REPORT 1215

CONTENTS

	Page
SUMMARY	141
INTRODUCTION	141
I. CALCULATED IMPINGEMENT OF DROPLETS ON CYLINDERS	142
ANALYSIS	142
Derivation of Equations of Motion	142
Calculation Procedure	143
Data Presentation	145
RESULTS AND DISCUSSION	145
Collection Efficiency	145
Maximum Angle of Impingement	147
Impingement of Intermediate Trajectories	147
Local Rate of Droplet Impingement	149
Tangential-Velocity Components	149
II. EFFECT OF COMPRESSIBILITY OF AIR FLOW AROUND CYLINDER ON IMPINGEMENT OF CLOUD DROPLETS	150
ANALYSIS	150
RESULTS	152
DISCUSSION	153
III. THEORY OF ROTATING MULTICYLINDER METHOD	154
BASIC CONCEPT	154
NONUNIFORM CLOUDS	154
Droplet-Size Distribution Patterns	154
Over-All Weighted Collection Efficiency	155
Comparison Curves	155
DETERMINATION OF DROPLET SIZE, LIQUID-WATER CONTENT, AND NOMINAL DROPLET-SIZE DISTRIBUTION	156
IV. APPARATUS AND PROCEDURE FOR MEASURING LIQUID-WATER CONTENT AND DROPLET SIZES IN SUPERCOOLED CLOUDS BY ROTATING MULTICYLINDER METHOD	157
APPARATUS	157
PROCEDURE	160
Operation	160
Calculation	161
Stepwise Calculating Procedure	161
(a) Average local airspeed	161
(b) Free-air temperature	161
(c) Parameter φ/DV	161
(d) Average cylinder diameter	162
(e) Amount of ice per unit space	162
(f) Plotting	162
(g) Matching procedure	162
(h) Droplet diameter and liquid-water content	163
V. EVALUATION OF ROTATING MULTICYLINDER METHOD	164
HEAT-BALANCE AND MASS-TRANSFER FACTORS IN FLIGHT MEASUREMENTS	164
Critical Rates of Freezing and Evaporation	165
Relation of Volume Rates of Freezing, Evaporation, and Run-Off	165
Correction of Multicylinder Measurements for Evaporation (Subcritical Case)	166
Interpretation of Multicylinder Data with Occurrence of Run-Off	166
DROPLET-SIZE DISTRIBUTION	168
EXPECTED ERRORS IN MATCHING FLIGHT DATA	168
CONCLUDING REMARKS	170
APPENDIXES	
A—SYMBOLS	170
B—STARTING CONDITIONS OF TRAJECTORIES AT LARGE VALUES OF $-x$	171
C—CONVERSION OF PRACTICAL FLIGHT UNITS INTO DIMENSIONLESS PARAMETERS	172
D—METHOD OF CALCULATING CURVES OF $1/K_o$ AGAINST E_o FOR DIFFERENT ASSUMED DROPLET-SIZE DISTRIBUTIONS	172

APPENDIXES—Continued

	Page
E—ALTERNATE METHOD OF REDUCING ROTATING MULTI-CYLINDER DATA, By Paul T. Hacker	173
INTRODUCTION	173
THEORY	173
Basic Concepts, Assumptions, and Dimensionless Parameters	173
Determination of Liquid-Water Content and Droplet Size	174
Application of Method to Clouds of Nonuniform Droplet Size	175
Units for Equations	175
STEPWISE CALCULATING PROCEDURE	175
Steps (a) to (d)	175
(e) Relative amount of ice per unit frontal area	175
(f) Parameter φ for average diameters of cylinders	175
(g) Tabulation of E_w as function of $K_o\varphi$ for values of φ	175
(h) Parameter E_w/I^*	175
(i) Plotting $K_o\varphi$ as function of E_w/I^*	175
(j) Droplet size	175
(k) Liquid-water content	177
DISCUSSION	177
F—ANALYSIS OF HEAT BALANCE AND MASS TRANSFER	178
ASSUMPTIONS	178
EQUATIONS	178
CALCULATIONS	180
FREEZING RATES	180
REFERENCES	182

REPORT 1215

IMPINGEMENT OF CLOUD DROPLETS ON A CYLINDER AND PROCEDURE FOR MEASURING LIQUID-WATER CONTENT AND DROPLET SIZES IN SUPERCOOLED CLOUDS BY ROTATING MULTICYLINDER METHOD [1]

By R. J. Brun, W. Lewis, P. J. Perkins, and J. S. Serafini

SUMMARY

Evaluation of the rotating multicylinder method for the measurement of droplet-size distribution, volume-median droplet size, and liquid-water content in clouds showed that small uncertainties in the basic data eliminate the distinction between different cloud droplet-size distributions and are a source of large errors in the determination of the droplet size. Calculations of the trajectories of cloud droplets in incompressible and compressible flow fields around a cylinder were performed on a mechanical analog constructed for the study of the trajectories of droplets around aerodynamic bodies. Many data points were carefully calculated in order to determine precisely the rate of droplet impingement on the surface of a right circular cylinder. From the computed droplet trajectories, the following impingement characteristics of the cylinder surface were obtained and are presented in terms of dimensionless parameters: (1) total rate of water impingement, (2) extent of droplet impingement zone, and (3) local distribution of impinging water on cylinder surface.

The rotating multicylinder method for in-flight determination of liquid-water content, droplet size, and droplet-size distribution in icing clouds is described. The theory of operation, the apparatus required, the technique of obtaining data in flight, and detailed methods of calculating the results, including necessary charts and tables, are presented. An evaluation of the multicylinder method includes the effect on final results of droplets that do not freeze completely on the cylinders after striking them, as well as probable errors in final results caused by the inherent insensitivity of the multicylinder method.

INTRODUCTION

As part of a comprehensive research program directed toward an appraisal of the problem of ice prevention on aircraft, the NACA has undertaken an investigation of the impingement of water droplets on aerodynamic bodies. Previous investigators have calculated the water-droplet trajectories for right circular cylinders (refs. 1 to 5), for bodies of revolution (refs. 6 to 8), for elbows (ref. 9), and for airfoils (refs. 10 to 15). The trajectory results on bodies of revolution, elbows, and airfoils have been applied to the design of equipment for the protection of aircraft components against ice formation. The calculations of water-droplet impingement on cylinders have occasionally been used for the same purpose but are most useful in connection with flight instruments used in the study of liquid-water content, droplet size, and size distributions in icing clouds. A knowledge of the constitution of supercooled clouds is necessary in order to design equipment for aircraft icing protection.

A commonly used technique for measuring cloud liquid-water content, droplet size, and droplet-size distribution involves the collection of ice on cylinders exposed to the air stream in the icing clouds. This technique is known as the rotating multicylinder method (refs. 1 and 16). In this method, several right circular cylinders of different diameters rotating on a common axis are exposed from an airplane in flight to the supercooled droplets in a cloud.

In the usual procedure for obtaining cloud-droplet data, the cylinders are extended through the airplane fuselage during the exposure period and are then retracted for disassembling and weighing. The cylinders are rotated during exposure in order to secure uniform ice collection around the circumference and thus to preserve a circular cross section during the entire exposure. It has usually been assumed that during the exposure period in flight all the supercooled droplets that strike the cylinders freeze completely on the cylinders. This assumption is not strictly true, because a small portion of the impinging water is lost by evaporation; and, under some conditions of temperature and impingement rate, a considerable fraction may run off in the liquid state (refs. 17 and 18). Calculated corrections for evaporation and calculated values of the conditions under which run-off may occur are presented herein.

The measurement of droplet size, droplet-size distribution, and liquid-water content is based on the principle that cylinders of different sizes collect different quantities of ice per unit frontal area. The amount of ice collected per unit frontal area is expressed in terms of the collection efficiency, that is, the ratio of the mass of ice collected to the mass of liquid water contained in the volume of space swept by the cylinder. The collection efficiency presented herein is obtained from calculations of cloud-droplet trajectories with respect to the cylinders. The collection efficiency is a known

[1] Supersedes NACA TN 2903, "Impingement of Cloud Droplets on Aerodynamic Bodies as Affected by Compressibility of Air Flow Around the Body," by Rinaldo J. Brun, John S. Serafini, and Helen M. Gallagher, 1952; TN 2904, "Impingement of Water Droplets on a Cylinder in an Incompressible Flow Field and Evaluation of Rotating Multicylinder Method for Measurement of Droplet-Size Distribution, Volume-Median Droplet Size, and Liquid-Water Content in Clouds," by Rinaldo J. Brun and Harry W. Mergler, 1952; and RM E53D23, "Procedure for Measuring Liquid-Water Content and Droplet Sizes in Supercooled Clouds by Rotating Multicylinder Method," by William Lewis, Porter J. Perkins, and Rinaldo J. Brun, 1953.

function of droplet size, cylinder size, airspeed, air density, and air viscosity. The liquid-water content and the average droplet diameter are determined from a comparison of the measured weight of ice collected on each cylinder with the calculated values of collection efficiency. The actual distribution of cloud-droplet sizes cannot be determined as such by the multicylinder method, but the degree of inhomogeneity can be approximated by comparing the flight data with values of collection efficiency calculated for hypothetical droplet-size distributions.

An evaluation of the effect of the compressibility of air on the cylinder collection efficiency is presented herein, because the flight critical Mach number on the cylinders is attained at relatively low airplane speeds. The flight critical Mach number is defined as that airspeed which results in sonic velocity at some location on the cylinder. In order to evaluate the magnitude of the compressibility effect on droplet impingement, trajectories in a compressible flow field around a cylinder were calculated at the NACA Lewis laboratory and the results compared with those of trajectories calculated in an incompressible flow field. The results of the trajectories calculated in an incompressible flow field were also compared with results available in references 1 to 5, in which the trajectories were calculated for an incompressible flow field around a cylinder. Some difference was found between the NACA results and those in the references. Also, a considerable difference was found to exist among the references cited. Because of the differences in the existing literature, a recalculation of the trajectories in an incompressible flow field around a cylinder was undertaken at the NACA Lewis laboratory.

In reference 1 the forces acting on the water droplet were calculated from Stokes' law for slow translatory motion of a small sphere in an incompressible viscous fluid. The forces acting on the water droplet were calculated more precisely in references 3 to 5 by the use of the experimentally determined drag coefficient for a sphere in terms of the Reynolds number. The calculations for the trajectories were performed in references 1, 2, 4, and 5 by a step-by-step integration of the second-order nonlinear differential equations that describe the motion of the droplets around a cylinder. The calculations presented in reference 3 were made more accurately with the use of a differential analyzer. Another difference among the investigations (refs. 1 to 5) is the values of the droplet velocities assumed at the beginning of the integration process of the equations of motion.

The method used in reference 3 for calculating the water-droplet trajectories has been used for calculating the data persented herein. Many more data points were carefully calculated for the results presented herein than were calculated for the data in reference 3, in order to determine more precisely the rate of impingement of droplets on the surface of the cylinder. Accuracy was emphasized in all the calculations, because the insensitivity of the rotating multicylinder method in its application to the measurement of droplet-size distribution does not permit wide tolerances in the theoretical data. Curves were established over a wide range of the variables in order to determine whether the impingement on cylinders follows rules that might be available for extension in future studies to other aerodynamic bodies.

The procedure is also presented in this report for the application of the calculated data in the determination of average droplet size, droplet-size distribution, and liquid-water content from multicylinder flight data. The description of the apparatus adopted for flight use at the NACA Lewis laboratory, the procedure used in taking data in flight, and the customary method of processing the flight data are descriptions of techniques developed by the NACA and others interested in the problem of measuring the characteristics of icing clouds. These techniques are based on the methods proposed in reference 3.

I. CALCULATED IMPINGEMENT OF DROPLETS ON CYLINDERS

The trajectories of atmospheric water droplets about a cylinder moving at subsonic velocities were calculated with the aid of a differential analyzer at the NACA Lewis laboratory. The rate, distribution, and surface extent of impinging droplets were obtained from the computed trajectories and are summarized in this section in terms of dimensionless parameters.

ANALYSIS

DERIVATION OF EQUATIONS OF MOTION

As a cylinder moves through a cloud, the amount of water intercepted by the cylinder depends on the cylinder size, the flight and meteorological conditions, and the inertia of the cloud droplets. In order to obtain the surface extent of impingement and the rate of droplet impingement per unit area on a cylinder, the cloud-droplet trajectories with respect to the cylinder must be determined. The differential equations that describe the droplet motion have been stated in reference 3 and are derived in the following paragraphs.

From the conventional forms of the equations for the drag force of a body in a fluid

$$F=C_D\frac{1}{2}\rho_a\pi a^2\bar{v}^2$$

and for Reynolds number

$$Re=\frac{2a\rho_a\bar{v}}{\mu}$$

there is obtained

$$F=\frac{C_D Re}{4}\pi a\mu\bar{v}$$

for a sphere having a relative velocity $\bar{v}$ with respect to the fluid. (All symbols are defined in appendix A.) The equation of motion of a water droplet in terms of its x-component in a rectangular coordinate system is

$$\frac{4}{3}\pi a^3\rho_w\frac{dv_x'}{dt}=\frac{C_D Re}{4}\pi a\mu(u_x'-v_x')$$

$$\left(\frac{2}{9}\frac{a^2\rho_w}{\mu}\frac{U}{L}\right)\frac{dv_x'}{dt}\frac{L}{U^2}=\frac{C_D Re}{24}\frac{(u_x'-v_x')}{U}$$

where the velocity terms with the prime superscript are in feet per second. In dimensionless terms, the equation of

motion for the x-component becomes

$$\frac{dv_x}{d\tau}=\frac{C_D Re}{24}\frac{1}{K}(u_x-v_x) \tag{1}$$

and for the y-component becomes

$$\frac{dv_y}{d\tau}=\frac{C_D Re}{24}\frac{1}{K}(u_y-v_y) \tag{2}$$

where

$$K=\frac{2}{9}\frac{\rho_w a^2 U}{\mu L} \tag{3}$$

The Reynolds number Re can be obtained conveniently in terms of the free-stream Reynolds number,

$$Re_0=\frac{2a\rho_a U}{\mu} \tag{4}$$

so that

$$\left(\frac{Re}{Re_0}\right)^2=(u_x-v_x)^2+(u_y-v_y)^2 \tag{5}$$

The free-stream Reynolds number, expressed with respect to the droplet size, is used as a convenient term in the calculations and is not intended to imply relative motion between the droplet and the free-stream air.

The term $C_D Re/24$ containing the coefficient of drag for the droplets, required in equations (1) and (2), may be obtained from tables in reference 3 or 10. The values presented in references 3 and 10 were obtained from experimental wind-tunnel data on the drag forces on spheres, presented in reference 19. As the relative motion between the droplets and air approaches zero as a limiting value, the value of $C_D Re/24$ approaches unity as the limiting value, and Stokes' law for the drag forces acting on spheres applies.

The air velocity components (ref. 20) for a cylinder in a uniform, potential, and incompressible flow in two dimensions and without circulation are

$$\left.\begin{aligned} u_x&=1+\frac{y^2-x^2}{(x^2+y^2)^2}\\ u_y&=-\frac{2xy}{(x^2+y^2)^2}\end{aligned}\right\} \tag{6}$$

Equations (1) to (6) are written in dimensionless form in order to maintain the number of calculations at a minimum and to simplify the presentation of the results. The equations apply to the motion of droplets in a plane perpendicular to the axis of the cylinder, which is located at the origin of the rectangular coordinate system, as shown in figure 1. At an infinite distance ahead of the cylinder, the uniform air flow carrying the cloud droplets is assumed to be approaching the cylinder from the negative x-direction and parallel to the x-axis. All the distances appearing in the equations and in the figures are ratios to the cylinder radius L, which is the unit of distance. The velocities appear as fractional parts of the free-stream velocity U. Time is expressed in terms of the cylinder radius and free-stream velocity, so that

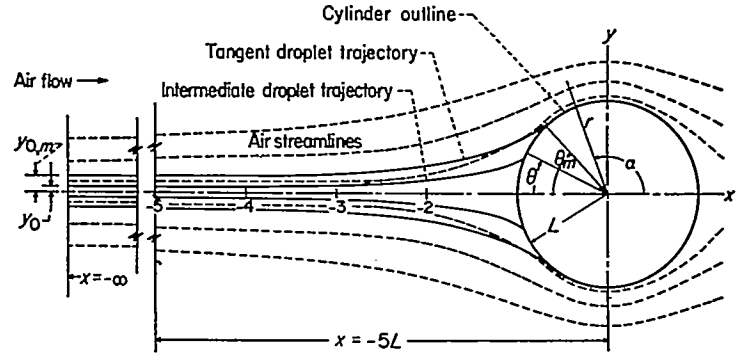

FIGURE 1.—Coordinate system for cylinder.

$\tau=tU/L$. In this manner the unit of time is the time required for a droplet to travel a distance L at velocity U.

The differential equations (1) and (2) state that the motion of a droplet is governed by the drag forces imposed on the droplet by virtue of the relative velocities between the droplet and the local air in motion along the streamlines around the cylinder. The droplet momentum tends to keep the droplet moving in a straight path, while the drag forces tend to force the droplet to follow the streamlines. For very small droplets and slow speed, the momentum of the droplets parallel to the direction of the free-stream motion is small, and the drag forces are large enough that little deviation from the streamlines occurs; whereas, for large droplets or high speed, the momentum is large enough to cause the droplets to deviate from the streamlines and follow a path more nearly in the direction established by the free-stream velocity. In accordance with the statement of equations (1) and (2) and the definition of the parameter K in equation (3), the trajectories depend on the size of the cylinder, the radius of the droplet, the airspeed, and the air viscosity as first-order variables.

Assumptions that have been necessary in order to solve the problem are:

(1) At a large distance ahead of the cylinder (free-stream conditions), the droplets move with the same velocity as the air.

(2) No gravitational force acts on the droplets.

(3) The droplets are always spherical and do not change in size.

The first two assumptions are valid for droplets smaller than drizzle or rain drops, because the inertial forces of the droplets are usually much greater than the gravitational force. The assumptions are also valid for falling rain drops if the free-stream velocity with respect to the cylinder is much greater than the drop velocity caused by gravitational force. Preliminary calculations show that the third assumption is valid for the usual meteorological and flight conditions in which cylinders are used. An evaluation of the evaporation rate of droplets is presented in reference 21.

CALCULATION PROCEDURE

The differential equations of motion (eqs. (1) and (2)) are difficult to solve by ordinary means, because the actual values of the velocity components of the droplet relative to the air and the term containing the coefficient of drag are not known until the trajectory is traced. These values are determined

as the trajectory of a droplet is developed, because their magnitude depends on the position of the droplet in the flow field. Simultaneous solutions for the two equations of motion were obtained with the use of a mechanical analog based on the principle of a differential analyzer. A description of this analog and the method of solution for the droplet trajectories are presented in appendix A of reference 22. The answers were obtained in the form of plots of the droplet trajectories with respect to the cylinder, as shown in figure 2. The second-quadrant section of the cylinder is outlined. The ordinate scale was expanded approximately 4 times the abscissa scale with appropriate gearing in the analog in an effort to obtain the maximum accuracy in the determination of the points of impingement of the droplets on the cylinder surface.

Before the integration of the equations of motion could be performed with the analog, the velocity of the droplets at the start of the integration had to be determined. As has been postulated in the assumptions, at an infinite distance ahead of the cylinder, all the droplets have vertical and horizontal components of velocity that are the same as those of the free-stream air. At finite distances ahead of the cylinder, the droplets have velocity components and positions varying between those pertaining to the undisturbed free stream and those pertaining to the air streamlines. A study of the air streamlines showed that only a gradual deviation of the air streamlines from the free-stream velocity takes place up to approximately 5 radii ahead of the cylinder centerline. A large rate of change of air motion takes place between $x=-5$ and the cylinder surface. The equations of motion (eqs. (1) and (2)) were linearized by an approximation and solved between $x=-\infty$ and $x=-5$ by the method presented in reference 3 and discussed herein in appendix B. The trajectories of the droplets impinging on the cylinder are shown in figure 2 plotted from $x=-5$ to the point of impingement on the cylinder surface. The analog starting conditions at $x=-5$, as calculated by the linearized equations, were checked for several values of K and were found to be within the accuracy of the analog (appendix B).

The trajectories shown in figure 2 are representative of operating conditions that result in values of $K=4$ and $Re_0=63.246$ (eqs. (3) and (4)). The topmost trajectory A is tangent to the cylinder and determines the maximum extent of impingement of droplets for the conditions given for figure 2. All droplets having trajectories below this tangent trajectory strike the cylinder; whereas, all droplets having trajectories above this line will miss the cylinder.

The impingement of droplets on the third quadrant of the cylinder (fig. 1) is identical to that on the second quadrant, except that the trajectories are mirror images of those shown in figure 2. The amount of water impinging on the cylinder is the total water in those droplets bounded by the second- and third-quadrant tangent trajectories. If the cloud of droplets is assumed to be uniform at a large distance ahead of the cylinder (free-stream conditions), the water intercepted by the cylinder per unit time is the water contained in a volume of cloud of unit depth and length but

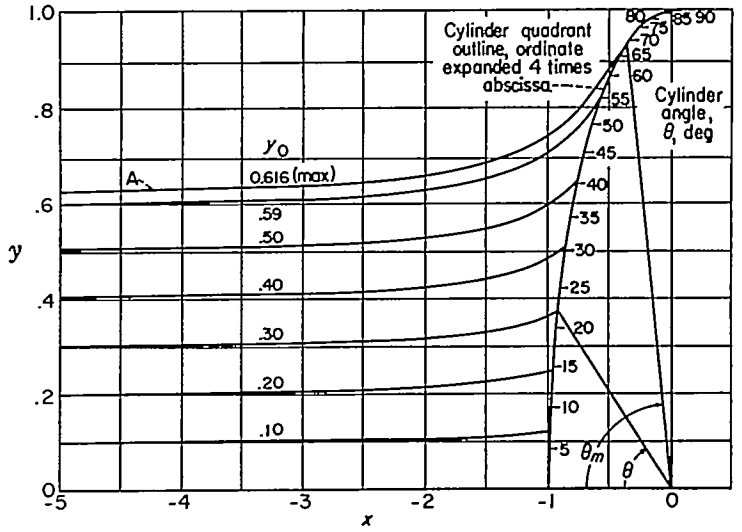

FIGURE 2.—Trajectories of droplets impinging on cylinder. Free-stream Reynolds number, 63.246; inertia parameter, 4; φ, 1000.

with a width that has twice the value of $y_{0,m}$, the ordinate at infinity of the tangent trajectory.

For the conditions of K and Re_0 applicable to the trajectories shown in figure 2, the tangent trajectory A also determines the cylinder collection efficiency, which is defined as the ratio of the actual water in the droplets intercepted by the cylinder to the total water in the volume swept out of its path by the cylinder. For a cloud composed of droplets all uniform in size, the collection efficiency is equal to $y_{0,m}$ in magnitude, because in the trajectory calculations the ordinate $y_{0,m}$ is given as a ratio to the cylinder radius.

The tangent trajectories were computed in order to obtain the water intercepted by the cylinder and the cylinder collection efficiency. The tangent trajectories also determine the angle of maximum extent of impingement. The angle of maximum extent of impingement is denoted by θ_m (fig. 2), and the angle of impingement of the intermediate trajectories is denoted by θ. The accuracy in determining θ_m was approximately $\pm 1.5°$. The trajectories intermediate between the x-axis and the tangent trajectory were computed in order to obtain the distribution of the water on the cylinder surface.

Trajectories for droplets with low inertia hovered along the surface of the cylinder over large circumferential distances. The crowding together of the trajectories near the cylinder for very low values of K did not permit the $\pm 1.5°$ accuracy to be maintained for values of $K<1$ with the same scale factors shown in figure 2. For values of $K<1$, the scale factors of the cylinder were doubled so that the trajectories were plotted with respect to a cylinder 40 inches in diameter. For these low values of K, the ordinate scale was not distorted with respect to the abscissa scale. A small section of the cylinder surface with the trajectories of droplets impinging on it is shown in figure 3. Although only the portion of the trajectories from $x=-2$ up to the cylinder surface is shown in figure 3, the trajectories were calculated by the machine from $x=-5$, and the starting conditions at $x=-5$ were obtained as explained in appendix B.

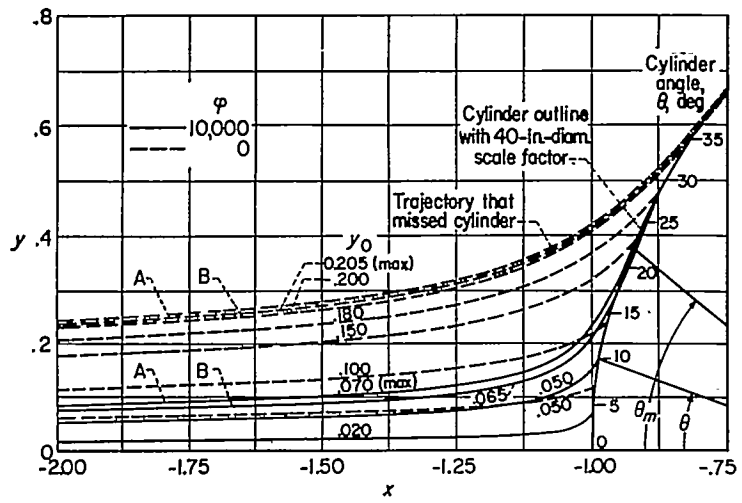

FIGURE 3.—Trajectories of droplets with low inertia parameter ($K=0.5$).

An attempt was made to increase the ease in locating the point of tangency by calculating a trajectory slightly below the tangent trajectory and running the trajectory through the cylinder (trajectories B, fig. 3). The trajectory near the tangent trajectory defined the tangency by cutting the cylinder at two definite points, such as a secant line. This method of determining the tangent is accurate only if trajectory B is very near the tangent trajectory. The increase in scale factor for low values of K permitted an accuracy of $\pm 1.5°$ to be obtained for θ_m for $K=0.5$, and $\pm 2°$ for $K=0.25$.

DATA PRESENTATION

Series of trajectories, such as those shown in figure 2, computed for several combinations of values of K and Re_0, permit the evaluation of area, rate, and distribution of water-droplet impingement on cylinders. The data are presented herein in terms of dimensionless parameters in order to generalize the presentation of the data and to gain flexibility in the application of the data to experimental and analytical studies. Examples involving dimensions and flight conditions are used herein whenever the examples are aids in clarifying the presentation of the data. Typical values of dimensions and flight conditions are used in most of the examples given; however, because of the nature of the dimensionless parameters, a large number of combinations of values of the variables, such as free-stream velocity, cylinder size, droplet size, and others (eqs. (3) and (4)), would apply to the particular value of the dimensionless parameter illustrated by the example. A system of equations for the evaluation of dimensionless parameters in terms of variables with units commonly employed in aeronautics is presented in appendix C.

The results are often presented herein as functions of the parameter K. The parameter K has been termed the inertia parameter, because its magnitude directly reflects the external force required on a droplet to cause a deviation from the original line of motion of the droplet. A dimensionless parameter φ, defined as

$$\varphi \equiv \frac{Re_0^2}{K} = \frac{18\rho_a^2 LU}{\mu\rho_w} \tag{7}$$

was adopted in reference 3 for the presentation of the data and is also employed herein. The parameters K and φ together are sufficient to define the conditions of a particular impinging droplet. The parameter φ is valuable in that φ is not a function of droplet size. The parameter φ is an important concept in the interpretation of icing-cloud measurements in which the droplet size is not measured directly and is an unknown which must be calculated. (Procedure for calculating droplet size is discussed in sections III and IV.) In the interpretation of icing-cloud measurements in which cylinders of different diameters are exposed to the supercooled droplets from an airplane in flight, φ may be considered to be a function of altitude through its dependence on air density ρ_a and viscosity μ for any given cylinder size and flight speed.

The magnitude of φ is a measure of the deviation from Stokes' law for the forces acting on the water droplets. Stokes' law was derived for slow translatory motion of a small sphere in an incompressible viscous fluid and applies precisely in the limiting value of $\varphi=0$, when the free-stream Reynolds number is zero or the droplet motion relative to the cylinder approaches zero as the limit (eq. (7)).

RESULTS AND DISCUSSION

COLLECTION EFFICIENCY

The collection efficiency is presented in figure 4 as a function of the inertia parameter K and the parameter φ. For the conditions in which a cylinder is moving through a cloud of droplets that are all uniform in size, the total rate of water interception per foot span of the cylinder is

$$W_m = 2ELUw \tag{8}$$

The collection efficiency increases with increasing values of K. The primary variables in the inertia parameter K (eq. (3)) are the droplet size, the free-stream velocity, and the cylinder size. The range of variation of water density or air viscosity over the range of temperature changes in the ordinary atmosphere from sea level to 30,000 feet is small compared with the range of variation possible with the other variables in equation (3).

The collection efficiency increases with increasing droplet size and free-stream velocity, because an increase in the free-stream momentum of the droplet with respect to a cylinder increases the forces necessary to force the droplet around the cylinder. An increase in the cylinder size decreases the collection efficiency, because the large cylinders cause the air streamlines to start moving around the cylinder a greater actual distance (not in terms of ratio to cylinder radius) ahead of the cylinder than the small cylinders. The greater distance ahead of the cylinder in which the streamlines are moving around the large cylinder permits the air drag forces to act on the droplets for a longer time t in seconds, thus causing a smaller proportion of the droplets that are in the path of the cylinder to impinge on the cylinder.

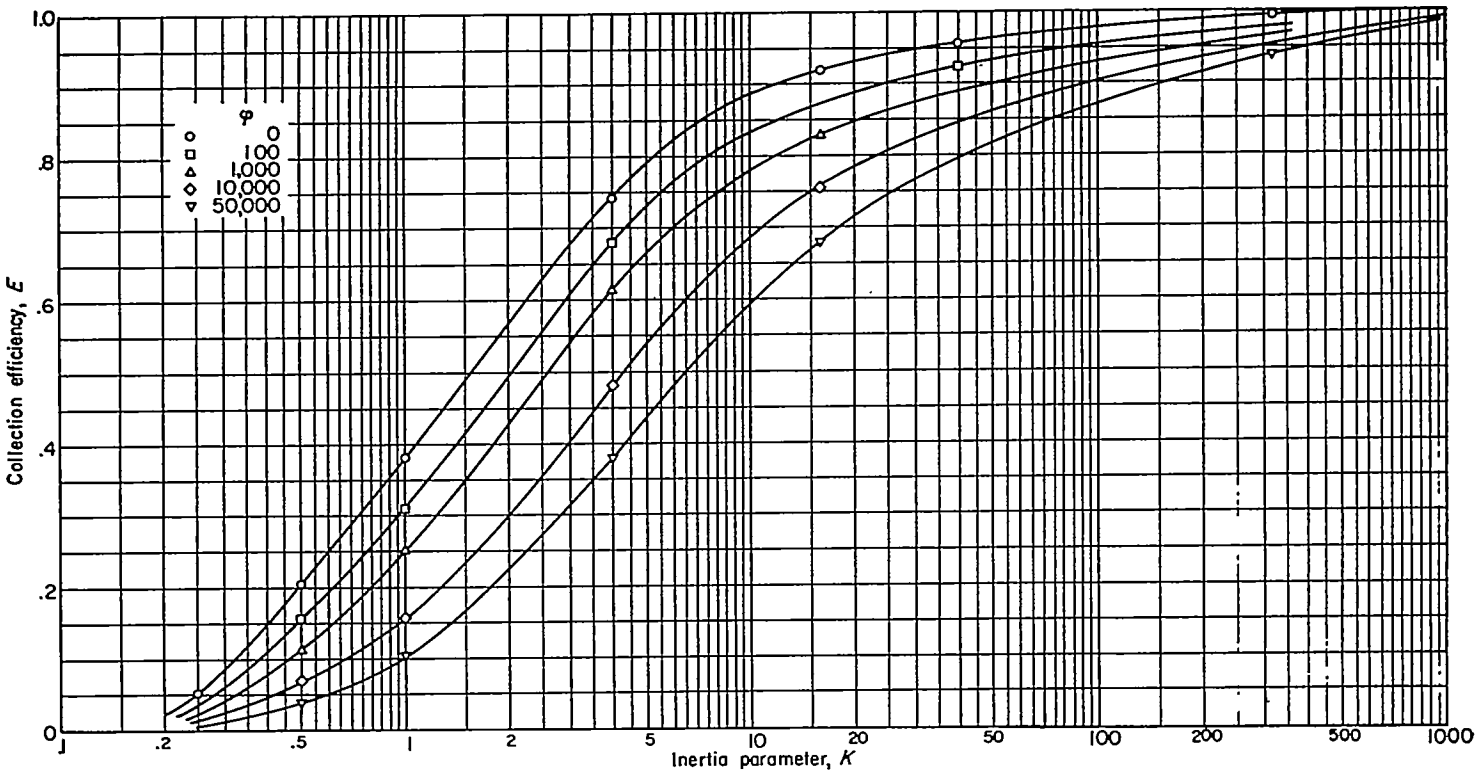

FIGURE 4.—Cylinder collection efficiency. (A 17- by 21-in. print of this figure is available from NACA on request.)

For the conditions in which Stokes' law applies for the drag force ($\varphi=0$), the values of figure 4 for collection efficiency are very nearly the same as those presented in reference 3. The results of figure 4 and reference 3 are both lower than those presented in references 1 and 2, again for $\varphi=0$. The calculations for the work presented in references 1 and 2 were not made with differential analyzers, nor were the conditions at the start of the trajectories determined by the method presented in appendix B. The differences may result from either the method of calculation or the assumptions at the starting conditions. The calculations of reference 2 included only values of K less than 2. The results of figure 4 differ somewhat from those of reference 3. For $\varphi=10{,}000$, the results of figure 4 are higher than those in reference 3 by 0, 8, 7, 2, and 0 percent for $K=1$, 4, 16, 36, and 256, respectively.

The calculated points shown in figure 4 are presented in table I. Corresponding points obtained from curves given in reference 3 are also given in table I for comparison. No calculations were made in references 1 and 2 for values of φ other than zero. Although a few calculations were made in reference 5 for $\varphi=16{,}000$, the results are not comparable with either the results presented herein or in reference 3, because the starting conditions and method of computation were not the same. For the same reasons, the results of reference 4 are not comparable. The values of E given in reference 4 are all considerably higher for all values of φ than values for corresponding conditions given either herein or in reference 3.

The expanded ordinate scale used with the analog permitted the calculations presented herein for the collection efficiency to be read accurately within ± 0.002 unit for values of E between 0.20 and 1.00. The accuracy in obtaining E for values of $K=0.5$ and 0.25 was ± 0.003 and ± 0.004, respectively, because the accuracy in the determination of the tangent trajectory was not as good for the low values of K, as stated previously. The values shown in figure 4 for $K=0.5$ and 0.25 are averages of two or more check calculations.

TABLE I.—COMPARISON WITH RESULTS OF REFERENCE 3

φ	K	Re_0	E		θ_m		v_x		v_y	
			NACA	Langmuir	NACA	Langmuir	NACA	Langmuir	NACA	Langmuir
0	0.25	0	0.051	0.042	0.330	------	0.151	------	0.438	------
	.50	0	.205	.186	.716	0.688	.573	0.523	.658	0.035
	1	0	.380	.380	.980	.991	.817	.827	.547	.542
	4	0	.741	.722	1.379	1.365	1.039	1.008	.198	.211
	16	0	.920	.909	1.518	1.517	1.018	1.002	.054	.055
	40	0	.957	.962	1.538	1.546	1.014	------	.036	------
	320	0	.995	.997	1.557	1.567	1.005	------	.016	------
100	0.50	7.071	0.157	0.127	0.601	0.565	0.445	------	0.650	------
	1	10	.309	.296	.865	.857	.717	0.915	.612	0.793
	4	20	.680	.639	1.291	1.253	1.022	.993	.295	.326
	40	63.246	.924	.928	1.522	1.504	1.018	------	.050	------
1,000	0.50	22.361	0.116	0.090	0.504	0.483	0.329	------	0.596	------
	1	31.623	.250	.228	.760	.719	.617	------	.650	------
	4	63.246	.616	.568	1.20	1.147	.980	------	.382	------
	16	126.49	.830	.806	1.445	1.391	1.036	------	.133	------
10,000	0.50	70.711	0.070	0.053	0.385	0.384	0.195	------	0.482	------
	1	100	.157	.156	.595	.597	.441	0.494	.650	0.725
	4	200	.480	.441	1.060	.997	.890	.877	.500	.507
	16	400	.755	.710	1.345	1.286	1.035	1.039	.239	.304
50,000	0.5	158.114	0.038	0.035	0.267	0.314	0.085	------	0.310	------
	1	223.607	.105	.097	.45	.494	.266	------	.549	------
	4	447.214	.378	.340	.016	.873	.762	------	.584	------
	16	894.427	.682	.615	1.258	1.169	1.009	------	.327	------
	320	4000	.940	.912	1.515	1.470	1.020	------	.058	------

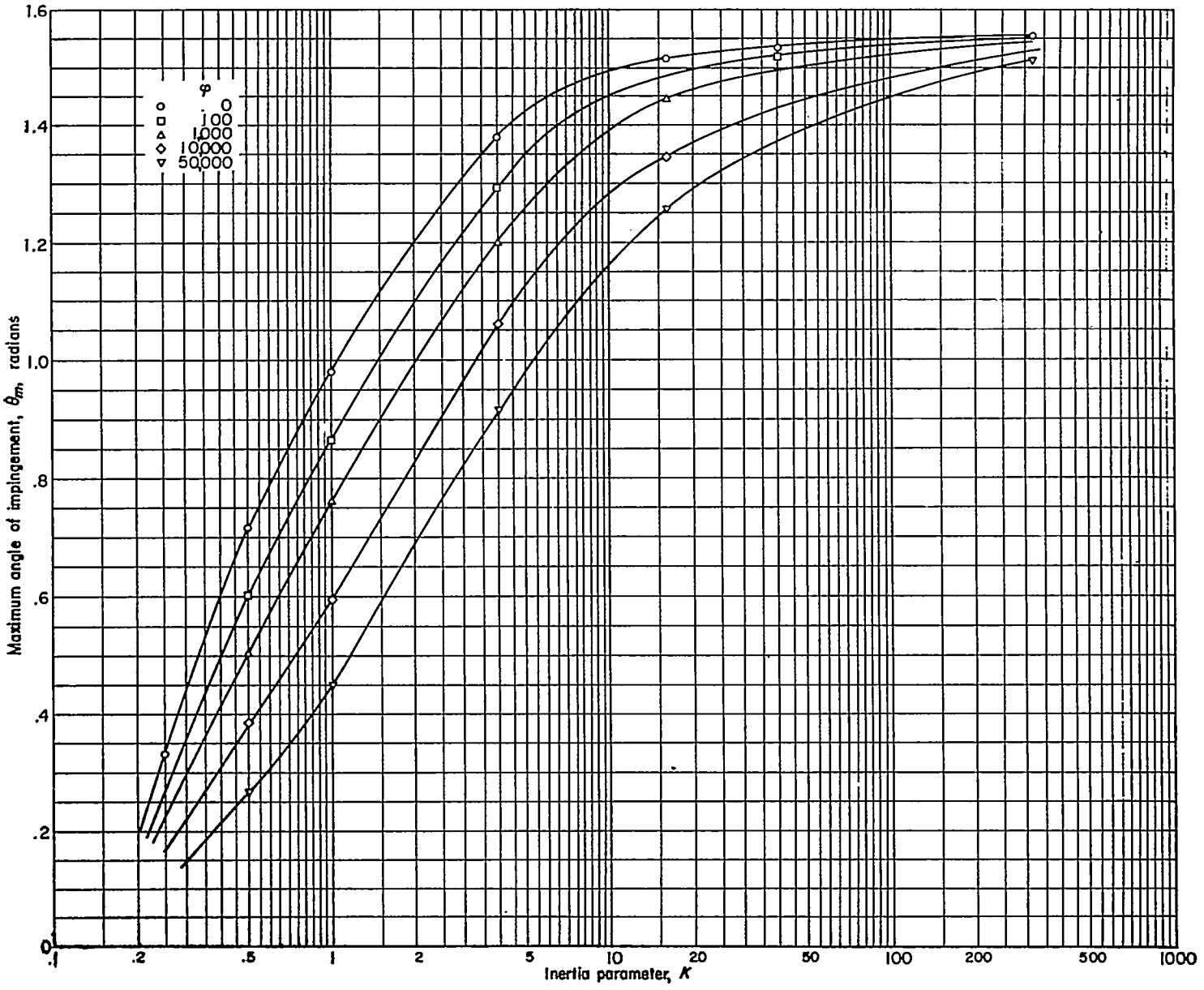

FIGURE 5.—Maximum angle of impingement on cylinder. (A 17- by 21-in. print of this figure is available from NACA on request.)

MAXIMUM ANGLE OF IMPINGEMENT

The maximum angle of impingement is given in figure 5 as a function of K and φ. The maximum angle of impingement, in radians, increases with increasing values of the inertia parameter K. The curves in figure 5 are similar in shape to those in figure 4 for the collection efficiency. As was discussed in the section on CALCULATION PROCEDURE, the accuracy in determining θ_m was $\pm 1.5°$ for conditions in which $K=0.5$. The curves of figure 5 were faired through averages of readings by several observers of the original trajectory plots. For the low values of K ($K<1$), two or often more than two check analog calculations were made. A comparison of the angle of impingement given by the curves of figure 5 with the results of reference 3 is made in table I.

IMPINGEMENT OF INTERMEDIATE TRAJECTORIES

The starting ordinate y_0 at infinity of any trajectory, including the trajectories between the tangent trajectory and the x-axis such as shown in figure 2, can be found in figure 6 for any given angle of impingement on the cylinder. The starting and ending positions of the trajectories are shown in figure 6 for the five different values of φ studied. For each value of φ, curves for several values of K are presented. The choice of the particular values of K shown in each figure was governed by the gearing available for the analog.

The amount of water impinging between any two given points on a cylinder moving through a uniform cloud can be found from the results given in figure 6. For example, if the amount of water impinging between the x-axis and a point $\theta=45°=0.785$ radian must be known for a 1½-inch cylinder moving with a free-stream velocity of 130 miles per hour through a cloud composed of 20-micron droplets, the value of y_0 to be used in the relation

$$W=UwLy_0 \tag{9}$$

for $\varphi=1000$ and $K=4$ is found in figure 6 (c) to be 0.53. The amount of water impinging between two points, where one

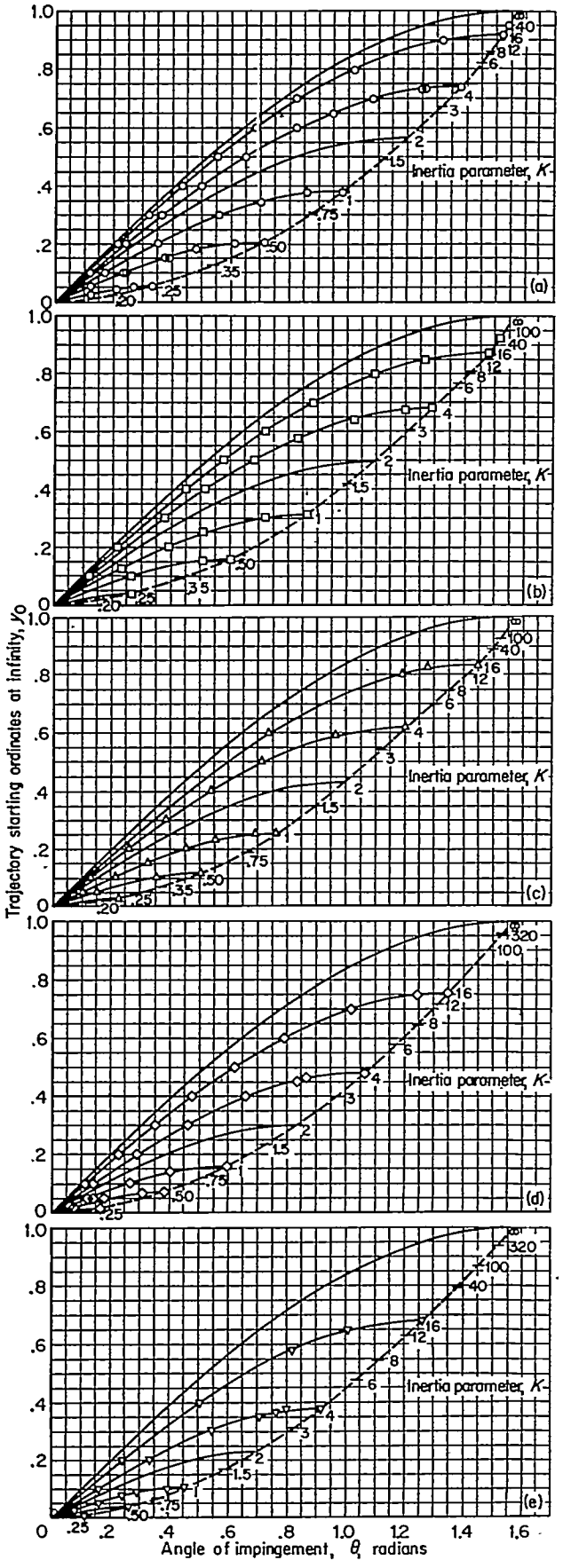

(a) φ, 0.
(b) φ, 100.
(c) φ, 1000.
(d) φ, 10,000.
(e) φ, 50,000.

FIGURE 6.—Trajectory starting ordinates as function of angle of impingement.

of the points is not on the x-axis, is found by using the relation

$$W=UwL(y_{0,2}-y_{0,1}) \tag{9a}$$

The angle θ is given in radians in figure 6 to permit a convenient conversion of the data of figure 6 in the determination of local rates of water impingement discussed in the following section.

An analysis of the data points in figure 6 reveals that all the points fall on sine curves, with amplitude and period depending on the values of K and φ studied. The reason for this behavior is not apparent from a study of the equations of motion (eqs. (1) and (2)), which are very nonlinear and do not permit a formal solution. However, this behavior of the data can be used advantageously, in that curves of y_0 as a function of θ for values of φ and K in addition to those curves given in figure 6 are possible with the aid of the expression

$$y_0=E\sin\left(\frac{\pi}{2}\frac{\theta}{\theta_m}\right) \tag{10}$$

The following examples illustrate the use of equation (10). If the curve of y_0 as a function of θ for $\varphi=100$ and $K=2$ is desired (shown in fig. 6(b) without calculated points), the amplitude and period that determine the terminus of the desired curve are obtained from figures 4 and 5, respectively. The value of $y_{0,m}=E=0.493$ is found in figure 4, and the value of $\theta_m=1.092$ is found in figure 5. These values of $y_{0,m}$ and θ_m are the terminus values and a measure of the amplitude and period, respectively, of the desired sine curve for $\varphi=100$ and $K=2$. Other points along the desired curve are obtained by solving equation (10) over a range of values of θ from zero to θ_m.

If a knowledge is required of the amount of water impinging between $\theta=40°=0.698$ radian and $\theta=50°=0.873$ radian on a cylinder for which the operating conditions were $K=6$ and $\varphi=3000$, the value of $(y_{0,2}-y_{0,1})$ required in equation (9a) is found by interpolation of the curves presented in figures 4 and 5. The value of $y_{0,m}=E$ is found from figure 4 to be 0.66. The value of θ_m is found from figure 5 to be 1.255. The values of θ/θ_m required for use with equation (10) are $0.698/1.255=0.556$ and $0.873/1.255=0.696$ for the two points of interest on the cylinder. The value of $(y_{0,2}-y_{0,1})$ for use in equation (9a) is

$$0.66\left[\sin\left(\frac{\pi}{2}0.696\right)-\sin\left(\frac{\pi}{2}0.556\right)\right]=0.080$$

The dashed lines in figure 6 are the loci of the termini of the sine curves. These dashed lines are cross plots of the curves given in figures 4 and 5. The accuracy in determining the dashed lines is the same as the accuracy for figures 4 and 5. The accuracy in obtaining the intermediate points was usually much better, because the points where the intermediate trajectories intercepted the cylinder were much better defined than were those of the tangent trajectories (figs. 2 and 3). The tolerances are approximately ±0.001 for y_0 and ±0.012 radian for θ.

LOCAL RATE OF DROPLET IMPINGEMENT

The local rate of water impingement per unit of area on the cylinder surface located at a given angle θ can be determined from the relation

$$W_\beta = Uw\frac{dy_0}{d\theta} = Uw\beta \tag{11}$$

provided θ is measured in radians. The magnitude of the term $dy_0/d\theta$ is the fractional part of the maximum water that could impinge on a local area of the cylinder, if all the trajectories were parallel straight lines and the cylinder surface were projected into a plane perpendicular to the trajectories. A value of

$$\frac{dy_0}{d\theta} = \beta = 1$$

indicates that the intensity of impingement on a local area of the cylinder is the maximum possible for the liquid-water content present in the cloud. For a uniform cloud composed of droplets all of the same size, the value of β is obtained from the slope of the curves of y_0 as a function of θ presented in figure 6. Curves of β that correspond to the data of figure 6 are presented in figure 7. The rate of droplet impingement is highest at the stagnation point ($\theta=0$).

Curves of β as a function of θ in addition to those given in figure 7 can be found from the relation

$$\beta = \frac{\pi}{2}\frac{E}{\theta_m}\cos\left(\frac{\pi}{2}\frac{\theta}{\theta_m}\right)$$

where θ is measured in radians. This relation applies on the assumption that the curves in figure 6 are sine curves for which the amplitude is characterized by $y_{0,m}$ and the period by θ_m.

TANGENTIAL-VELOCITY COMPONENTS

The tangential-velocity components of both the air and those droplets that are tangent to the surface of the cylinder are presented in figure 8 in the form of a velocity hodograph. The vertical and horizontal components of the air velocity at the surface of the cylinder can be found from the outermost velocity hodograph. The graduations denote the angle θ measured clockwise on the cylinder from the $-x$ ordinate to the $+y$ ordinate (fig. 1). The velocity components of those droplets that impinge tangentially to the cylinder (trajectory A, fig. 2) can be found from the hodograph enclosed by the air hodograph. A line passing through the 0,0 ordinates of the hodograph and a given position angle θ on the air hodograph will give the velocity direction of both the air and the droplets at that point on the cylinder, because both the air and the droplet velocities are tangent to the cylinder. The values of the inertia parameter K that correspond to the calculated points are shown at each point. Apparently, the velocity components for all droplets, regardless of the combination of φ and K, can be represented by one curve. This relation between v_y and v_x was also noted for airfoils in reference 11.

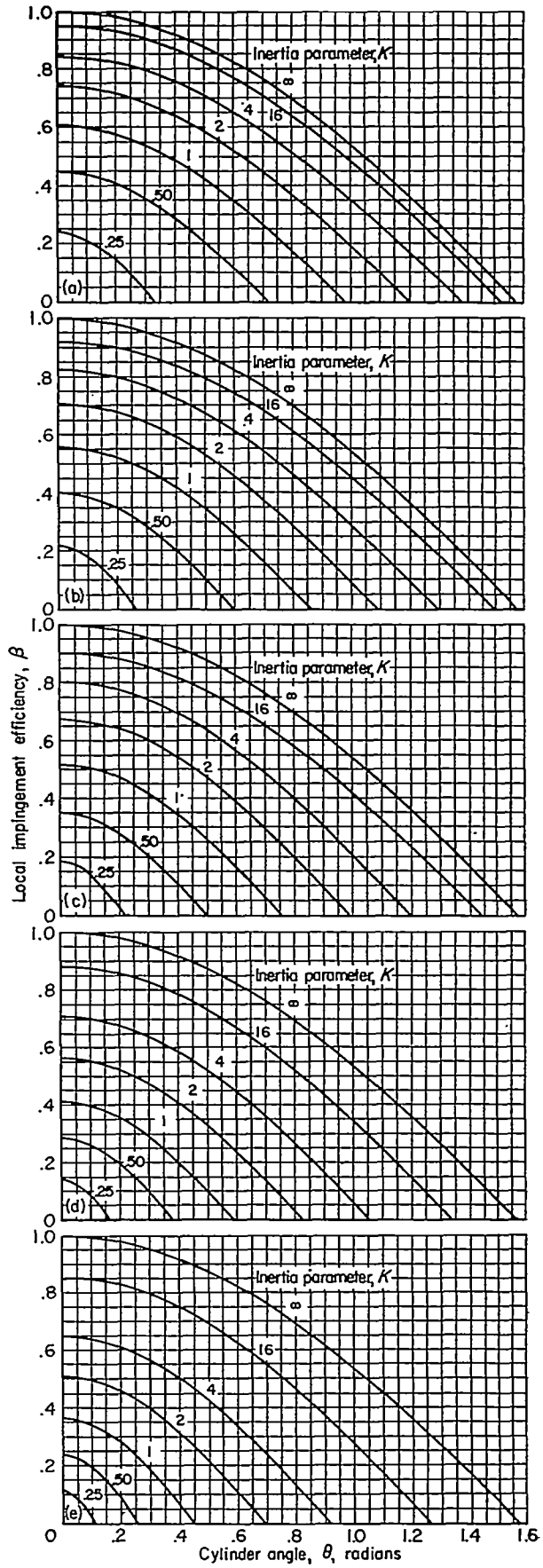

(a) φ, 0.
(b) φ, 100.
(c) φ, 1000.
(d) φ, 10,000.
(e) φ, 50,000.

FIGURE 7.—Local impingement efficiency as function of cylinder angle.

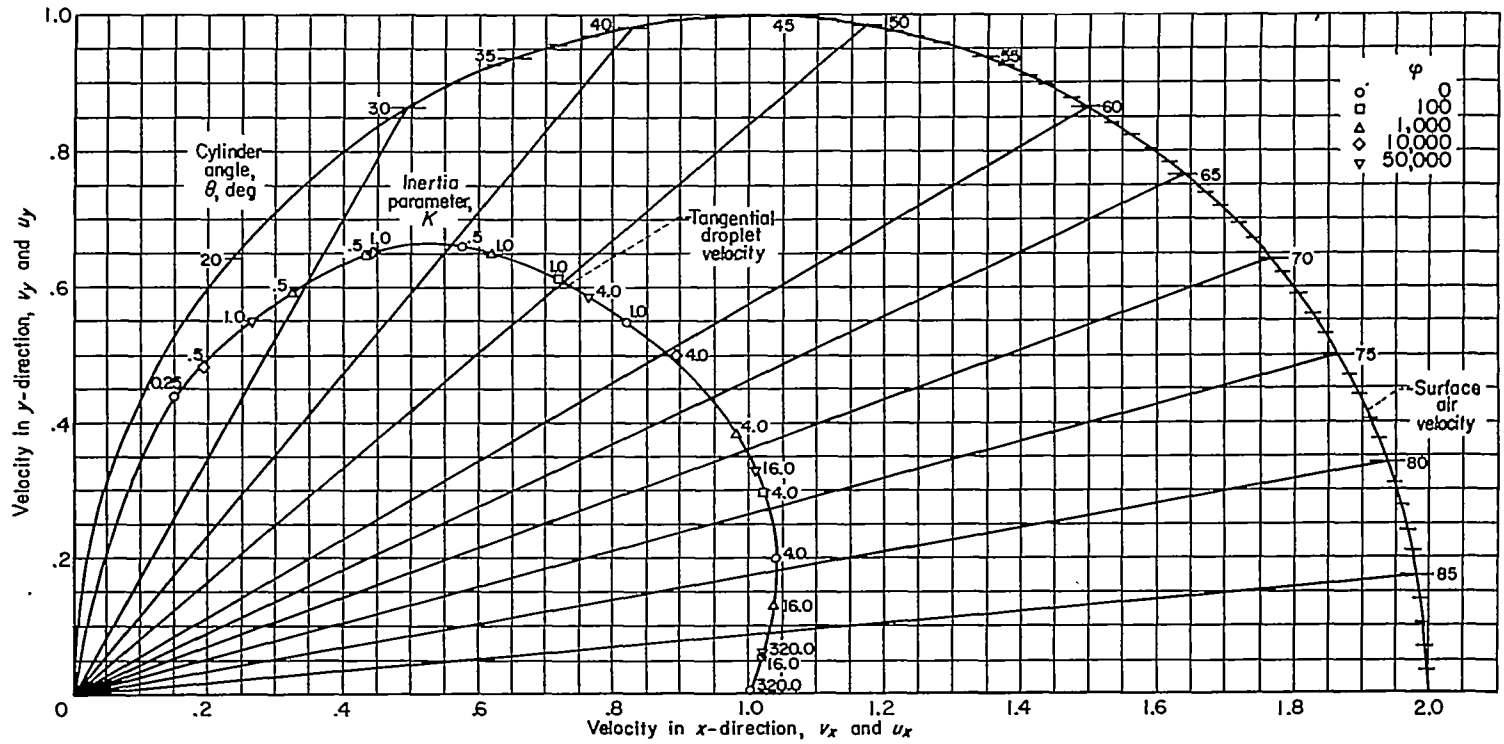

FIGURE 8.—Tangential-velocity hodograph for air and droplets at surface of cylinder.

The method for obtaining the vertical and horizontal component velocities of both the air and the droplets is illustrated for the example involving a cylinder 1⅝ inches in diameter moving with a free-stream velocity of 125 miles per hour at 10,000 feet NACA standard altitude conditions through a cloud composed of uniform droplets 20 microns in diameter. For these conditions $K=3.6$ and $\varphi=1000$. The maximum angle of impingement, which corresponds to the point on the cylinder where these droplets impinge tangentially, is found in figure 5 to be 1.172 radians, or 67°. The vertical component of droplet velocity v_y at the point of tangency on the cylinder is 0.41 and the horizontal component v_x is 0.96, both values being given in figure 8 as ratios to the free-stream velocity. The air velocity components u_y and u_x are 0.72 and 1.69, respectively, times the free-stream velocity.

At the cylinder angle θ_m of 90°, all the horizontal droplet velocities must be unity, which is the free-stream velocity, because only the droplets with infinite inertia will be tangent to the 90° point on the cylinder.

II. EFFECT OF COMPRESSIBILITY OF AIR FLOW AROUND CYLINDER ON IMPINGEMENT OF CLOUD DROPLETS

All the calculations presented in section I were made with the assumption that the air surrounding the cylinders behaved as an incompressible fluid. An evaluation of the effect of the compressibility of air in the flow field on the trajectories of cloud droplets is important, because the flight critical Mach number of cylinders is only approximately 0.4. For example, this value of Mach number corresponds to a speed of approximately 290 miles per hour at a standard NACA altitude of 10,000 feet. If important, the effect of compressibility must be considered at the speeds often used in taking multicylinder flight data. The magnitude of the compressibility effect is evaluated in this section.

ANALYSIS

In order to evaluate the magnitude of the compressibility effect on droplet impingement, trajectories in a compressible flow field around a cylinder were calculated and the resulting collection efficiencies compared with those from trajectories calculated in an incompressible flow field (section I). The differential equations that describe the motion of a droplet in a compressible flow field are the same as equations (1) and (2). Since in a compressible flow field the viscosity and density are not constant everywhere in the field, the Reynolds numbers must be written as

$$Re_0=2aU\left(\frac{\rho_a}{\mu}\right)_0 \tag{12}$$

and

$$\left(\frac{Re}{Re_0}\right)^2=\left(\frac{\rho_a}{\rho_{a,0}}\frac{\mu_0}{\mu}\right)^2[(u_x-v_x)^2+(u_y-v_y)^2] \tag{13}$$

A necessary assumption in order to solve the problem, in addition to the three presented in section I, is that the ratio of the local viscosity μ to the free-stream viscosity μ_0, appearing in equation (13), is unity. This assumption is valid, because viscosity is not appreciably affected by the order of magnitude of the changes in temperature found along a trajectory. This last assumption also permits the definition of the inertia parameter as

$$K=\frac{2}{9}\frac{\rho_w a^2 U}{\mu_0 L} \tag{14}$$

The compressible air flow around the right circular cylinder of infinite extent is described by the following equations:

$$
\left.
\begin{aligned}
u_x=&[(1-r^{-2})\cos^2\alpha+(1+r^{-2})\sin^2\alpha]+\\
&M^2\Big[\Big(-\frac{13}{12}r^{-2}+\frac{3}{2}r^{-4}-\frac{5}{12}r^{-6}\Big)\cos^2\alpha+\\
&\Big(\frac{1}{4}r^{-2}-\frac{1}{4}r^{-4}\Big)\cos\alpha\cos 3\alpha-\Big(-\frac{13}{12}r^{-2}+\frac{1}{2}r^{-4}-\frac{1}{12}r^{-6}\Big)\sin^2\alpha-\Big(\frac{3}{4}r^{-2}-\frac{1}{4}r^{-4}\Big)\sin\alpha\sin 3\alpha\Big]+\\
&M^4\Big\{(\gamma-1)\Big[\Big(-\frac{17}{60}r^{-2}+\frac{3}{8}r^{-4}-\frac{5}{12}r^{-6}+\frac{7}{16}r^{-8}-\frac{9}{80}r^{-10}\Big)\cos^2\alpha+\\
&\Big(\frac{61}{80}r^{-4}-\frac{15}{16}r^{-6}+\frac{7}{40}r^{-8}\Big)\cos\alpha\cos 3\alpha+\Big(-\frac{3}{16}r^{-4}+\frac{3}{16}r^{-6}\Big)\cos\alpha\cos 5\alpha\Big]+\\
&\Big[\Big(-\frac{137}{80}r^{-2}+4r^{-4}-\frac{65}{16}r^{-6}+\frac{35}{16}r^{-8}-\frac{33}{80}r^{-10}\Big)\cos^2\alpha+\\
&\Big(\frac{19}{48}r^{-2}+\frac{5}{16}r^{-4}-\frac{15}{16}r^{-6}+\frac{7}{24}r^{-8}-\frac{1}{16}r^{-10}\Big)\cos\alpha\cos 3\alpha+\Big(-\frac{1}{16}r^{-2}-\frac{3}{16}r^{-4}+\frac{1}{4}r^{-6}\Big)\cos\alpha\cos 5\alpha\Big]-\\
&(\gamma-1)\Big[\Big(-\frac{17}{60}r^{-2}+\frac{1}{8}r^{-4}-\frac{1}{12}r^{-6}+\frac{1}{16}r^{-8}-\frac{1}{80}r^{-10}\Big)\sin^2\alpha+\\
&\Big(\frac{61}{80}r^{-4}-\frac{9}{16}r^{-6}+\frac{3}{40}r^{-8}\Big)\sin\alpha\sin 3\alpha+\Big(-\frac{5}{16}r^{-4}+\frac{3}{16}r^{-6}\Big)\sin\alpha\sin 5\alpha\Big]-\\
&\Big[\Big(-\frac{137}{80}r^{-2}+\frac{4}{3}r^{-4}-\frac{13}{16}r^{-6}+\frac{5}{16}r^{-8}-\frac{11}{240}r^{-10}\Big)\sin^2\alpha+\\
&\Big(\frac{19}{16}r^{-2}+\frac{5}{16}r^{-4}-\frac{9}{16}r^{-6}+\frac{1}{8}r^{-8}-\frac{1}{48}r^{-10}\Big)\sin\alpha\sin 3\alpha+\Big(-\frac{5}{16}r^{-2}-\frac{5}{16}r^{-4}+\frac{1}{4}r^{-6}\Big)\sin\alpha\sin 5\alpha\Big]\Big\}
\end{aligned}
\right\}
\tag{15a}
$$

and

$$
\left.
\begin{aligned}
u_\nu=&[-r^{-2}\sin 2\alpha]+\\
&M^2\Big[\Big(-\frac{13}{12}r^{-2}+\frac{3}{2}r^{-4}-\frac{5}{12}r^{-6}\Big)\sin\alpha\cos\alpha+\Big(\frac{1}{4}r^{-2}-\frac{1}{4}r^{-4}\Big)\sin\alpha\cos 3\alpha+\\
&\Big(-\frac{13}{12}r^{-2}+\frac{1}{2}r^{-4}-\frac{1}{12}r^{-6}\Big)\sin\alpha\cos\alpha+\Big(\frac{3}{4}r^{-2}-\frac{1}{4}r^{-4}\Big)\cos\alpha\sin 3\alpha\Big]+\\
&M^4\Big\{(\gamma-1)\Big[\Big(-\frac{17}{60}r^{-2}+\frac{3}{8}r^{-4}-\frac{5}{12}r^{-6}+\frac{7}{16}r^{-8}-\frac{9}{80}r^{-10}\Big)\sin\alpha\cos\alpha+\Big(\frac{61}{80}r^{-4}-\frac{15}{16}r^{-6}+\frac{7}{40}r^{-8}\Big)\sin\alpha\cos 3\alpha+\\
&\Big(-\frac{3}{16}r^{-4}+\frac{3}{16}r^{-6}\Big)\sin\alpha\cos 5\alpha\Big]+\Big[\Big(-\frac{137}{80}r^{-2}+4r^{-4}-\frac{65}{16}r^{-6}+\frac{35}{16}r^{-8}-\frac{33}{80}r^{-10}\Big)\sin\alpha\cos\alpha+\\
&\Big(\frac{19}{48}r^{-2}+\frac{5}{16}r^{-4}-\frac{15}{16}r^{-6}+\frac{7}{24}r^{-8}-\frac{1}{16}r^{-10}\Big)\sin\alpha\cos 3\alpha+\Big(-\frac{1}{16}r^{-2}-\frac{3}{16}r^{-4}+\frac{1}{4}r^{-6}\Big)\sin\alpha\cos 5\alpha\Big]+\\
&\Big[\Big(-\frac{137}{80}r^{-2}+4r^{-4}-\frac{65}{16}r^{-6}+\frac{35}{16}r^{-8}-\frac{33}{80}r^{-10}\Big)\sin\alpha\cos\alpha+\Big(\frac{19}{48}r^{-2}+\frac{5}{16}r^{-4}-\frac{15}{16}r^{-6}+\frac{7}{24}r^{-8}-\frac{1}{16}r^{-10}\Big)\sin\alpha\cos 3\alpha+\\
&\Big(-\frac{1}{16}r^{-2}-\frac{3}{16}r^{-4}+\frac{1}{4}r^{-6}\Big)\sin\alpha\cos 5\alpha\Big]+(\gamma-1)\Big[\Big(-\frac{17}{16}r^{-2}+\frac{1}{8}r^{-4}-\frac{1}{12}r^{-6}+\frac{1}{16}r^{-8}-\frac{1}{80}r^{-10}\Big)\sin\alpha\cos\alpha+\\
&\Big(\frac{61}{80}r^{-4}-\frac{9}{16}r^{-6}+\frac{3}{40}r^{-8}\Big)\sin 3\alpha\cos\alpha+\Big(-\frac{5}{16}r^{-4}+\frac{3}{16}r^{-6}\Big)\sin 5\alpha\cos\alpha\Big]+\\
&\Big[\Big(-\frac{137}{80}r^{-2}+\frac{4}{3}r^{-4}-\frac{13}{16}r^{-6}+\frac{5}{16}r^{-8}-\frac{11}{240}r^{-10}\Big)\sin\alpha\cos\alpha+\\
&\Big(\frac{19}{16}r^{-2}+\frac{5}{16}r^{-4}-\frac{9}{16}r^{-6}+\frac{1}{8}r^{-8}-\frac{1}{48}r^{-10}\Big)\sin 3\alpha\cos\alpha+\Big(-\frac{5}{16}r^{-2}-\frac{5}{16}r^{-4}+\frac{1}{4}r^{-6}\Big)\sin 5\alpha\cos\alpha\Big]\Big\}
\end{aligned}
\right\}
\tag{15b}
$$

The first bracketed term describes the incompressible flow around the cylinder. The term with the M^2 factor and the term with the M^4 factor are, respectively, the first- and second-order corrections for the effect of compressibility on the incompressible flow field. The expression for the velocity potential, from which equations (15) were derived, was obtained from reference 23. In equations (15), α is measured counterclockwise from the x-axis of the cylinder, as is shown in figure 1.

The compressible-air velocity components in the flow field (eqs. (15)) were calculated at a Mach number of 0.4, because the effect of compressibility for completely subsonic flow is considered greatest at or near the flight critical Mach number. The value obtained for the flight critical Mach number depends on the number of correction terms applied to the incompressible flow field and appears to approach 0.4 as a limit. Results presented herein involve the maximum effect of compressibility, which restricts the free-stream velocity to a value compatible with a Mach number of 0.4.

Because of the difficulties in making precise corrections to the coefficient-of-drag term in equations (1) and (2) and to the density terms in equation (13), the problem was solved in two steps. The first step was to survey a range of values of the parameters K and φ to determine the conditions most affected by compressibility. In this first step the horizontal and vertical velocity components of the air flow computed with equations (15a) and (15b) were used. The coefficient of drag was assumed to be a function of the local Reynolds number Re only and not related to the Mach number, and the air density ratio appearing in equation (13) was assumed to be unity for this survey. Thus, only the air velocity obtained from the compressible-field calculations, not the air densities, was used in obtaining the $C_D Re/24$ term while the trajectories were calculated. In the second step, variations of air density were introduced in the equations (using the trajectories obtained in the first step as guides). These corrections to the coefficient-of-drag term and the air density variations (eq. (13)) were applied in the recalculation of the particular trajectory that showed the largest effect in the first step. The difference in the trajectories resulting from the first and second steps was less than the probable error of the analog.

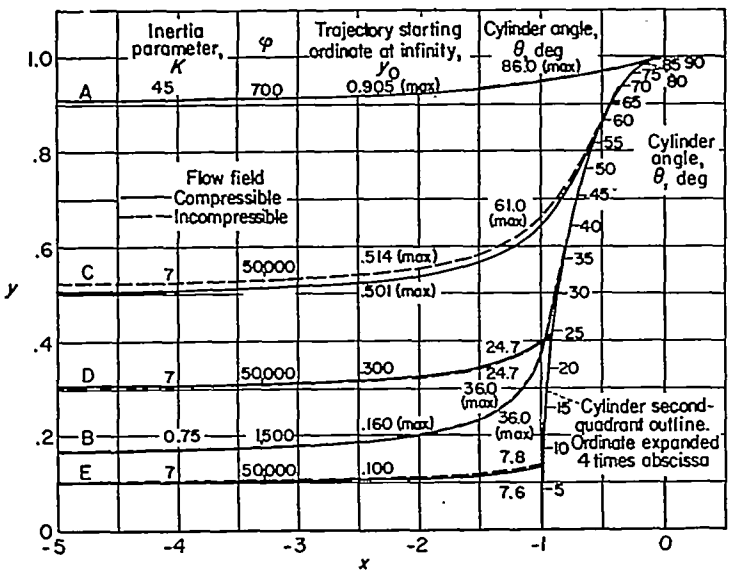

FIGURE 9.—Effect of compressibility on trajectories of droplets impinging on cylinder.

RESULTS

The solid lines in figure 9 are the trajectories for droplets in a compressible-air flow field calculated at the flight critical Mach number for the cylinder ($M_0=0.4$), and the dashed lines are the trajectories for droplets in an incompressible flow field. The set of lines labeled A are trajectories of droplets with large momentum, that is, large in size and moving with high speed. The momentum of these droplets is so large that the trajectories are nearly straight lines. One combination of operating conditions for which the trajectories A would be applicable involves a cylinder ½ inch in diameter moving with a free-stream velocity of 290 miles per hour through a cloud composed of uniform droplets approximately 26 microns in diameter at a 10,000-foot altitude. The trajectories A are tangent to the cylinder at the point of interception. The initial ordinate y_0 of the droplets at $x=-\infty$ (fig. 1) is given in figure 9.

A comparison of the trajectories computed for the compressible-air flow field with those for an incompressible flow field shows that, for droplets with large values of the inertia parameter K (trajectories A, fig. 9), the effect of compressibility is imperceptible. The effect of compressibility is also negligible on trajectories of droplets with low values of K, as shown by the set of tangent trajectories labeled B. These trajectories would apply, for example, to a cylinder 1 inch in diameter moving with a free-stream velocity of 290 miles per hour through a cloud composed of uniform droplets approximately 4 microns in diameter at a 10,000-foot altitude.

The greatest effect of compressibility on tangent trajectories is found in the middle range of the droplet inertia parameter K, as shown by the set of trajectories labeled C in figure 9. Both trajectories are tangent to the cylinder, but the droplets had to start at different ordinates in order to arrive tangent. For the droplets having trajectories C, the collection efficiency ($E=y_{0,m}$) is 0.501 if compressibility is accounted for, as compared with 0.514 when compressibility is neglected.

The effect of compressibility on the collection efficiency is shown in figure 10 as a percentage difference, which is obtained from the following relation:

$$\text{Percent difference}=\frac{E_i-E_c}{E_c}(100)$$

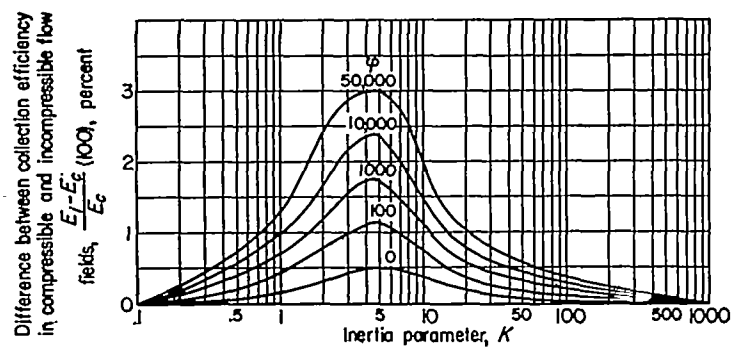

FIGURE 10.—Correction factor for compressibility effect.

where the values for E_i are obtained from the collection efficiency presented in figure 4 for the incompressible flow field. The greatest difference is about 3 percent at the conditions of $K=5$ and $\varphi=50{,}000$. The following tabulation summarizes the effect of compressibility as a percentage difference between results computed in a compressible and an incompressible flow field. Typical values of dimensions and flight conditions are involved in the examples given. All calculations were made for 290 miles per hour, which is near the critical speed for cylinders at the 10,000-foot NACA standard altitude:

Inertia parameter, K	Cylinder diameter, D, in.	Droplet diameter, d, microns	Parameter φ	$\frac{E_i-E_c}{E_c}(100)$, percent
0.5	0.5	3	740	0.3
	1	4	1,480	.4
	3	7	4,440	.5
	6	9	8,880	.5
1	0.5	4	740	0.6
	1	5	1,480	.8
	3	9	4,440	.9
	6	13	8,880	1.0
5	0.5	9	740	1.5
	1	12	1,480	1.9
	3	21	4,440	2.1
	6	30	8,880	2.3
	18	50	27,650	2.8
	30	70	44,400	2.9
20	0.5	17	740	0.5
	1	24	1,480	.6
	3	40	4,440	.7
	6	60	8,880	.8

DISCUSSION

From the results of the tabulation and of figure 10, it may be concluded that for a cylinder the effect of compressibility of the air on the droplet trajectories is not very great up to the flight critical Mach number; and, for most practical problems involving measurements of droplet impingement on cylinders, the compressibility effect may be ignored.

The reason that the effect of compressibility on droplet trajectories is almost negligible is found by comparing the compressible and the incompressible flow fields. The effect of compressibility is most pronounced on those streamlines close to the cylinder. The compressibility effect decreases very rapidly with distance away from the surface of the cylinder and everywhere becomes negligible 1 cylinder radius away from the surface. Furthermore, the effect of compressibility is of consequence only over the top portion of the cylinder, as shown in figure 11. Comparison of compressible and incompressible tangential air-flow velocities on the cylinder surface (fig. 11) shows that the effect is pronounced only for $\theta>60°$. The angle is measured from the same reference line as in figure 1.

Droplets forming the solid-line trajectory A in figure 9 are acted on, during the last portion of the trajectory, by

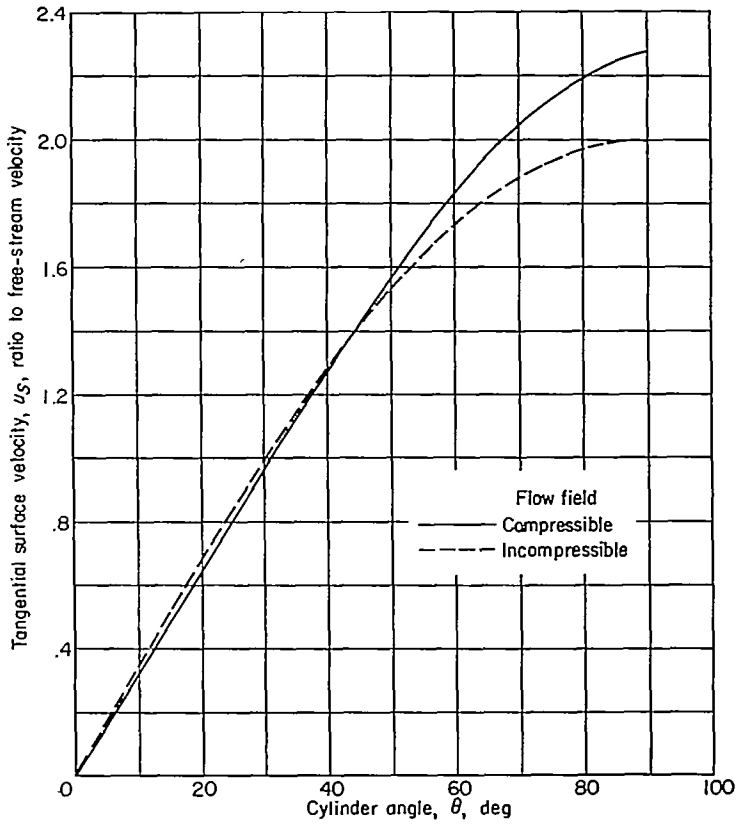

FIGURE 11.—Comparison of surface velocity on cylinder in compressible and incompressible flow fields at approximately flight critical Mach number.

air streamlines that have a different pattern from the air streamlines for an incompressible flow field; however, the inertia of these droplets is so large that the last portion of their path is not influenced appreciably by the compressibility of the air flow. The droplets with low inertia (trajectories B, fig. 9) are always in the flow-field region where there is no appreciable difference between the compressible and incompressible air flows. The last portions of the tangent trajectories (C) of droplets in the middle range of inertia are affected by compressibility. Droplets with trajectories D and E have the same middle range of inertia as those with trajectories C. Trajectories D and E are not influenced by compressibility for the same reason that trajectory B was not influenced.

The sample trajectories presented in figure 9 summarize the effect of compressibility over the complete range of values studied for the parameters K and φ. The small effect of compressibility is most noticeably pronounced on collection efficiency (fig. 10). The effect on the maximum angle of impingement θ_m was within the accuracy of the analog. The effect on trajectories intermediate between the tangent trajectory and the x-axis is imperceptible (trajectories D and E, fig. 9). For this reason, the values of the local impingement efficiency β are not noticeably affected by compressibility; however, the cumulative effect on β—that is, $\int_0^{\theta_m} \beta \, d\theta = E$—results in the effect shown in figure 10.

III. THEORY OF ROTATING MULTICYLINDER METHOD

As was discussed in the **INTRODUCTION** to this report, an important application of droplet-trajectory data with respect to cylinders has been in the measurement of droplet size and liquid-water content in icing clouds. Several cylinders of different diameters are exposed from an airplane in flight to the supercooled droplets in the icing cloud. The number of supercooled droplets that strike and freeze on the cylinders is a function of the cylinder size and of the flight and atmospheric conditions, as well as the inertial properties of the droplets. The liquid-water content and droplet-size distribution in the cloud are determined by a comparison of the measured weight of ice collected on each of the cylinders with the amount of droplet impingement obtained from the calculated water-droplet trajectories for cylinders of the same size and for the same flight and atmospheric conditions. A brief discussion of the basic theory of the multicylinder method is presented in this section.

BASIC CONCEPT

The mass of ice collected per unit space swept out by a rotating cylinder exposed in a supercooled cloud is given by

$$wE=\frac{m}{2L\bar{U}t} \tag{16}$$

For clouds composed of droplets of uniform size, the collection efficiency E is given in section I in terms of the dimensionless parameters

$$K=\frac{2}{9}\frac{\rho_w a^2 U}{\mu L} \tag{3}$$

and

$$\varphi=\frac{18\rho_a{}^2 LU}{\mu\rho_w} \tag{7}$$

It is assumed that w, ρ_w, ρ_a, U, and μ do not vary during the exposure period.

When several cylinders of different radii are exposed simultaneously from an airplane flying in a supercooled cloud, all the quantities on the right side of equations (3) and (7), with the exception of the cylinder radius L, are the same for each of the cylinders; hence, if L is eliminated by combining equations (3) and (7), the resulting parameter

$$K\varphi=\left(\frac{2\rho_a aU}{\mu}\right)^2 \tag{17}$$

has the same value for each cylinder of the set. Thus, it is evident that the mathematical condition that $K\varphi$ is the same for all cylinders corresponds to the physical situation assumed to exist during the exposure of a multicylinder set in flight. The only unknown quantity on the right side of equation (17) is the droplet size a. For a given simultaneous exposure of several cylinders of different radii, the mass of ice collected per unit frontal area of each cylinder is proportional to the collection efficiency E of each cylinder (eq. (16)) and $1/K$ is proportional to L (eq. (3)). Therefore, any functional relation between calculated values of E and $1/K$, when $K\varphi$ is constant, is also analogous to the functional relation between the measured ice collected per unit space swept out by the cylinder and the cylinder radius. The latter relation is given by a plot of the flight data. The basic concept states that a theoretically determined curve of E as a function of $1/K$ exists that is identical to the curve defined by the flight data, except for scale factors. This relation provides the basis in subsequent sections for comparing the measured weight of ice collected on each cylinder with the calculated water-droplet collections for the same cylinders and conditions. From these comparisons the droplet sizes and liquid-water contents of the clouds are obtained.

NONUNIFORM CLOUDS

DROPLET-SIZE DISTRIBUTION PATTERNS

The data presented in figures 2 to 10 apply directly only to clouds composed of droplets all of which are uniform in size. In a cloud in the earth's atmosphere, the water droplets are often not of uniform size. For a cylinder exposed in a cloud with a given droplet-size distribution pattern, the trajectory data in the figures cited are used to compute other curves that are applicable to the distribution pattern under consideration.

Five different droplet-size distribution patterns are defined in reference 3 for convenience in the classification of clouds. The table of distribution patterns, reproduced herein as table II, was adopted to cover some of the range believed to be encountered in nature. Although the five distributions given in table II are not the only probable patterns existing in clouds, these five distributions are used herein to discuss the theory and procedure of the rotating multicylinder method. The methods of analysis applied to these patterns can be used for similar study of other droplet-size distribution patterns. The droplet-size ratios given in table II are the average radius of the droplets in each group to the radius a_o of the volume-median droplet size. (The amount of water in all the droplets of a diameter greater than the volume-median droplet diameter is equal to the amount of water in all the droplets of smaller diameter.) The different distribution patterns are labeled with the first five letters of the alphabet. A cloud with an A distribution is composed of droplets which are all uniform in size. In a cloud with a B distribution, 30 percent of the water is contained in droplets having the volume-median droplet diameter, 20 percent in droplets with a diameter 0.84 of the volume-median droplet diameter, and another 20 percent in droplets

TABLE II.—FIVE ASSUMED DISTRIBUTIONS OF DROPLET SIZE (REF. 3)

Total liquid water in each size group, percent	a/a_o				
	Distributions				
	A	B	C	D	E
5	1.00	0.56	0.42	0.31	0.23
10	1.00	.72	.61	.52	.44
20	1.00	.84	.77	.71	.65
30	1.00	1.00	1.00	1.00	1.00
20	1.00	1.17	1.26	1.37	1.48
10	1.00	1.32	1.51	1.74	2.00
5	1.00	1.40	1.81	2.22	2.71

The size is expressed as the ratio of the average drop radius in each group to the volume-median drop radius a_o.

Example of interpretation: 30 percent of the liquid-water content of any cloud is contained in droplets which have a radius a_o. In the case of the B distribution, 20 percent of the liquid-water content is contained in droplets which have a radius smaller than the volume-median radius a_o by a ratio a/a_o=0.84 and another 20 percent in droplets which have a radius larger than a_o by a ratio a/a_o=1.17. A similar interpretation applies to the remaining values.

with a diameter 1.17 times as large as the volume-median droplet diameter. The remaining water is distributed as follows: 10 percent in droplets with a diameter 0.72 of the volume-median diameter, 10 percent in droplets 1.32 times as large, 5 percent in droplets 0.56 as large, and 5 percent in droplets 1.49 times as large as the volume-median diameter. A similar interpretation applies to the other distributions listed in table II.

OVER-ALL WEIGHTED COLLECTION EFFICIENCY

In a cloud composed of droplets of many different sizes, a cylinder of a given diameter will collect some droplets of every size; however, the collection efficiency with the smaller droplets will be less than with the larger droplets. For any assumed droplet-size distribution in the cloud, such as distribution B in table II, an over-all weighted collection efficiency for a cylinder can be calculated from the results of figure 4 by adding together the weighted collection efficiencies that are appropriate to each droplet-size group in the B distribution. For example, 30 percent of the water in all droplets in the cloud is assumed to be processed by the cylinder at the collection efficiency pertaining to the volume-median droplet; 20 percent of the water in all the droplets in the cloud is assumed to be processed by the cylinder at the lower collection efficiency that applies to droplets with diameters 0.84 as large as the volume-median droplet diameter, and so forth. The over-all weighted collection efficiency for each cylinder in the set of cylinders exposed from the airplane can be calculated for the assumed distribution. A different curve of over-all weighted collection efficiency E_ω as a function of cylinder diameter will exist for each assumed droplet-size distribution.

COMPARISON CURVES

The droplet-size distribution prevailing in a cloud at the time of measurement can be found by comparing the shape of a curve of cylinder radius as a function of the measured ice accumulated in flight on each cylinder per unit space swept out by the cylinder with the shape of the calculated curves of cylinder radius as a function of over-all weighted collection efficiency. (Sets of calculated curves for comparison are shown in fig. 12 for droplet-size distributions A to E of table II. The detailed method of calculating these curves, which differs slightly from that presented in ref. 3, is discussed in appendix D.) The correspondence that has been shown to exist between calculated values of the collection efficiency and the ice collected in the case of uniform droplets (eq. (16)), as well as the relation between K and L (eq. (3)), applies also for nonuniform droplet-size distributions when E and K are replaced by E_ω and K_o. (K_o is obtained by substituting a_o for a in eq. (3).) Thus, the relation between calculated values of E_ω and $1/K_o$, when $K_o\varphi$ is constant, corresponds to the relation between measured amounts of ice collected per unit space swept out by the cylinder and cylinder radius. In order to cover the more probable conditions of airplane speed, air viscosity and density, and volume-median droplet size, five values of $K_o\varphi$ ranging from 0 to 10,000 were chosen for calculation of comparison curves and are presented in figure 12. Values of E_ω are also presented in table III for the five selected values of $K_o\varphi$ (0, 200, 1000, 3000, and 10,000) that are herein called standard values.

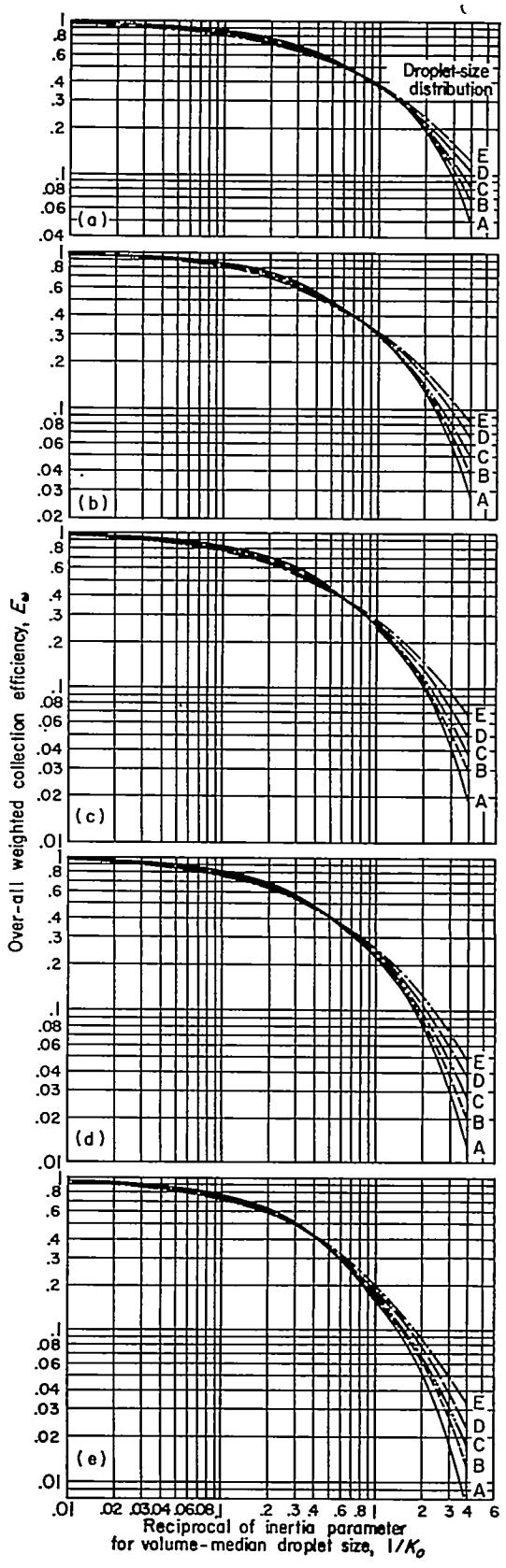

(a) $K_o\varphi$, 0.
(b) $K_o\varphi$, 200.
(c) $K_o\varphi$, 1000.
(d) $K_o\varphi$, 3000.
(e) $K_o\varphi$, 10,000.

FIGURE 12.—Over-all weighted collection efficiency as function of reciprocal of inertia parameter for volume-median droplet size for five cloud droplet-size distributions.

TABLE III.—CALCULATED VALUES OF CYLINDER COLLECTION EFFICIENCY FOR STANDARD VALUES OF $K_o\varphi$

$1/K_o$	A		B		C		D		E
	E_ω	$0.6E_\omega$	E_ω	$0.7E_\omega$	E_ω	$0.8E_\omega$	E_ω	$0.9E_\omega$	E_ω
$K_o\varphi=0$									
4.00	0.051	0.031	0.069	0.048	0.085	0.068	0.107	0.096	0.126
2.00	.205	.123	.204	.143	.211	.169	.225	.203	.241
1.00	.380	.228	.374	.262	.373	.298	.379	.341	.384
.50	.566	.340	.555	.389	.549	.439	.542	.488	.536
.20	.789	.473	.768	.538	.750	.600	.732	.659	.713
.10	.885	.531	.870	.609	.854	.683	.836	.752	.815
.05	.932	.559	.925	.648	.918	.734	.898	.808	.885
.02	.963	.578	.961	.673	.957	.766	.951	.856	.940
.01	.978	.587	.976	.683	.977	.782	.972	.875	.965
$K_o\varphi=200$									
4.00	0.027	0.016	0.039	0.027	0.050	0.040	.066	0.059	0.083
2.00	.135	.081	.138	.097	.146	.117	.165	.149	.182
1.00	.298	.179	.302	.211	.306	.245	.315	.284	.319
.50	.493	.296	.486	.340	.482	.386	.480	.432	.477
.20	.761	.457	.740	.518	.721	.577	.703	.633	.686
.10	.874	.524	.859	.601	.846	.677	.826	.743	.805
.05	.925	.555	.919	.643	910	728	901	811	.878
.02	.960	.576	.959	.671	.955	.764	.948	.853	.938
.01	.976	.586	.975	.683	.976	.781	.971	.874	.963
$K_o\varphi=1000$									
4.00	0.019	0.011	0.029	0.020	0.038	0.030	0.050	0.045	0.065
2.00	.109	.065	.109	.076	.122	.098	.138	.124	.154
1.00	.251	.151	.252	.176	.259	.207	.271	.244	.283
.50	.460	.276	.452	.316	.423	.338	.447	.402	.447
.20	.714	.428	.697	.488	.677	.542	.661	.595	.643
.10	.830	.498	.816	.571	.800	.640	.783	.705	.763
.05	.908	.545	.899	.629	.892	.714	.876	.788	.862
.02	.953	.572	.953	.667	.949	.759	.943	.849	.933
.01	.971	.583	.972	.680	.973	.778	.967	.870	.962
$K_o\varphi=3000$									
4.00	0.013	0.008	0.020	0.014	0.027	0.022	0.039	0.035	0.048
2.00	.085	.051	.090	.063	.100	.080	.111	.100	.130
1.00	.218	.131	.225	.158	.235	.188	.244	.220	.251
.50	.409	.245	.416	.291	.410	.328	.415	.374	.413
.20	.687	.412	.668	.468	.652	.522	.641	.577	.623
.10	.815	.489	.797	.558	.785	.628	.766	.689	.746
.05	.884	.530	.878	.615	.867	.694	.855	.770	.839
.02	.945	.567	.940	.658	.938	.750	.921	.829	.918
.01	.968	.581	.966	.676	.970	.776	.964	.868	.954
$K_o\varphi=10,000$									
4.00	0.008	0.005	0.013	0.009	0.017	0.014	0.023	0.021	0.034
2.00	.057	.034	.060	.042	.072	.058	.083	.075	.092
1.00	.157	.094	.163	.114	.172	.138	.188	.169	.202
.50	.350	.210	.356	.249	.357	.286	.362	.326	.368
.20	.645	.387	.630	.441	.615	.492	.599	.539	.591
.10	.778	.467	.764	.535	.748	.598	.731	.658	.713
.05	.865	.519	.857	.600	.849	.679	.830	.747	.816
.02	.920	.552	.920	.644	.918	.734	.909	.818	.899
.01	.952	.571	.950	.665	.955	.764	.946	.851	.939

DETERMINATION OF DROPLET SIZE, LIQUID-WATER CONTENT, AND NOMINAL DROPLET-SIZE DISTRIBUTION

The fact that the mass of ice per unit space swept out by the cylinder is proportional to E_ω is expressed by an equation obtained from the identity $E_\omega \equiv wE_\omega/w$ and equation (16). The equation is written in logarithmic form in order to make the proportionality constant appear as an additive term:

$$\log E_\omega \equiv \log wE_\omega - \log w = \log \frac{m}{2LlUt} - \log w \qquad (18)$$

Similarly, since LK_o is the same for all values of L during a given exposure of the cylinder set, as shown by equation (3), a proportionality between $1/K_o$ and L is conveniently expressed by the identity

$$\log 1/K_o \equiv \log L - \log LK_o \qquad (19)$$

The additive terms $\log w$ and $\log LK_o$ in equations (18) and (19), respectively, permit the translation of the axes of a curve of $\log E_\omega$ as a function of $\log 1/K_o$ with respect to the axes of another curve of $\log wE_\omega$ as a function of $\log L$, so that the two curves coincide if the physical conditions for which the two curves were obtained are the same.

The flight data are plotted in terms of the coordinates $\log wE_\omega$ as a function of $\log L$ as shown in figure 13, and the calculated data of table III are plotted in terms of $\log E_\omega$ and $\log 1/K_o$. The comparison of experimental points and calculated curves is valid if $K_o\varphi$ is approximately the same for both and if the assumed droplet-size distribution applicable to the calculated curve is similar to the actual droplet-size distribution in the cloud. The translation of axes is illustrated in figure 14, in which the data points, which are obtained from actual flight measurements, are plotted in terms of $\log wE_\omega$ and $\log L$ with respect to the axes shown by the dashed lines. The theoretical curve of $\log E_\omega$ as a function of $\log 1/K_o$, which applies to droplet-size distribution E when $K_o\varphi=3000$ (table III), is plotted with respect to the axes shown by the solid lines. The vertical axes of the two sets of coordinates are separated by an interval equal to $\log LK_o$, and the horizontal axes are separated by an interval equal to $\log w$. When the plotted points are correctly matched with the calculated curve, the separation of the axes provides values of $\log LK_o$ and $\log w$ that are used to calculate the volume-median droplet radius (eq. (3)) and the liquid-water content.

Because the shape of the calculated curves of $\log E_\omega$ as a function of $\log 1/K_o$ depends upon the assumed droplet-size distribution, curves based on the various assumed distributions listed in table II are matched against the experimental plot of $\log wE_\omega$ as a function of $\log L$, and the curve which most closely fits the data points is used in the determination

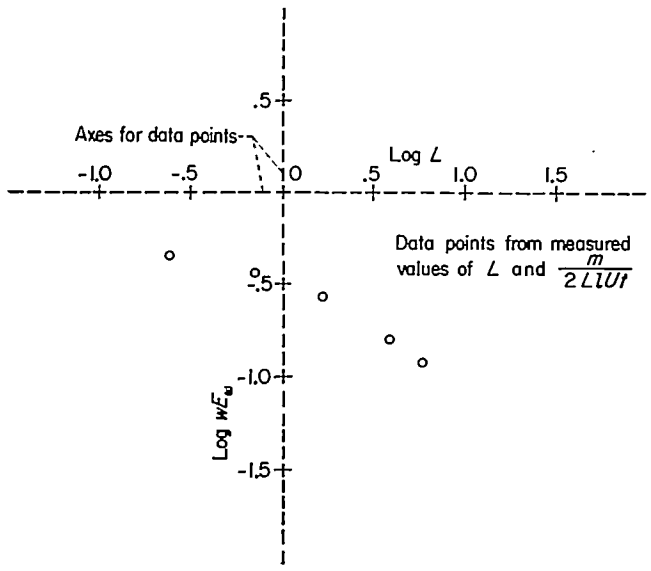

FIGURE 13.—Illustration of plotted flight data to be used in comparison.

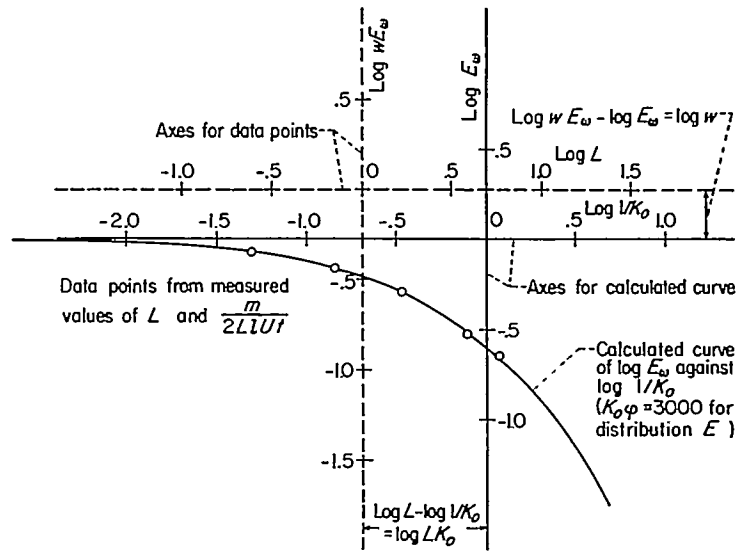

FIGURE 14.—Comparison of measured ice-collection data with calculated collection-efficiency curve.

of liquid-water content and droplet diameter. The assumed droplet-size distribution corresponding to this chosen curve is taken as an approximate representation of the degree of homogeneity of the actual cloud-droplet distribution. If the actual droplet-size distribution in a cloud is not of the same general form as the assumed distributions (e. g., if the distribution is bimodal), the value of droplet diameter obtained by using the procedure described herein is not necessarily the volume-median diameter. For this reason, some investigators prefer to use the term "mean effective diameter" when referring to the results of multicylinder measurements of droplet size.

In order to fulfill the requirement that approximately the same value of $K_o\varphi$ must apply to both the experimental and calculated data, a procedure of successive approximations is necessary. As described in the calculation procedures of section IV, an estimated standard value of $K_o\varphi$ is used to determine an approximate value of LK_o that is used to calculate a corrected value of $K_o\varphi$. The standard value of $K_o\varphi$ that is nearest to this calculated value is then used in the final determination of w and a_o. This procedure is practicable because large errors in estimating $K_o\varphi$ cause only small changes in LK_o. Since curves are available for only a few standard values of $K_o\varphi$, the value of $K_o\varphi$ for the flight data is generally not the same as for the calculated curve. This difficulty is not serious, because the curves of log E_ω as a function of log $1/K_o$ for successive standard values of $K_o\varphi$ are nearly identical except for slight displacement in the direction of the axis of log $1/K_o$. Since this displacement is a known function of $K_o\varphi$, the value of droplet radius may be corrected by the use of a correction factor that depends on the corrected value of $K_o\varphi$ and the standard value applicable to the curve used in determining a_o. This correction factor is also discussed in section IV.

IV. APPARATUS AND PROCEDURE FOR MEASURING LIQUID-WATER CONTENT AND DROPLET SIZES IN SUPERCOOLED CLOUDS BY ROTATING MULTICYLINDER METHOD

The basic steps involved in the application of the multicylinder method are essentially as follows:

(1) Exposing set of cylinders of different sizes in supercooled cloud for measured time at known pressure altitude, true airspeed, and ambient temperature
(2) Disassembling and storing ice-covered cylinders in separate water-proof containers
(3) Weighing individual cylinders plus containers in both wet and dry conditions to obtain net weight of collected ice
(4) Determining liquid-water content, droplet size, and droplet-size distribution by comparing measured weight of ice collected on each cylinder with theoretical computations for comparable cylinders and comparable flight and atmospheric conditions

These basic steps are discussed in detail in this section.

APPARATUS

The following pieces of equipment are used for taking multicylinder data during flight:

(a) Cylinder sets
(b) Shafts and transition segments.
(c) Plastic bags (large and small) with rubber bands for sealing
(d) Carrying case for cylinder sets, shafts, and transition segments

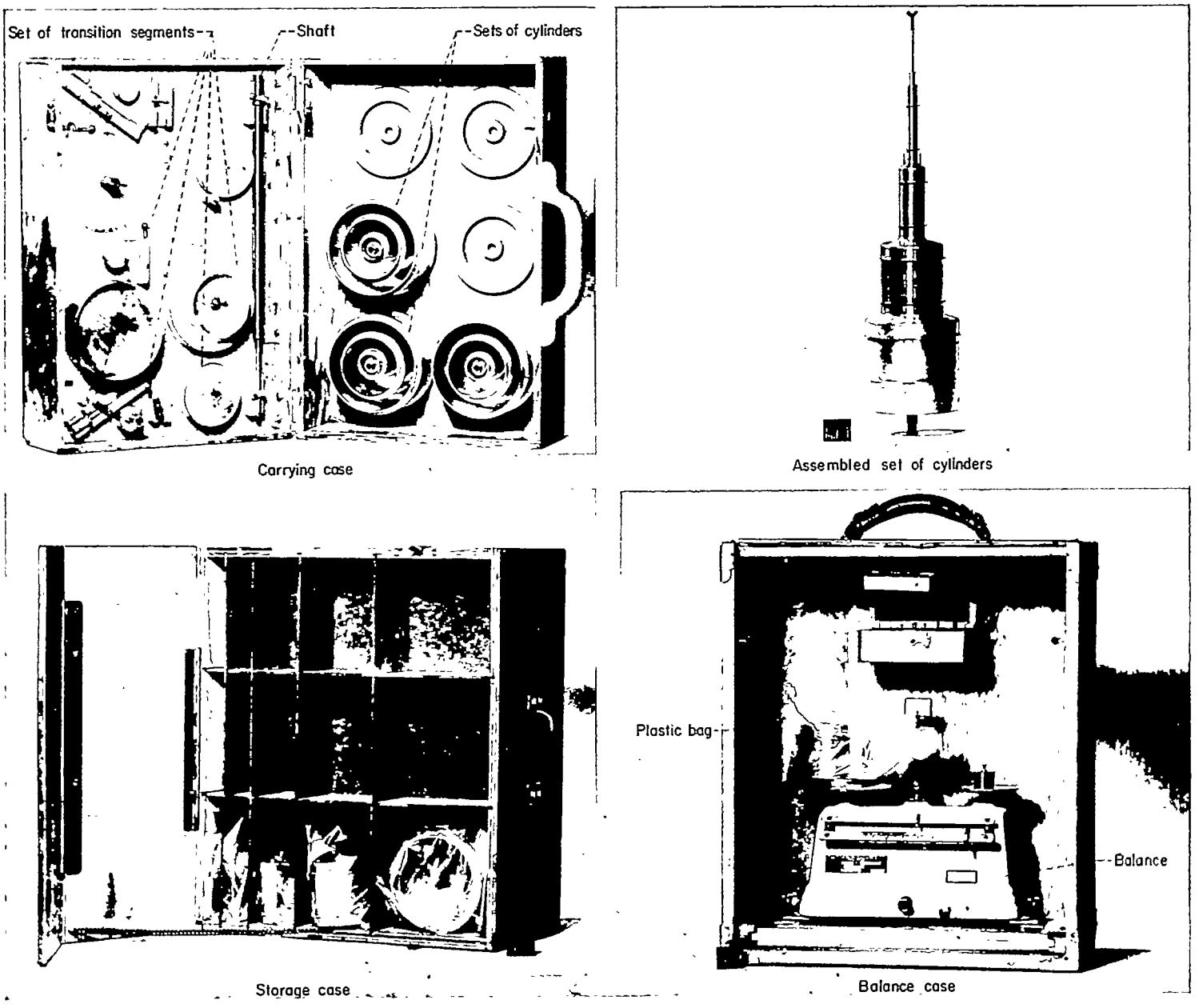

FIGURE 15.—Multicylinder kit.

(e) Cold box for storage and disassembly of iced cylinders
(f) Box with compartments (not refrigerated) for storing cylinders in sealed bags after disassembly
(g) Rotating drive unit and mast mounted on sliding platform supported by guide rails
(h) Stop watch
(i) Free-air temperature indicator, altimeter, and airspeed indicator

Auxiliary items necessary for use on the ground after the flight are:

(j) Set of balances (accuracy, ±0.01 g)
(k) Drying rack for plastic bags

The essential components of this equipment, including a set of balances, an assembled multicylinder unit, and a carrying case for cylinder sets, are shown in figure 15. The details of an assembled set of cylinders are shown in figure 16. The standard set includes five 2-inch-long cylinders with diameters of ⅛, ½, 1¼, 3, and 4½ inches. The set is arranged with flanges attached to the ends of the cylinder elements in order to establish precisely the length of the ice samples and to provide for ease in disassembly after exposure to an icing cloud. The transition pieces are designed for minimum distortion of the air-flow field from the required two-dimensional flow pattern around the cylinders.

An assembled set of cylinders is shown in figure 17 extended through the top of the airplane fuselage. A sliding platform, which does not extend through the fuselage, supports the cylinder assembly on a 2-foot mast in such a manner that the entire assembly can be moved to a position in which the mast will be extended into the ambient air stream a sufficient distance to be reasonably free from aerodynamic effects introduced by the fuselage. The alteration of the concentration of cloud droplets in the immediate vicinity of an aircraft moving through a cloud is discussed in reference 8. A qualitative knowledge of the spatial variation of local

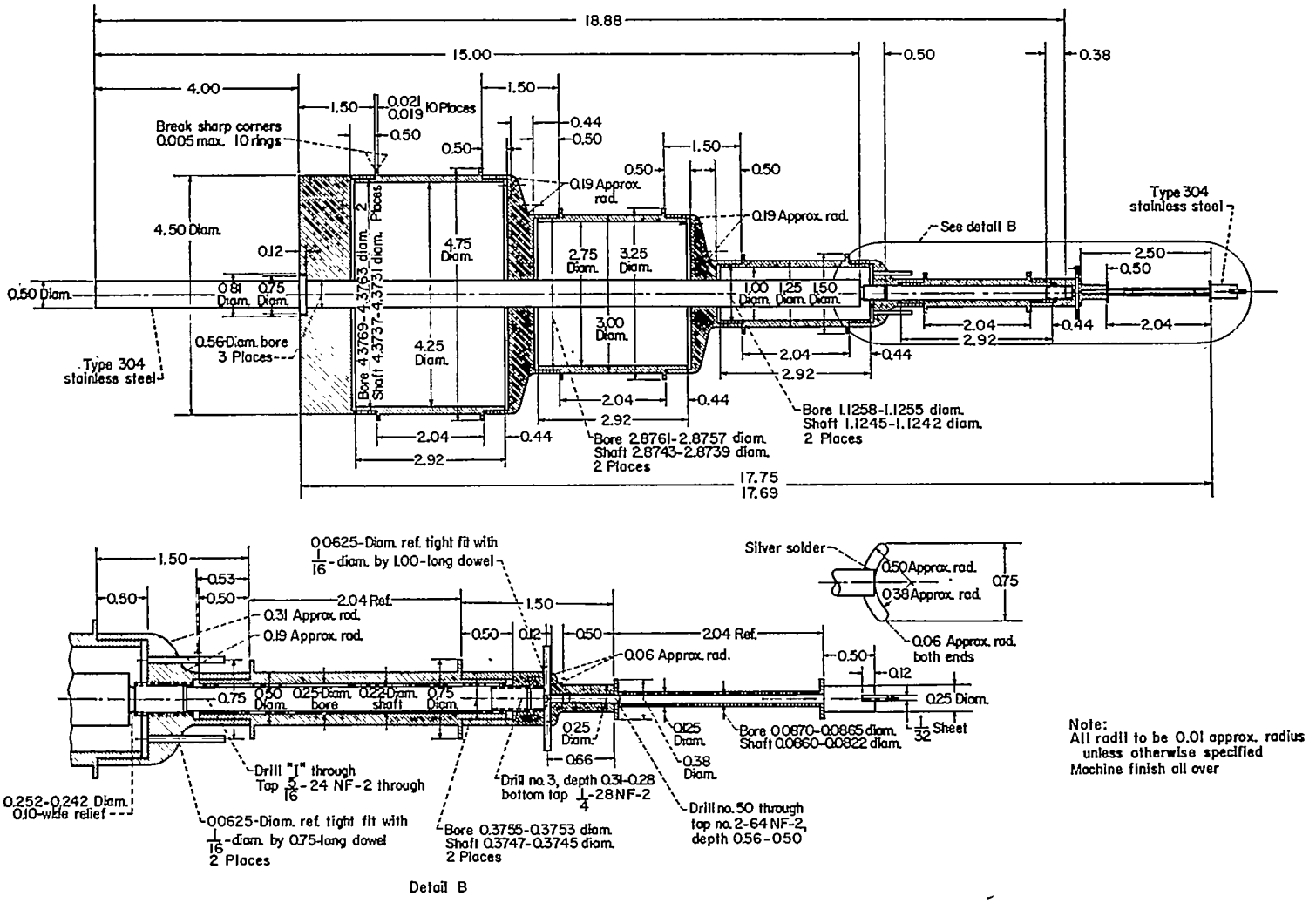

FIGURE 16.—Details of assembled set of cylinders. (Dimensions in inches.)

droplet concentration about the aircraft can be obtained by extending rods from the fuselage during an icing encounter. The details of construction of the sliding platform, the guide rails, and the supporting structure vary depending on the location of the apparatus and the type of airplane. A drive unit, which is also mounted on the sliding platform, rotates the supporting mast and multicylinder assembly at a speed of about 80 rpm (speed not critical ±20 rpm).

The wooden cold box used for disassembling is large enough to hold one or more assembled sets of multicylinders, so that, if the cylinders cannot be disassembled immediately following an exposure, the cold box can be used for storage for short times. Disassembly of the cylinders is facilitated when the cylinders are in the vertical position; therefore, the box is so constructed that one side and the top can be opened. The other three sides of the box are surrounded with dry ice. Sockets are provided in the bottom of the box for insertion of the driving shaft, which acts as a support for the cylinders.

The ambient air temperature may be measured by any convenient type of thermometer, but the temperature element must be shielded from direct water impingement in order to prevent heat-of-fusion effects. The airspeed used in the calculations is the speed of the air with respect to the airplane at the point in the field of flow about the fuselage at which the cylinders are to be exposed. The relation between the true airspeed of the airplane, obtained with the airspeed indicator that is part of the original equipment on the airplane, and the required local airspeed may be determined experimentally for any particular installation by means of a static-pressure survey. If an appreciable variation (approx. 2 percent) of local airspeed exists along a line with the same length and direction as the cylinder assembly, another exposure location on the airplane must be selected. Effects caused by propellers and protruding objects can be evaluated with a static-pressure survey.

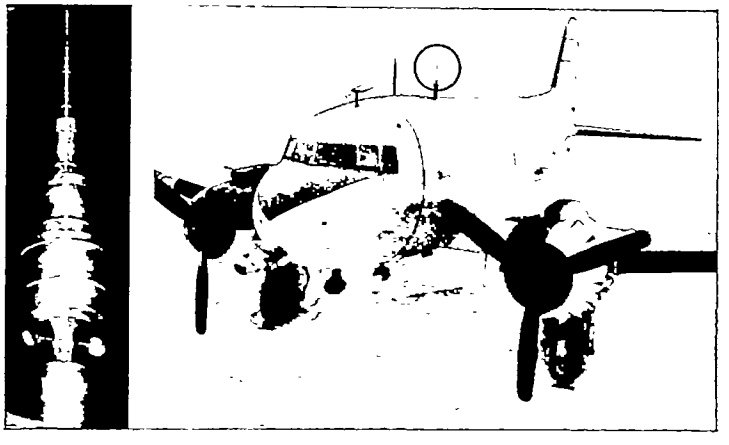

FIGURE 17.—Rotating multicylinder set extended through top of airplane fuselage.

PROCEDURE

OPERATION

The following procedure and precautions are taken to ensure sufficient and reliable data:

(1) Three sets of cylinders are assembled before flight or before entry into suspected icing conditions.

(2) All unmounted cylinders are in the carrying rack within convenient reach of the operators.

(3) Plastic bags are marked according to run number before take-off.

(4) When test conditions are established, a set of cylinders is exposed to the air stream for a period of 1 to 5 minutes, depending upon the rate of ice formation. The ice thickness should always be less than the width of the flanges on the ⅛-inch-diameter cylinder. The period of exposure is measured to the nearest second and recorded. In order to minimize the errors associated with large percentage changes in cylinder radius, the exposure period is just long enough to obtain ice samples that can be weighed to an accuracy of 2 percent. The airspeed is held as nearly constant as possible during exposure.

(5) The time involved in extending or retracting the cylinders is kept as short as possible in order to minimize the difference in exposure time between the large and the small cylinder.

(6) The complete assembly is placed in the cold box during the disassembling period.

(7) In the disassembling procedure, the ice is carefully scraped off the thin flanges at the ends of the cylinders in order to ensure that only ice collected on the cylinders is weighed. If a small amount of ice is lost from a cylinder, the percentage of loss is estimated and recorded. (A pair of pliers is necessary occasionally in order to loosen some of the transition segments frozen on the cylinders or shafts. Drying each part with a cloth before reassembling will help to prevent adherence between the parts after exposure.)

(8) The plastic bags in which the ice-coated cylinders are placed are sealed with rubber bands and deflated to prevent bursting with increase in altitude.

(9) The ice-coated cylinders are arranged in systematic order in the storage box. The sealed bags are handled carefully to prevent breakage of bags and possible damage to the cylinders.

WORK SHEET I WITH SAMPLE DATA FROM AN OBSERVATION

(1) Average indicated airspeed, mph	171
(2) Average true airspeed, Γ, mph	185
(3) Average local airspeed, V, mph	191
(4) Pressure altitude, Z_p, ft	7000
(5) Uncorrected air temperature, °C	−10.1
(6) Wet-air temperature correction, °C	−2.1
(7) Corrected temperature, T, °C	−12.2
(8) Exposure period, t, sec	216
(9) φ/DV, hr/(mile)(in.)	6.7

	Cylinder diameter, D, in.				
	⅛	½	1¼	3	4½
(10) Gross weight, g	7.44	23.56	59.68	141.83	190.47
(11) Tare weight, g	6.34	20.94	55.16	135.61	183.41
(12) Net weight of ice, g	1.10	2.62	4.52	6.22	7.06
(13) Corrected net weight, m^*, g	1.10	2.62	4.52	6.22	7.06
(14) D_{ice}, in.	.191	.554	1.291	3.024	4.518
(15) w^*E_ω, g/cu m	.242	.199	.147	.086	.066

	a First approximation	b Second approximation	c Final values
(16) $K_o\varphi$ (nearest standard)	3000	3000	----------
(17) DK_o, in.	3.86	----------	3.86
(18) $K_o\varphi$ (corrected)	4940	----------	4940
(19) Droplet diam. (uncorrected), microns	----------	----------	13.3
(20) Droplet-size distribution	E	----------	E
(21) w^*, g/cu m	0.30	----------	0.30

(22) Droplet-diameter correction factor	1.033
(23) Mean effective droplet diameter, d, microns	13.7

(10) Pressure altitude, free-air temperature, and indicated airspeed, averaged over the exposure period, are recorded during exposure. The airspeed is determined as accurately as practicable; approximate values of pressure altitude and temperature are satisfactory.

(11) After the flight, each cylinder and its plastic bag are weighed together to the nearest 0.01 gram. After the initial weighing, drying of the bags is expedited by turning them inside out. Care should be exercised in making certain that each cylinder is weighed dry with the same rubber band and bag used in the initial weighing.

CALCULATION

Computed values of collection efficiency presented in section III, ice-collection data obtained with the rotating cylinders, and flight data expressed in terms of working parameters are used to determine cloud liquid-water content and droplet size. The working parameters are φ/DV, which involves the factors of pressure altitude and air temperature, and wE_ω, which is the amount of ice collected per unit space swept out by the cylinders.

It is convenient to record the flight data and the computation steps in a systematic form, such as the work sheet shown herein. In the detailed calculation procedure that follows, reference is made to the various numbered items listed in work sheet I. Equations (1) to (19) are true with any consistent system of units, such as feet, slugs, and seconds. For practical reasons, certain departures from consistent units are desirable for routine use. Thus, in the detailed STEPWISE CALCULATION PROCEDURE described in the next section, a (droplet radius in ft) is replaced by d (droplet diameter in microns); U (ft/sec) by V (mph); w (slugs/cu ft) by w^* (g/cu m); L (cylinder radius in ft) by D (cylinder diameter in inches); and m (slugs) by m^* (grams). Certain numerical conversion factors appear in the calculations because of these changes of units. Also, for routine calculations it is convenient to use logarithmic graph paper for the curve-matching procedure, thus making it unnecessary to use numerical values of the logarithms.

Before proceeding with the calculations, the flight data are recorded as items (1), (4), (5), and (8). The weight of ice on each cylinder is entered as item (12). Corrections for any loss of ice are made, and the corrected weights are entered as item (13).

STEPWISE CALCULATING PROCEDURE

(a) **Average local airspeed.**—The average true airspeed (item (2)) is obtained by correcting, in the usual manner, the average indicated airspeed (item (1)) for air density effects. The average local airspeed to be entered in item (3) is the true airspeed corrected (if required) for effects caused by the fuselage of the airplane. This correction factor is obtained by the static-pressure survey mentioned in the section on APPARATUS.

(b) **Free-air temperature.**—The wet-air temperature correction (item (6)) is obtained from the relation (ref. 24)

$$\Delta T = -\sigma\Gamma^2 \frac{\zeta_s}{\zeta_d} \times 10^{-4}$$

where Γ is the average true airspeed (item (2)). Although the recovery factor is influenced to a slight extent by several factors, including shape, thermal conductivity, and location of the temperature probe, a value of 0.85 for σ is suggested unless a calibration of the installation is available. The lapse-rate ratio ζ_s/ζ_d is given in figure 18 as a function of the pressure altitude and temperature (items (4) and (5)). When the corrected temperature (item (7)) is used, small inaccuracies in the temperature ($\pm 2°$ C) do not appreciably affect the final results.

(c) **Parameter φ/DV.**—The parameter φ/DV is a convenient means of introducing the effects of altitude and temperature into the calculations required for the determination of droplet size and droplet-size distribution. The value of φ/DV (item (9)) is obtained from figure 19, in which the corrected temperature (item (7)) is used.

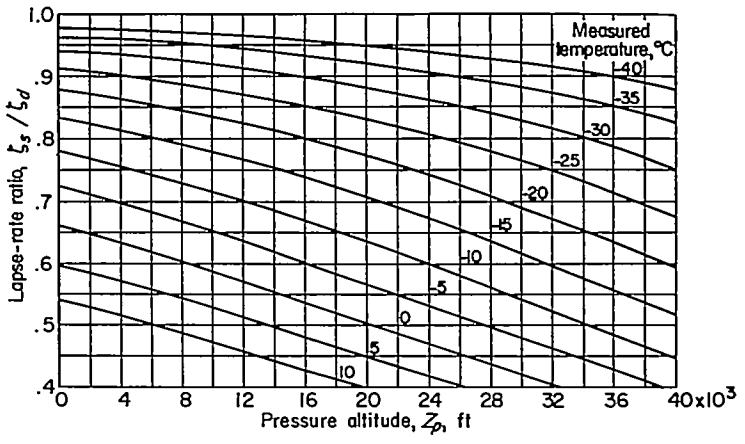

FIGURE 18.—Ratio of saturated- to dry-adiabatic lapse rate as function of temperature and pressure altitude.

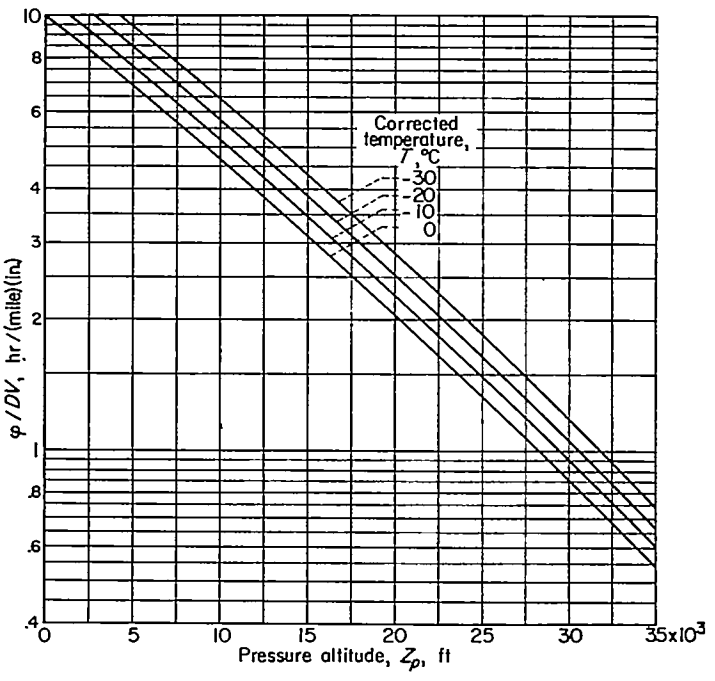

FIGURE 19.—Parameter φ/DV as function of temperature and pressure altitude.

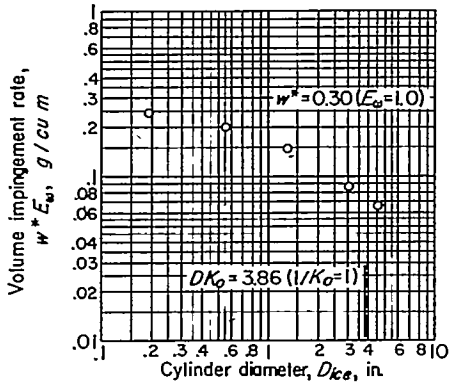

FIGURE 20.—Sample plot of volume impingement rate w^*E_ω as function of cylinder diameter.

(d) **Average cylinder diameter.**—The values of D_{ice} (item (14)) are calculated with the equation

$$D_{ice}=\frac{1}{2}\left(D+\sqrt{\frac{0.1509m^*}{\rho_{ice}l^*}+D^2}\right)$$

This equation defines D_{ice} as the average between the initial and final diameters of the iced cylinder.[2] The recommended average value of the ice density ρ_{ice} is 1.65 slugs per cubic foot; and, for the apparatus described herein, $l^*=2$ inches. Hence, the equation becomes

$$D_{ice}=\frac{1}{2}\left(D+\sqrt{0.0457m^*+D^2}\right)$$

(e) **Amount of ice per unit space.**—The mass of ice collected per unit space swept out by the cylinder is determined by the following equation:

$$w^*E_\omega=3467\frac{m^*}{D_{ice}l^*tV}$$

For the cylinders shown in figure 16, the length of the cylinders l^* is 2 inches, and the equation becomes

$$w^*E_\omega=1734\frac{m^*}{D_{ice}tV}$$

Values of w^*E_ω for each cylinder are entered as item (15).

(f) **Plotting.**—A plot of w^*E_ω as a function of D_{ice} is constructed on logarithmic graph paper. A sample plot is shown in figure 20. The plotted points are not connected, because the next step involves matching the plotted points to a curve.

(g) **Matching procedure.**—The liquid-water content, droplet size, and droplet-size distribution in the cloud are found by comparing the measured values of w^*E_ω, plotted as indicated in step (f), with calculated values for the cylinders in the same flight and atmospheric conditions. For matching with the flight data, sets of curves are required that represent the relation between the reciprocal of the inertia parameter $1/K_o$ and the over-all weighted collection efficiency E_ω for

[2] Experience on Mt. Washington has shown that more reliable results for the average diameter D_{ice} may be obtained from actual measurement of the final and initial diameters (ref. 25); however, this procedure is usually not practicable in flight. Moreover, the density of ice collected in flight is higher and more uniform than that of ice collected on Mt. Washington because of the higher airspeed in flight.

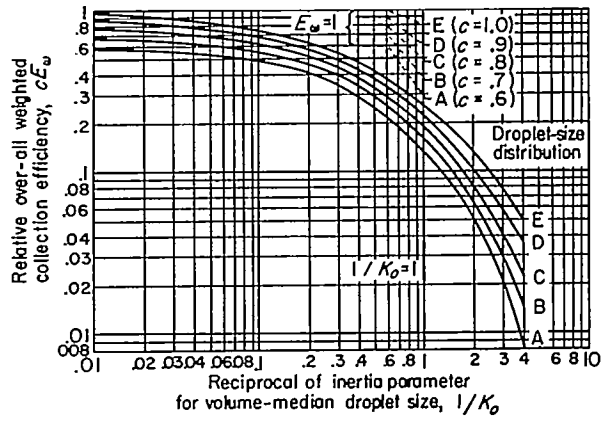

FIGURE 21.—Curves from data of table III showing relative over-all weighted collection efficiency as function of reciprocal of inertia parameter for $K_o\varphi=3000$ for droplet-size distributions defined in table II.

the five assumed droplet-size distributions for each of the five standard (arbitrarily selected) values of $K_o\varphi$ (0, 200, 1000, 3000, and 10,000). These curves (fig. 12) are prepared by plotting the data of table III on logarithmic graph paper of the same scale as that used for plotting the measured data (step (f)). In order that the values may be plotted as five curves for one value of $K_o\varphi$ on a single sheet of 2- by 3-cycle logarithmic graph paper without overlapping, values of E_ω for distributions A, B, C, D, and E (defined in table II) are multiplied by the constant factors 0.6, 0.7, 0.8, 0.9, and 1.0, respectively. The revised values of E_ω are given in table III, and a sample plot is shown in figure 21. Use of the curves is facilitated if the location of the line for which $1/K_o=1$ and each of the lines for which $E_\omega=1$ (corresponding to the five size distributions) are clearly marked. Figures 12, 20, and 21 are reprinted on page 43 for convenience in matching.

Matching the measured data with the theoretical calculations usually requires several steps of successive approximations in order to satisfy several restrictive conditions simultaneously. The principle underlying the stepwise procedure is discussed in section III. The stepwise procedure for matching the curves is as follows:

(1) A preliminary estimate of a value of $K_o\varphi$ from the standard values of $K_o\varphi$ given in table III is used for item (16)a on the work sheet. A value of 3000 is suggested unless experience dictates that other values are closer approximations. An incorrect preliminary estimate will not lead to an incorrect final result but will perhaps require extra successive approximations.

(2) The set of theoretical curves of E_ω as a function of $1/K_o$ applicable to the selected standard value of $K_o\varphi$ (item (16)a) is compared with the experimental plot prepared in step (f). The experimental plot is placed over the theoretical curves and viewed by transmitted light. The sheet containing the experimental points is moved about, with the two sets of axes kept parallel, until the position of best fit is obtained. The various curves for different droplet-size distributions are tried, and the one that most closely fits the experimental points is selected. The letter designating the curve of best fit is recorded as the droplet-size distribu-

tion (item (20)a). While the two plots are held in position of best fit, the value of D_{ice} that falls upon the line for which $1/K_o=1$ and the value of w^*E_ω that falls along the line for which $E_\omega=1$ are recorded as DK_o (item (17)a) and w^* (item (21)a), respectively.

(3) A corrected value of $K_o\varphi$ (item (18)a) is obtained by multiplying DK_o (item (17)a) times φ/DV (item (9)) times V (item (3)). The standard value of $K_o\varphi$ corresponding to item (18)a is selected from the following table and entered as item (16)b:

Range of estimated or calculated $K_o\varphi$	Corresponding standard value of $K_o\varphi$
200 to 440	200
441 to 1,750	1,000
1,751 to 5,600	3,000
5,601 to 30,000	10,000

If item (16)b is the same as item (16)a, items (17)a and (21)a are used in step (h). If item (16)b is different from item (16)a, the procedure of paragraph (2) of step (g) is repeated in the second approximation, and the curves applicable to the new standard value of $K_o\varphi$ (item (16)b) are used.

(h) **Droplet diameter and liquid-water content.**—The end results of step (g) are values of w^* (item (21)), DK_o (item (17)), droplet-size distribution (item (20)), and $K_o\varphi$ (item (18)), all of which were obtained with the curves based on the standard value of $K_o\varphi$ that corresponds to the actual value of $K_o\varphi$. These results are used to determine the droplet diameter and the liquid-water content as follows:

(1) The uncorrected droplet diameter (item (19)c) is obtained from figure 22 by using items (17), (3), and (7).

(2) The droplet-diameter correction factor (item (22)), obtained from figure 23 by using items (18) and (16), is multiplied by item (19)c to obtain the final value of droplet diameter d (item (23)). The droplet diameter obtained by

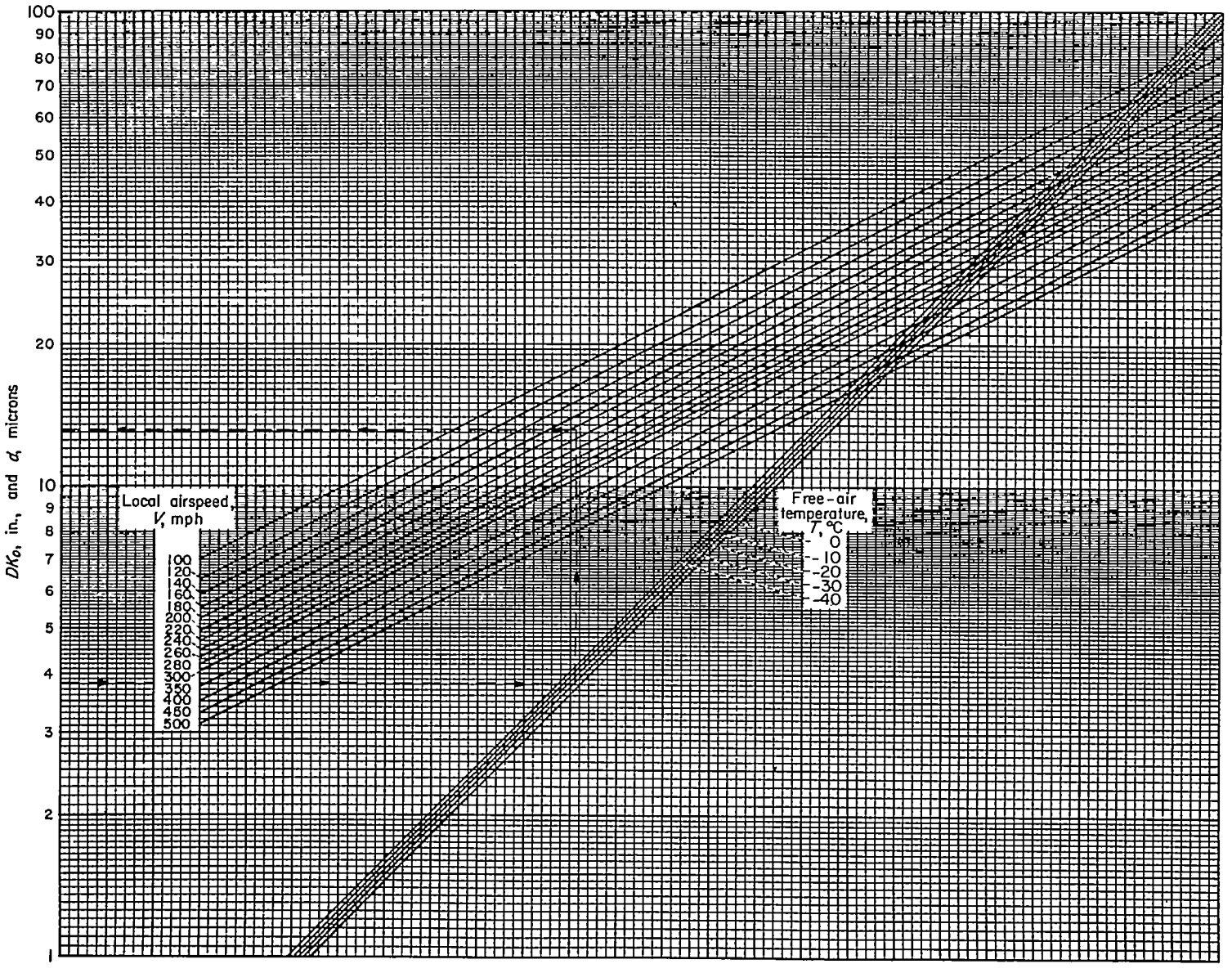

FIGURE 22.—Diagram for determining droplet diameter from DK_o, free-air temperature, and local airspeed. [Enter diagram with DK_o on ordinate, follow horizontal line to diagonal line representing temperature, follow vertical line to diagonal line representing airspeed, and follow horizontal line to value of droplet diameter on ordinate. Example: DK_o=3.86 in., T=−12.2° C, and V=191 mph; then d=13.3 microns.]

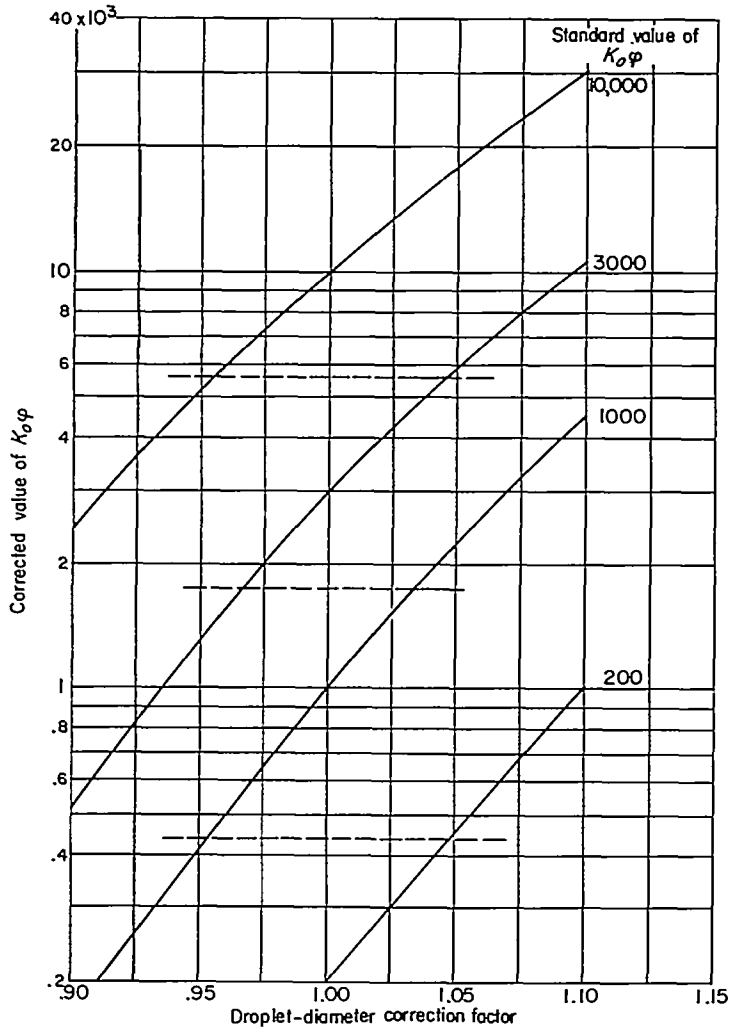

FIGURE 23.—Droplet-diameter correction factor.

this procedure is often referred to as the "mean effective droplet diameter." The dashed lines of figure 23 correspond to the values of the limits in the range of estimated or calculated $K_o\varphi$ given in the table in step (g).

(3) The liquid-water content in grams per cubic meter is obtained directly from item (21).

An alternate method for processing the data in steps (e) to (h) is presented in appendix E. The plotting and matching procedure of steps (f) and (g) are replaced by another graphical procedure that obviates making a series of approximations to the value of $K\varphi$.

V. EVALUATION OF ROTATING MULTICYLINDER METHOD

Errors in obtaining the flight data contribute to errors in the determination of liquid-water content and droplet sizes. Some of these errors result from errors in measuring flight speed, exposure time, and air temperature; from differences between the exposure time of the large cylinder and the small cylinder due to the time required to extend and retract the set; from losses in the accumulated ice while disassembling the cylinders before weighing; and from errors in weighing. Another error influencing the accuracy of the results is that expected in the calculation of the over-all weighted collection efficiency plotted in figure 12, which ranges from 1 to 2 percent (appendix D). Experience in obtaining flight data has shown that the aggregate error in w^*E_ω from all these sources can be kept below ± 10 percent but is seldom less than ± 5 percent.

The rotating multicylinder method also has several inherent undesirable characteristics that do not permit accurate results. Among these are the failure of droplets to freeze on the cylinders under certain conditions, the fact that the method does not measure the actual droplet-size distribution in the cloud but rather how closely the cloud corresponds to an assumed droplet-size distribution, and the insensitivity of the method in discriminating among different droplet-size distributions. These three undesirable characteristics are discussed in this section.

HEAT-BALANCE AND MASS-TRANSFER FACTORS IN FLIGHT MEASUREMENTS

One of the basic assumptions underlying the use of the multicylinder method is that all the droplets striking the cylinder freeze completely thereon. Investigators concerned with icing-cloud measurements have long been aware of the fact that this assumption is not fulfilled at temperatures only slightly below freezing (ref. 26). Under these conditions a considerable fraction of the impinging water may run off in the liquid state, making the results unreliable and difficult to interpret in terms of liquid-water content and droplet diameter. For this reason, flight measurements at temperatures above 26° F have usually not been attempted.

A quantitative analysis of the heat balance of a rotating cylinder in icing conditions is presented in reference 17. The results of this analysis indicate that the phenomenon of run-off imposes serious limitations on the range of liquid-water content that can be measured reliably by means of ice-collecting instruments, especially in the upper portion of the icing-temperature range. A later analysis in reference 18, which includes the effect of kinetic heating, indicates a further reduction in the range of reliable measurement at high airspeeds.

By means of the methods of calculation described in references 17 and 18, it is possible to determine the "critical" rate of ice formation such that the heat of fusion is just sufficient to bring the cylinder surface temperature to the melting point. If the rate of water impingement exceeds the critical rate of ice formation by more than the rate of evaporation, only a small fraction of the additional water freezes, the excess leaving the surface as run-off. The maximum observed rates of ice formation would therefore be expected to be at most only slightly greater than the calculated critical values. Moreover, because of the horizontal variations in liquid-water content in natural clouds, it can be shown (see appendix F) that the average rate of ice formation as measured by the multicylinder method is very unlikely to exceed the calculated critical value.

Comparison of the results of calculations following the method of reference 18 with multicylinder data obtained in

flight showed that the maximum measured rates of ice formation for individual cylinders exceeded the corresponding calculated critical values by as much as 50 to 70 percent. The explanation of this discrepancy is to be found in the fact that the calculations of reference 18 were based on values of the heat-transfer coefficient for smooth cylinders, whereas the actual surface of a cylinder exposed to heavy icing is rough and irregular. The increased heat transfer due to surface roughness causes an increase in the rate of removal of latent heat of fusion and thus accounts for the increased rate of ice accretion.

In order to define the reliable operating range of the multicylinders, critical rates of ice accretion were calculated for various flight conditions with the use of heat-transfer coefficients applicable to rough cylinders. An incidental result of the heat-balance calculations was the determination of evaporation rates, which provided a means of correcting multicylinder data for evaporation.

CRITICAL RATES OF FREEZING AND EVAPORATION

Since ice-collecting cylinders are used primarily for the measurement of liquid-water content, it is convenient to express both the rate of ice accretion and the rate of evaporation in terms of liquid-water content in the air stream in which the cylinders are exposed. If a cylinder of unit length and radius L is exposed in a stream of air having a velocity U and liquid-water content w, the total rate of water impingement is given by

$$W_m=2E_\omega LUw$$

The water impingement rate W_m is composed of three parts; the freezing rate W_f, the evaporation rate W_e, and the run-off rate W_r, as follows:

$$W_m=W_f+W_e+W_r \tag{20}$$

Similarly, the liquid-water content of the air stream may be regarded as being made up of three "partial" liquid-water contents w_f, w_e, and w_r, defined by the following equations:

$$\left.\begin{aligned} W_f&=2LU_lw_fE_\omega \\ W_e&=2LU_lw_eE_\omega \\ W_r&=2LU_lw_rE_\omega \end{aligned}\right\} \tag{21}$$

The quantities w_fE_ω, w_eE_ω, and w_rE_ω are called the "volume freezing rate," "volume evaporation rate," and "volume run-off rate," respectively. Each represents the amount of liquid water involved in a particular process per unit volume of air in the path of the cylinder (liquid water per unit space swept out by the cylinder). Their sum, the "volume impingement rate," is the product of the total liquid-water content and the over-all collection efficiency.

The critical volume freezing rate $(w_fE_\omega)_{cr}$ and the critical volume evaporation rate $(w_eE_\omega)_{cr}$ are the values of w_fE_ω and w_eE_ω that occur at the critical condition defined by

$$w_rE_\omega=0 \text{ and } T_S=0^\circ \text{ C} \tag{22}$$

Values of $(w_f{}^*E_\omega)_{cr}$ and $(w_e{}^*E_\omega)_{cr}$ were calculated by a method essentially similar to that used in reference 18, except that the cylinder surface was assumed to be rough instead of smooth and the local increase in airspeed due to the presence of the airplane was taken into account. The analysis, method of calculation, and assumptions necessary for solution of the problem are given in appendix F. Calculated values of the critical volume freezing rate and critical volume evaporation rate are presented in table IV for

TABLE IV.—CRITICAL VALUES OF $w_f{}^*E_\omega$ AND $w_e{}^*E_\omega$

[T_S=0° C; D=0.16 in.]

Pressure altitude, Z_p, ft	Local airspeed, V, mph	Temperature, °C							
		−5		−10		−15		−20	
		$w_f{}^*E_\omega$	$w_e{}^*E_\omega$	$w_f{}^*E_\omega$	$w_e{}^*E_\omega$	$w_f{}^*E_\omega$	$w_e{}^*E_\omega$	$w_f{}^*E_\omega$	$w_e{}^*E_\omega$
Sea level	100	0.96	0.048	2.04	0.083	3.23	0.107	4.55	0.126
	200	.57	.040	1.45	.069	2.41	.090	3.48	.105
	300	.17	.036	.93	.062	1.75	.081	2.66	.095
5,000	100	0.90	0.050	1.91	0.086	3.00	0.112	4.20	0.131
	200	.55	.042	1.37	.072	2.25	.094	3.23	.110
	300	.20	.038	.90	.065	1.65	.085	2.48	.099
10,000	100	0.86	0.053	1.79	0.091	2.79	0.118	3.89	0.138
	200	.54	.044	1.30	.076	2.11	.099	3.00	.116
	300	.22	.040	.88	.069	1.58	.089	2.33	.104
20,000	100	0.78	0.058	1.62	0.100	2.48	0.130	3.40	0.147
	200	.53	.049	1.20	.084	1.91	.110	2.65	.123
	300	.28	.044	.86	.076	1.47	.099	2.11	.111

various flight conditions for a cylinder 0.16 inch in diameter. This value was chosen because it is a representative average value of the outside diameter of the ice coating on a ⅛-inch cylinder during a typical exposure in icing conditions. The equations derived in appendix F for rough cylinders show that both $(w_e{}^*E_\omega)_{cr}$ and $(w_f{}^*E_\omega)_{cr}$ are proportional to the −0.253 power of the cylinder diameter. Values of $(w_e{}^*E_\omega)_{cr}$ and $(w_f{}^*E_\omega)_{cr}$ applicable to a cylinder of diameter D inches may therefore be found by multiplying the values in table IV by a factor G, given by

$$G=\left(\frac{0.16}{D}\right)^{0.253} \tag{23}$$

RELATION OF VOLUME RATES OF FREEZING, EVAPORATION, AND RUN-OFF

Various relations exist between wE_ω, w_eE_ω, w_fE_ω, and w_rE_ω, depending upon whether wE_ω is less than, equal to, or greater than the critical value. The following is a summary of such relations, derived in appendix F. In all three cases, it is presumed that ice is forming on the cylinder ($w_fE_\omega>0$).

Case I. Subcritical conditions:

$$wE_\omega<(wE_\omega)_{cr} \tag{24}$$

$$T_S<0^\circ \text{ C} \tag{25}$$

$$wE_\omega=w_eE_\omega+w_fE_\omega \tag{26}$$

$$w_rE_\omega=0 \tag{27}$$

Case II. Critical conditions:

$$wE_\omega=(wE_\omega)_{cr}=(w_cE_\omega)_{cr}+(w_fE_\omega)_{cr} \tag{28}$$

$$T_S=0^\circ\ \mathrm{C} \tag{29}$$

$$w_rE_\omega=(w_rE_\omega)_{cr}=0 \tag{30}$$

Case III. Supercritical conditions:

$$wE_\omega>(wE_\omega)_{cr} \tag{31}$$

$$T_S=0^\circ\ \mathrm{C} \tag{32}$$

$$w_eE_\omega=(w_eE_\omega)_{cr} \tag{33}$$

$$w_fE_\omega=(w_fE_\omega)_{cr}+\lambda[wE_\omega-(wE_\omega)_{cr}] \tag{34}$$

$$w_rE_\omega=(1-\lambda)[wE_\omega-(wE_\omega)_{cr}] \tag{35}$$

$$\lambda=\frac{h_{w,S}-h_{w,0}-\frac{1}{2}U^2}{h_{w,S}-h_{ice,S}} \tag{36}$$

CORRECTION OF MULTICYLINDER MEASUREMENTS FOR EVAPORATION (SUBCRITICAL CASE)

In the use of rotating cylinders for icing-cloud measurements, the volume freezing rate w_fE_ω is the quantity actually measured; whereas, the volume impingement rate wE_ω is required for use in the determination of liquid-water content and droplet size. Whenever $w_fE_\omega<(w_fE_\omega)_{cr}$ throughout the exposure interval (case I), equation (26) applies, and wE_ω can be determined from multicylinder measurements if w_eE_ω is a known function of w_fE_ω. In order to establish the relation between w_eE_ω and w_fE_ω for the subcritical case, values of both quantities were calculated for a 0.16-inch-diameter cylinder by the method described in appendix F for various values of T_S between T_0 and 0° C. It was found that $w_e{}^*E_\omega$ could be represented approximately by an equation of the form

$$w_e{}^*E_\omega=k+bw_f{}^*E_\omega \tag{37}$$

Values of the parameters k and b for various flight conditions are given in table V. This approximate equation yields values of $w_e{}^*E_\omega$ that agree with the individual calculated values to within ±0.01 gram per cubic meter for all flight conditions included in table V.

The analysis in appendix F shows that in the subcritical case the ratio of w_eE_ω to w_fE_ω is independent of cylinder diameter as long as the cylinder surface temperature is constant. A secondary effect exists, however, because the surface temperature varies slightly with cylinder diameter. This effect is of minor importance for two reasons: (1) The ratio w_eE_ω/w_fE_ω is relatively insensitive to differences in surface temperature except at low rates of ice formation; and (2) the variation of the heat-transfer coefficient with cylinder diameter is roughly similar to the corresponding variation of collection efficiency, and hence the variation of surface temperature with cylinder diameter is small. In the analysis of multicylinder icing data, it may be assumed, therefore, that the ratio of w_eE_ω to w_fE_ω is the same for each cylinder. Thus, the values of $w_f{}^*E_\omega$ determined from the weight of ice on each cylinder can be used as described in section IV to find $w_f{}^*$; and this result can be corrected for evaporation by means of the approximate equation

$$w^*=k+(1+b)w_f{}^* \tag{38}$$

where k and b have the values given in table V. Values of droplet diameter calculated from observed values of $w_f{}^*E_\omega$ do not require correction for evaporation, because the relative effect of evaporation is approximately the same for all cylinders.

TABLE V.—MULTICYLINDER EVAPORATION CORRECTIONS. VALUES OF CONSTANTS k AND b IN EQUATION (37)

Local airspeed, V, mph	Pressure altitude, Z_p, ft	Temperature, °C							
		−5		−10		−15		−20	
		k	b	k	b	k	b	k	b
100	0	0	0.051	[a]−0.002	0.040	[a]−0.004	0.032	[a]−0.006	0.026
	10,000	0	.062	−.002	.051	−.004	.012	−.006	.035
	20,000	0	.075	−.002	.063	−.004	.051	−.006	.013
200	0	0.006	0.061	0.003	0.045	0.001	0.035	−0.001	0.028
	10,000	.006	.071	.003	.055	.001	.044	−.001	.037
	20,000	.006	.082	.003	.067	.001	.055	−.001	.046
300	0	0.015	0.130	0.009	0.058	0.006	0.043	0.003	0.033
	10,000	.015	.110	.009	.068	.006	.052	.003	.042
	20,000	.015	.105	.009	.078	.006	.062	.003	.051

[a] Zero is to be used for w^* whenever the formula gives negative values.

INTERPRETATION OF MULTICYLINDER DATA WITH OCCURRENCE OF RUN-OFF

In the method described in section IV for determining liquid-water content and droplet size from multicylinder data, points representing the individual cylinders on a logarithmic plot of average volume ice-formation rate as a function of average cylinder diameter are fitted to an impingement curve representing the calculated relation between E_ω and $1/K_0$. On this same plot a line may be drawn to represent critical conditions as calculated for the observed temperature, airspeed, and altitude. This "critical line" has a constant slope of −0.253, as shown by equation (23). For observations in a continuous, uniform cloud, points representing cylinders at the critical condition lie along the critical line, points representing subcritical conditions lie below the critical line and along the impingement curve, and points representing supercritical conditions (run-off occurring) lie only slightly above the critical line, because the freezing fraction λ is generally small (see eq. (34)). For observations in discontinuous clouds, points representing critical or supercritical conditions lie approximately along a line called the "run-off line," which is located parallel to and generally below the critical line, because the effect on the average value of w_fE_ω of the term containing λ is nearly always smaller than the effect of discontinuities (gaps) in the cloud.

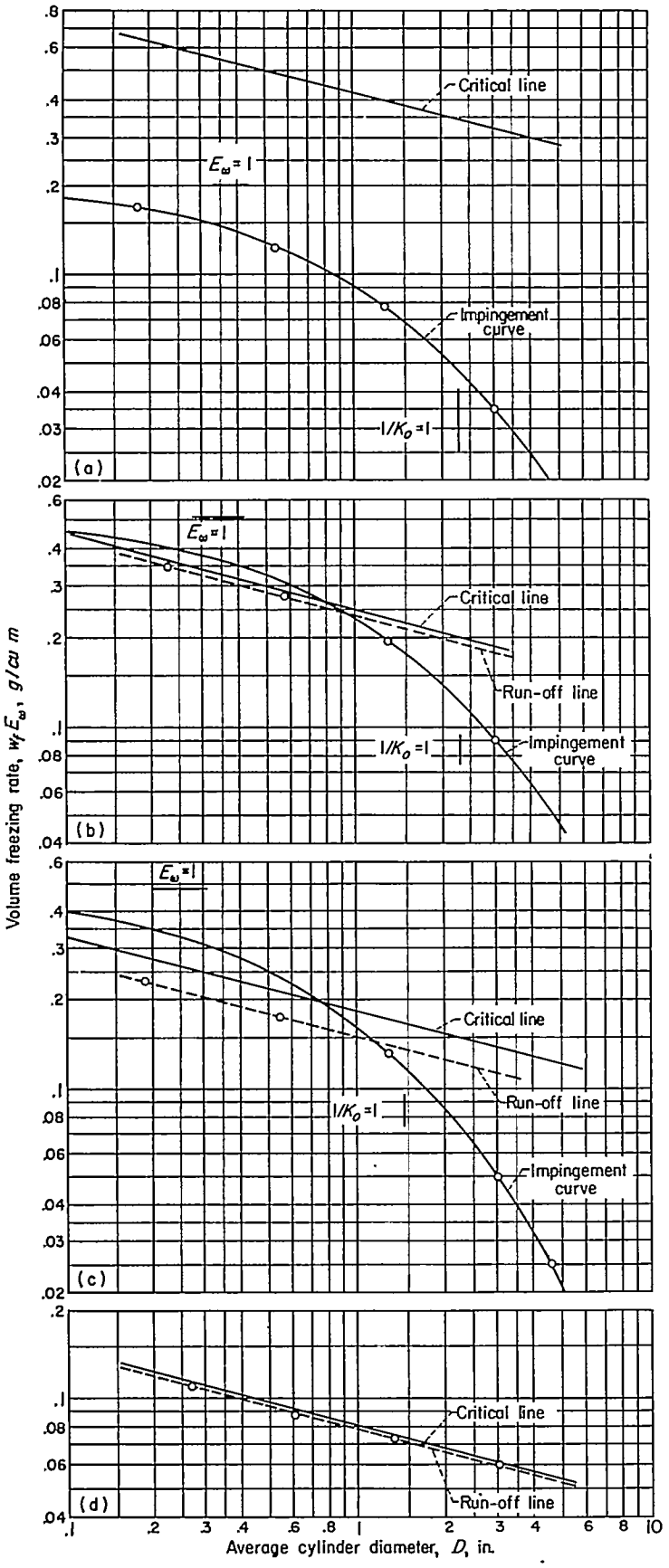

(a) No run-off from any cylinder [flight 20 (1/29/47, run 1), ref. 33].
(b) Run-off from two smallest cylinders, nearly continuous cloud [flight 10 (4/18/49, run 2), ref. 35].
(c) Run-off from two smallest cylinders, discontinuous cloud [flight 19 (2/9/50, run 2), ref. 35].
(d) Run-off from all four cylinders [flight 179 (3/29/48, run 17), ref. 36].

FIGURE 24.—Examples illustrating effect of run-off on multicylinder data.

Various relative locations of the critical line, run-off line, and impingement curve are possible, depending upon the flight conditions and the characteristics of the cloud. The representative points for each of the cylinders and the location of the critical line are calculated from the flight data. The run-off line is drawn to fit the data points representing cylinders apparently affected by run-off, and the impingement curve is fitted to the remaining points if possible.

Some of the possible configurations are illustrated in figure 24, which was prepared from NACA flight data. In the case in which no run-off occurs (all cylinders subcritical), all the representative points lie close to the impingement curve and below the critical line, as shown in figure 24 (a). In cases in which run-off occurs from some but not all of the cylinders, the run-off line intersects the impingement curve and some of the representative points lie on each curve as shown in figures 24 (b) and (c). The displacement of the run-off line below the critical line depends on the degree of discontinuousness of the cloud; and, since this factor cannot be evaluated from other flight data, the run-off line is drawn to fit the data points using the calculated slope of −0.253. The cloud represented by figure 24 (b) was almost continuous, as shown by the small displacement between the critical line and the run-off line; whereas, figure 24 (c) represents a less continuous cloud.

In cases such as those shown in figures 24 (b) and (c), in which less than four points are used to determine the impingement curve, the droplet-size distribution cannot be determined from the shape of the impingement curve; and the theoretical curves calculated for the C distribution are used arbitrarily, because the C distribution is believed to approximate the actual droplet-size distribution most likely to occur in natural clouds. In some cases (e. g., figs. 24 (b) and (c)), the manner of fitting the curves is rather simple and straightforward, and the average liquid-water content and droplet size may be determined with reasonable accuracy from the position of the impingement curve. In other cases, the interpretation of the data points is more difficult and the results are less reliable. A case in which run-off occurred from all four cylinders is shown in figure 24 (d). In this case, obviously, it is impossible to determine either the liquid-water content or the droplet size.

The use of a straight line of slope −0.253 as the run-off line implies that the average volume freezing rate for cylinders influenced by run-off is proportional to the critical volume freezing rate. This assumption is not exactly correct when applied to actual observations in clouds because

of the influence of two factors: (1) Because of the effect of horizontal variations in liquid-water content, a cylinder may experience both subcritical and supercritical conditions during a single exposure period; (2) under supercritical conditions, the second term in equation (34) varies with cylinder size in a different manner from the first. The net effect of these two factors is to increase slightly the slope of the run-off line and to introduce a slight convex curvature; however, the straight line with a slope of -0.253 is a close approximation.

If multicylinder data taken under conditions of partial run-off are analyzed by the ordinary method without reference to the possible occurrence of run-off, the results usually indicate values of liquid-water content that are too small and values of mean effective droplet diameter that are too large. This occurs because, under ordinary flight and cloud conditions, run-off occurs first from the smallest cylinders. For very large droplets, on the other hand, run-off occurs first from the largest cylinder and thus would tend to cause underestimation of the droplet size.

The methods described in the preceding paragraphs make possible the attainment of satisfactory results in many cases in which one or two cylinders are affected by run-off. Observations from which reliable results are unobtainable can also be recognized and rejected.

DROPLET-SIZE DISTRIBUTION

As mentioned previously, an important disadvantage of the multicylinder method is its failure to measure droplet-size distribution directly. The droplet-size distribution obtained is not necessarily the actual distribution existing in the cloud but rather an assumed distribution (table II). Although the actual droplet-size distribution in the cloud may affect the amount of ice collected on the cylinders in the manner described by the theoretical computations for an assumed droplet-size distribution, the area of coverage on an airfoil or on other nonrotating members in the clouds may differ from the area theoretically computed on the basis of the assumed distribution indicated by the rotating multicylinder method. The reason for the difference in area, or extent of coverage, is that the size of the largest droplets in the assumed distribution (given as a ratio to the volume-median size) is an arbitrarily assumed value, and the multicylinder method does not provide a means for obtaining the true value from the cloud data.

If the actual droplet-size distribution in a cloud is not of the same general form as the assumed distributions (e. g., if the distribution is bimodal), the effect of plotting the flight data (in the form of mass of ice collected as a function of cylinder size, fig. 20) would be that some of the points might appear as a scatter in the data caused by errors in measurement. This apparent scatter would influence greatly the values obtained for the mean effective droplet size (equivalent volume-median droplet size), as well as the type of distribution reported. The possible error in reported final results when apparent scatter in the flight data is present is discussed in the following section.

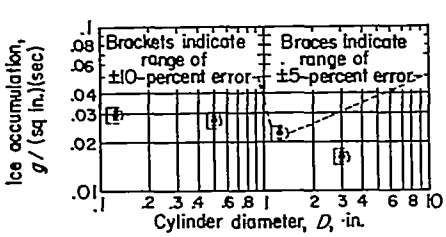

FIGURE 25.—Ice accumulation on set of cylinders. Local airspeed, 200 miles per hour; air viscosity, 3.436×10^{-7} slug per foot-second; pressure altitude, 10,000 feet.

EXPECTED ERRORS IN MATCHING FLIGHT DATA

A practical difficulty arises in matching the flight data with the calculated curves of figure 12. The difficulty is caused by the scattering of the measured data due to errors in measurements, by the difference between the assumed theoretical distributions on which the curves of figure 12 are based and the conditions actually prevailing in the natural cloud during the time the cylinders are exposed, and by the errors in the calculation of over-all weighted collection efficiency.

An attempt is made herein to evaluate the sensitivity of the multicylinder method when scatter of known magnitude is present in the flight data. The hypothetical data points of figure 25 were chosen to fit precisely the curve for the B distribution given in figure 12 (e) (volume-median droplet diameter for the data of fig. 25 was assumed to be 20 microns). If the data were taken in flight in a cloud in which the droplet sizes were defined by a B distribution and the volume-median droplet size were 20 microns, the data would probably not fit the B distribution of figure 12 (e) precisely, but each point would deviate by an amount depending on the accrued error related to the care in measuring. Furthermore, data will appear to have a scatter or error if the actual droplet-size distribution is not of the same general form as any of the assumed distributions. Incomplete freezing of droplets may also appear as part of the accrued error in the data, particularly if not properly accounted for (see previous section on HEAT-BALANCE AND MASS-TRANSFER FACTORS IN FLIGHT MEASUREMENTS).

The braces in figure 25 indicate the range of a ±5-percent error, and the brackets indicate the range of a ±10-percent error. The expected error in the calculation of over-all

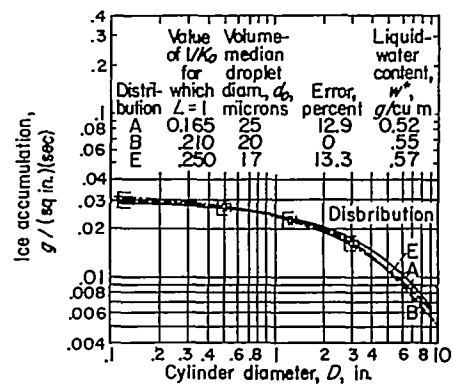

FIGURE 26.—Comparison of flight data with calculated impingement curves of figure 12 (e). $K_{\alpha\varphi}$, 10,000. (Braces indicate range of ±5-percent error; brackets indicate range of ±10-percent error.)

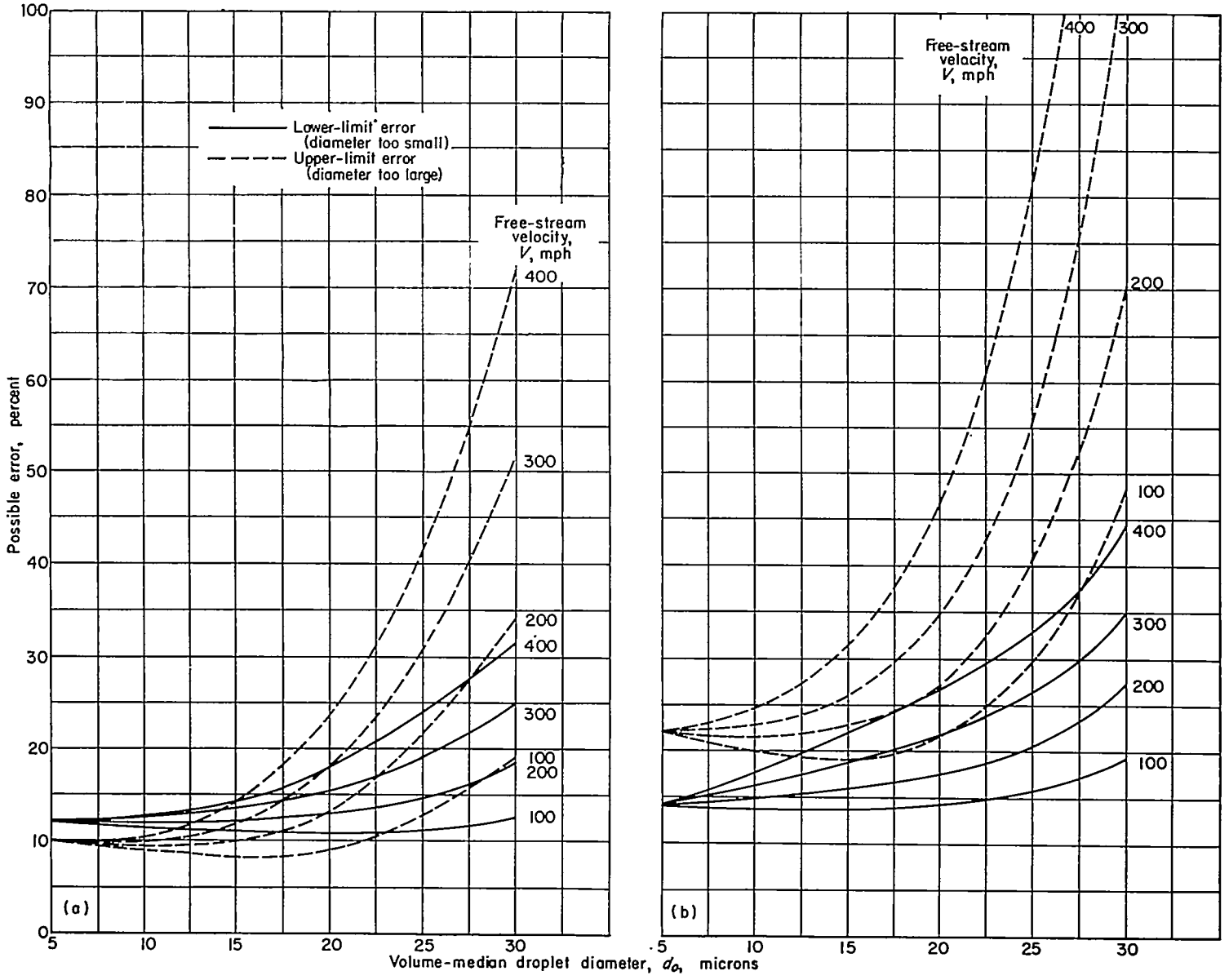

(a) Allowed error in measurement, ±5 percent.

(b) Allowed error in measurement, ±10 percent.

FIGURE 27.—Expected errors in determination of volume-median droplet size.

weighted collection efficiency plotted in figure 12 could be shown graphically in terms of the width of the lines used to plot the curves of figure 12. When the calculated curves of figure 12 are superposed on the flight data of figure 25 for comparison, the error in calculating over-all collection efficiency can be added to the error in measuring and both errors included in the range indicated by the braces (or brackets) and termed an accrued error. In the analysis of the flight data, the magnitude of the accrued error will affect the answers obtained and will determine the sensitivity of the multicylinder method.

Three sections of different curves taken from figure 12 (e) are shown in figure 26 to come within the ±5-percent range of accrued errors. The following is an illustrative example in the interpretation of the material presented in figure 26: If measurements were made simultaneously by a large number of careful observers who kept the accrued error within ±5 percent at a true airspeed of 200 miles per hour in a cloud in which the volume-median droplet size was actually 20 microns in diameter and the droplet-size distribution was most nearly defined by the B distribution of table II, the final answers reported by the observers would vary from 17 to 25 microns for the diameter of the volume-median droplet and from an A to an E distribution.

The type of analysis described with the use of figure 26 was made to cover a range of true flight speed up to 400 miles per hour and actual volume-median droplet sizes up to 30 microns in diameter. A set of four cylinders with diameters of 3, 1¼, ½, and ⅛ inches was assumed for the analysis. The other secondary variables assumed were an altitude of 10,000 feet and air viscosity of 3.436×10^{-7} slug per foot-second. The errors that can be expected in the final answers of the volume-median droplet size for the accrued errors of ±5 and ±10 percent (including the expected error in the calculations for the theoretical data of fig. 12) are shown in figures 27 (a) and (b), respectively. The ordinate is the error possible in reporting the actual volume-median droplet size in a cloud. Upper and lower limits are shown in the figures. Usually, it is possible to have a larger magnitude of error in reporting the size too large than in reporting the size too

small. For example, in a cloud in which the droplet size was actually 30 microns in diameter and the true airspeed was 200 miles per hour (accrued error=±5 percent, fig. 27 (a)), the answer reported would be within the limits of 25 and 40 microns. The lower-limit error is approximately 18 percent, and the upper-limit error is approximately 35 percent.

Doubling the sizes of the cylinders has the same effect on error as halving the flight speed. If a set of cylinders of 6-, 2¼-, 1-, and ¼-inch diameter are used at a flight speed of 200 miles per hour, the expected error can be found from the curves of figure 27 for a flight speed of 100 miles per hour. The expected error in the final results increases rapidly with increasing droplet sizes and flight speeds. The value of the multicylinder method in clouds consisting of volume-median droplet sizes above 30 microns in diameter is questionable, if the airplane speed cannot be maintained below 100 miles per hour.

The accuracy in the determination of the droplet-size distribution is very much subject to individual interpretation as well as to errors in measurement. The same measured data resolved by different observers often result in large differences in the typing of the distributions. If ±5-percent accrued error in measurements is assumed, the insensitivity of the multicylinder method does not permit an A distribution to be distinguished from an E distribution with data taken at flight speeds above 150 miles per hour.

Careful determinations of liquid-water content are usually not in error by more than ±5 percent, provided the size of the smallest cylinder is ⅛ inch in diameter or less and the measuring errors are less than ±4 percent (including errors due to incomplete freezing). The error in determining liquid-water content is usually 1 percent larger than the total errors in the measurements, because the curves of figure 12 are accurate only within ±1 percent at low values of $1/K_o$.

CONCLUDING REMARKS

Although the rotating multicylinder method for measurements in icing clouds has several inherent undesirable characteristics, it is considered to be the most reliable technique known at this time that is adaptable to flight use. The meteorological data obtained with the multicylinder method are the only data available for the design of ice-protection equipment for aircraft. An important deficiency of the method lies in its insensitivity in discriminating and resolving droplet-size distributions. The differences among the droplet-size distributions are masked by the scattering of the measured data due to errors in measurements, by differences between assumed theoretical conditions and those actually prevailing in the natural cloud, and by errors in the calculations.

Even though the effect of compressibility of the air on the droplet trajectories is negligible, the airplane speed should be maintained as low as possible in obtaining flight data, because the final results are most accurate at low speeds. Also, the limitations of ice-accretion rate caused by kinetic heating and heat of fusion are less severe at low airspeeds. Multicylinder results obtained with limitations on ice-accretion rates may be in error by a magnitude as large as the measurements, if the effect of run-off is not evaluated. Run-off is a factor in determining the volume-median droplet size and the liquid-water content. If run-off is not recognized in the analysis of the data, the measured data points are incorrectly matched to the theoretically calculated matching curves.

Different forms of the multicylinder instruments are discussed in reference 25, along with the effects of yaw, ice density, and other factors on the reliability of data and the reproducibility of measurements for conditions on a mountain.

Lewis Flight Propulsion Laboratory
National Advisory Committee for Aeronautics
Cleveland, Ohio, *September 5, 1952*

APPENDIX A

SYMBOLS

The following symbols are used in this report:

a droplet radius, ft (3.048×10^5 microns)
C_D drag coefficient for droplets in air
c constant
c_p specific heat of air at constant pressure, ft-lb/(slug)(°C)
D cylinder diameter, in.
d droplet diameter, microns (3.28×10^{-6} ft)
E collection efficiency based on cylinder radius, dimensionless
F drag force, lb
G factor to correct $(w_f E_\omega)_{cr}$ for cylinder diameter
H convective heat-transfer coefficient, ft-lb/(sec)(sq ft)(°C)
h specific enthalpy of water at state and temperature indicated by subscript, ft-lb/slug
I amount of ice collected per unit frontal area, slugs/sq ft
I^* amount of ice collected per unit frontal area, (mph)(sec)(g/cu m)
K inertia parameter, $\frac{2}{9}\frac{\rho_w a^2 U}{\mu L}$, dimensionless
k,b arbitrary evaporation parameters evaluated in table V
L cylinder radius, ft
l length of cylinder, ft
l^* length of cylinder, in.
M Mach number
m mass of ice collected on cylinder, slugs
m^* mass of ice collected on cylinder, g
Nu Nusselt number, $2LH/\kappa$
p pressure, in. Hg
q quantity of heat per unit time per unit cylinder length, ft-lb/(sec)(ft)
Re local Reynolds number with respect to droplet size, $2a\rho_a\bar{v}/\mu$
Re_C local Reynolds number with respect to cylinder size, $2L\rho_a U_l/\mu$
Re_0 free-stream Reynolds number with respect to droplet size, $2a\rho_a U/\mu$

r radial distance from cylinder axis to point in flow field, ratio to cylinder radius
T temperature, °C
T^* temperature, °R
t time, sec
U free-stream velocity, ft/sec
U_l air velocity, local at cylinder exposure point, ft/sec
u local air velocity, ratio of actual air velocity to free-stream velocity
V average corrected local airspeed, mph
v local droplet velocity, ratio of actual droplet velocity to free-stream velocity
$\bar{v}$ local vector difference between velocity of droplet and velocity of air, ft/sec
W rate of water collection per unit span of cylinder, slugs/(sec)(ft span)
W_β local rate of water impingement, slugs/(sec)(sq ft)
w liquid-water content in atmosphere, slugs/cu ft
w^* liquid-water content, g/cu m
x,y rectangular coordinates, ratio of actual distance to cylinder radius L
Z_p pressure altitude, ft
α angle between x-axis and radial line to point in flow field, deg
β local impingement efficiency, $dy_0/d\theta$, dimensionless
Γ average true airspeed, mph
γ ratio of specific heats
ϵ ratio of density of water vapor to density of dry air, 0.622
ζ_d dry-adiabatic lapse rate, °C/m
ζ_s saturated-adiabatic lapse rate, °C/m
θ impingement angle on cylinder, deg or radians as noted
κ thermal conductivity of air, ft-lb/(sec)(sq ft)(°C/ft)
λ freezing fraction, dimensionless
μ viscosity of air, slugs/(ft)(sec)
ρ density, slugs/cu ft
σ temperature-recovery factor, dimensionless
τ time scale, tU/L
φ $\frac{Re_0^2}{K}\equiv\frac{18\rho_a^2LU}{\mu\rho_w}$, dimensionless

Subscripts:
a air
c compressible
cr critical
d dry
e evaporation
f freezing
i incompressible
ice ice
l local at cylinder exposure point
m maximum
o volume median
r run-off
S surface
s saturated
v water vapor
w liquid water
x horizontal
y vertical
ω weighted
0 free stream

Superscript:
$'$ applied where velocity terms are in ft/sec

APPENDIX B

STARTING CONDITIONS OF TRAJECTORIES AT LARGE VALUES OF $-x$

For practical reasons the integration of the differential equations of motion (eqs. (1) and (2)) cannot be started with the NACA analog from an infinite distance ahead of the cylinder. The equations are therefore linearized by an approximation up to a convenient distance ahead of the cylinder. The method of linearizing the equations, which is presented in reference 3, results in the following expressions (in the nomenclature of ref. 3):

$$v_x=1-\frac{M(\beta)}{x^2}$$

$$v_y=\frac{1-M(\beta)y_0}{Kx^2}-\left(\frac{2y_0}{x^5}\right)(1-2y_0)^2$$

$$\Delta y=\frac{M(\beta)y_0}{x^2}+\frac{(1-y_0)^2y_0}{x^4}$$

$$M(\beta)=\beta+\beta^2e^\beta E_i(-\beta)$$

$$\beta=-\frac{x}{K}$$

The exponential integral $E_i(-\beta)$ is tabulated in pages 1 to 9 of reference 27. The y ordinate of the droplet is found by adding Δy to y_0.

For the studies of the trajectories discussed herein, the integration of equations (1) and (2) with the NACA analog was always started at $x=-5$. The accuracy of the preceding linearized starting equations was checked by integrating equations (1) and (2) for $K=32$, 16, and 4 with the NACA analog from $x=-50$ to $x=-5$. The difference in results was within the expected accuracy of the analog. The preceding linearized starting equations were found to be invalid for values of K less than 0.5. For values of K less than 0.5, the equations gave values of v_y greater than the corresponding values of u_y, and values of v_x smaller than the corresponding values of u_x. For values of K less than 0.5, the starting conditions at $x=-5$ were assumed to be the same as those conditions prevailing for the air streamlines. This assumption is valid, because the droplet inertias are very small.

APPENDIX C

CONVERSION OF PRACTICAL FLIGHT UNITS INTO DIMENSIONLESS PARAMETERS

The following relations are presented to aid in the interpretation of free-stream velocity (airplane speed), cylinder diameter, air viscosity, air and water density, and droplet diameter in terms of the dimensionless parameters K, φ, and Re_0 used in this report:

$$K=4.088\times10^{-11}\left(\frac{d^2U}{\mu D}\right) \tag{C1}$$

$$Re_0=4.813\times10^{-6}\left(\frac{d\rho_a U}{\mu}\right) \tag{C2}$$

$$d=1.564\times10^{5}\sqrt{\frac{K\mu D}{U}} \tag{C3}$$

$$\varphi=0.567\,\frac{\rho_a^2 DU}{\mu} \tag{C4}$$

$$K\varphi=2.316\times10^{-11}\left(\frac{d\rho_a U}{\mu}\right)^2 \tag{C5}$$

$$\rho_a=0.0412\,\frac{p}{T^*} \tag{C6}$$

$$W_m=2.745\times10^{-2}EDUw^* \tag{C7}$$

$$W_\beta=0.329Uw^*\beta \tag{C8}$$

where the specific weight of water was assumed to be 62.46 pounds per cubic foot, and the acceleration due to gravity, 32.17 feet per second per second.

APPENDIX D

METHOD OF CALCULATING CURVES OF $1/K_o$ AGAINST E_ω FOR DIFFERENT ASSUMED DROPLET-SIZE DISTRIBUTIONS

The procedure for obtaining the over-all weighted collection efficiency (fig. 12) is explained with the use of a sample calculation for the B distribution of table II and an assumed $K_o\varphi$ of 200 (eq. (17)). The over-all weighted collection efficiency of one cylinder in a group of cylinders is given as the final result in table VI. As a basis for beginning the computation, a value of $1/K=4.0$ is assigned to those droplets in the volume-median group size. (This particular value of $1/K$ is chosen arbitrarily and will define one point on the curves of $1/K_o$ against E_ω for $K_o\varphi=200$ of fig. 12 (b).) A value of the collection efficiency for $K=1/4.0$ is found in figure 4 and is given in the fifth column of table VI. The required value of φ is obtained from the original assumption that $K_o\varphi=200$; therefore, $\varphi=800$ for $1/K_o=4.0$. The weighted collection efficiency is found by taking the product of the percentage water in each size group (column 3) and the collection efficiency of column 5. The weighted collection efficiency is recorded in column 6. The effect of the variation of the group size on $1/K$ is obtained by dividing the value of $1/K$ assigned to the volume-median droplet size ($1/K=4.0$ in this example) by $(a/a_o)^2$, because the droplet radius appears to the second power in equation (3). The change in K with the change in droplet size is recorded in column 4. A value for the collection efficiency is found from figure 4 for each value of K in column 4. The value of φ remains the same as for the volume-median droplet size (800), because the droplet size does not enter into the definition of φ (eq. (7)).

TABLE VI.—SAMPLE CALCULATIONS OF E_ω FOR DISTRIBUTION B AND $K_o\varphi=200$

Group	a/a_o	Percent water in each size group	K	E	Weighted collection efficiency
(a) $1/K_o=4.0$ for volume-median droplet size; $\varphi=800$					
1	0.56	5	0.079	-----	------
2	.72	10	.130	-----	------
3	.84	20	.177	0.003	0.0006
4	1.00	30	.250	.027	.0081
5	1.17	20	.343	.065	.0130
6	1.32	10	.435	.100	.0100
7	1.49	5	.555	.140	.0070
Over-all weighted collection efficiency, E_ω					0.0387
(b) $1/K_o=1.0$ for volume-median droplet size; $\varphi=200$					
1	0.56	5	0.314	0.068	0.0034
2	.72	10	.518	.158	.0158
3	.84	20	.706	.225	.0450
4	1.00	30	1.000	.301	.0903
5	1.17	20	1.370	.384	.0768
6	1.32	10	1.740	.444	.0444
7	1.49	5	2.220	.515	.0258
Over-all weighted collection efficiency, E_ω					0.3015

The weighted collection efficiency is again the product of the values in column 3 and the collection efficiency of column 5. The sum of the individual weighted collection efficiencies of column 6 is the over-all weighted collection efficiency. The sum of column 6 in table VI(a), in combination with the assigned value of $1/K_o$ to the volume-median droplet size, defines one point on the B-distribution curve of figure 12 (b).

In order to obtain another point for the B-distribution curve of figure 12 (b), a different value is assigned to $1/K$ for the volume-median droplet size; for example, in table VI(b), $1/K_o=1.0$. Lowering the value of $1/K_o$ has the same effect as decreasing the cylinder size L when the physical dimensions of the volume-median droplet size, airplane speed, water density, and air viscosity are maintained constant (eq. (3)), as is actually the physical condition when a set of different-sized cylinders are flown simultaneously through a cloud. The procedure for computing the values in columns 4, 5, and 6 is the same as was described for table VI(a). The only exception is that the value of φ is now changed to 200 in order to maintain $K_o\varphi=200$ for $1/K_o=1.0$. The value of φ is maintained at 200 for the calculations in table VI(b).

The calculations of reference 3 are different from those described herein, in that, in the calculations of reference 3, φ was apparently allowed to vary to conform with maintaining $K\varphi$ constant during the calculations for the weighted collection efficiency. The value of φ cannot be permitted to vary during the calculations of the over-all weighted collection efficiency, because airplane speed, cylinder size, air density, air viscosity, and water density are not variables during that phase of the calculations.

The over-all weighted collection efficiencies, which are the sums of column 6 in table VI, are tabulated in table III for the values required to draw the curves of figure 12. The values of table III are subject to a tolerance error caused by the limit of accuracy in obtaining the collection efficiencies from the trajectories computed with the analog. The expected error in determining the collection efficiency for droplets with low inertia was much greater than for those with large inertia. The expected root-mean-square error of the over-all weighted collection efficiencies of table III, based on the expectation of individual random errors, was determined from the following expression:

$$\Delta H=\sqrt{(0.05)^2(\Delta a)^2+(0.10)^2(\Delta b)^2+(0.20)^2(\Delta c)^2+(0.30)^2(\Delta d)^2+(0.20)^2(\Delta e)^2+(0.10)^2(\Delta f)^2+(0.05)^2(\Delta g)^2}$$

where Δa, Δb, and so forth are actual errors in determining the respective collection efficiencies. The expected root-mean-square error in the curves of figure 12 has been determined to be somewhat less than 1 percent for values of E_ω near 1.0 and approximately 2 percent for values of E_ω near 0.01.

APPENDIX E

ALTERNATE METHOD OF REDUCING ROTATING MULTICYLINDER DATA

By Paul T. Hacker

INTRODUCTION

The method presented in this appendix for the processing of the flight data to obtain liquid-water content, droplet size, and droplet-size distribution is identical with the method presented in section IV of the body of the report up to step (e) of the STEPWISE CALCULATING PROCEDURE. The plotting and matching procedure of steps (f) and (g) are replaced by another graphical procedure that obviates the need for a series of successive approximations to the value of $K\varphi$. (Symbols are defined in appendix A.) This method directly yields two quantities: $K\varphi$, from which the droplet size is computed; and $1/Utw$, which is inversely proportional to the liquid-water content. Theoretically, approximate droplet-size distribution patterns can also be obtained by this method by using the calculated impingement data for various assumed droplet distribution patterns presented in table II. The theory of the method is presented, and a stepwise calculating procedure is outlined. The stepwise procedure is illustrated with the same example used for the method presented in section IV.

THEORY

BASIC CONCEPTS, ASSUMPTIONS, AND DIMENSIONLESS PARAMETERS

The basic concepts, assumptions, and dimensionless parameters for this method are identical with those used for the standard method. The mass of ice collected per unit frontal area on a rotating cylinder exposed in a supercooled cloud is given by

$$I=\frac{m}{2Ll}=EUwt \tag{E1}$$

where L is the average radius of the iced cylinder and E is the collection efficiency corresponding to this radius. For clouds composed of droplets of uniform size, the theoretical collection efficiency E is given in figure 4 in terms of two dimensionless parameters K and φ (eqs. (3) and (7)).

As is discussed in section III on the BASIC CONCEPT, the mathematical condition that $K\varphi$ is a constant corresponds to the physical situation existing during the exposure of a multicylinder set in flight, and the only unknown quantity is the droplet radius a for any given exposure. Since $K\varphi$ is constant for all cylinders for a given exposure, it is convenient to express the theoretical collection-efficiency data of table III in terms of $K_o\varphi$ and φ. Figure 28 (a) is a plot of the collection efficiency E_ω as a function of φ for various values of $K_o\varphi$ for droplets of uniform size (distribution A). This plot is the working chart for this method of determining droplet size and liquid-water content.

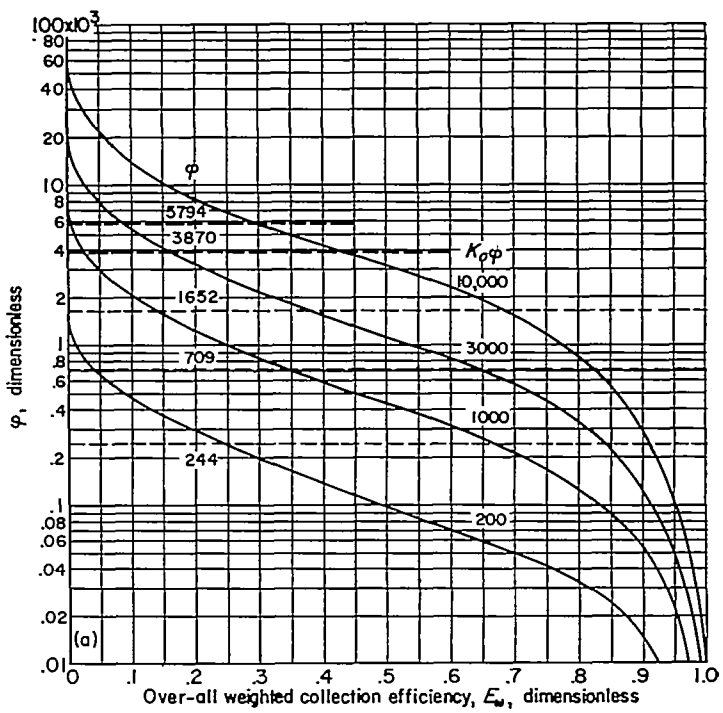

(a) Distribution A.

FIGURE 28.—Over-all weighted collection efficiency as function of φ for four values of $K_o\varphi$.

DETERMINATION OF LIQUID-WATER CONTENT AND DROPLET SIZE

For droplets of uniform size it is theoretically possible to determine by this method the droplet size and liquid-water content from the amount of ice collected on two cylinders of different diameter. For practical purposes, however, several cylinders should be employed in order to eliminate errors in droplet size and liquid-water content due to errors in the measured amount of ice collected on a cylinder. Only two cylinders will be used, however, to develop the theory of the method.

Assume that two cylinders with initial radii of $L_{0,1}$ and $L_{0,2}$ are exposed for a period of time t and collect amounts of ice m_1 and m_2, respectively. Average radii (L_1 and L_2) may be calculated for the two cylinders by the equation

$$L=\frac{1}{2}\left(L_0+\sqrt{\frac{m}{\rho_{ice}\pi l}+L_0^2}\right) \tag{E2}$$

from which two values of φ (φ_1 and φ_2) may be calculated by equation (7) and other flight data. Substitution of values of mass of ice collected m and average cylinder radius L into equation (E1) gives

$$I_1=\frac{m_1}{2L_1 l}=E_1 Uwt \tag{E3}$$

and

$$I_2=\frac{m_2}{2L_2 l}=E_2 Uwt \tag{E4}$$

where E_1, E_2, and w are unknown quantities; but w, the liquid-water content, is the same for the two cylinders. Since L is the only factor that changes the value of φ for any given exposure, equation (E3) is for $\varphi=\varphi_1$ and equation (E4) is for $\varphi=\varphi_2$. Solving the two equations for $1/Uwt$ gives

$$\frac{1}{Uwt}=\frac{E_1}{I_1} \tag{E5}$$

and

$$\frac{1}{Uwt}=\frac{E_2}{I_2} \tag{E6}$$

The right sides of the two expressions may be set equal to each other because Uwt is identical for both. The result is

$$\frac{E_1}{I_1}=\frac{E_2}{I_2} \tag{E7}$$

where $\varphi=\varphi_1$ for the left side and $\varphi=\varphi_2$ for the right side. Equation (E7) states that the ratio of collection efficiency to the mass of ice collected per unit frontal area is the same for all cylinders for a given exposure. Equation (E7) is the fundamental relation upon which this method is based.

From figure 28 (a) it is possible to determine a value of $K\varphi$ which is constant for a given exposure of cylinders so that the ratio of the collecton efficiency to the mass of ice collected per unit frontal area is the same for all values of φ (in this case φ_1 and φ_2). This determination is accomplished in the following manner: For a constant value of φ, say φ_1, the theoretical values of E are tabulated from figure 28 (a) for various values of $K\varphi$. The values of E are then divided by the mass per unit frontal area of the cylinder I_1, and a plot of $K\varphi$ as a function of E/I_1 is made. The

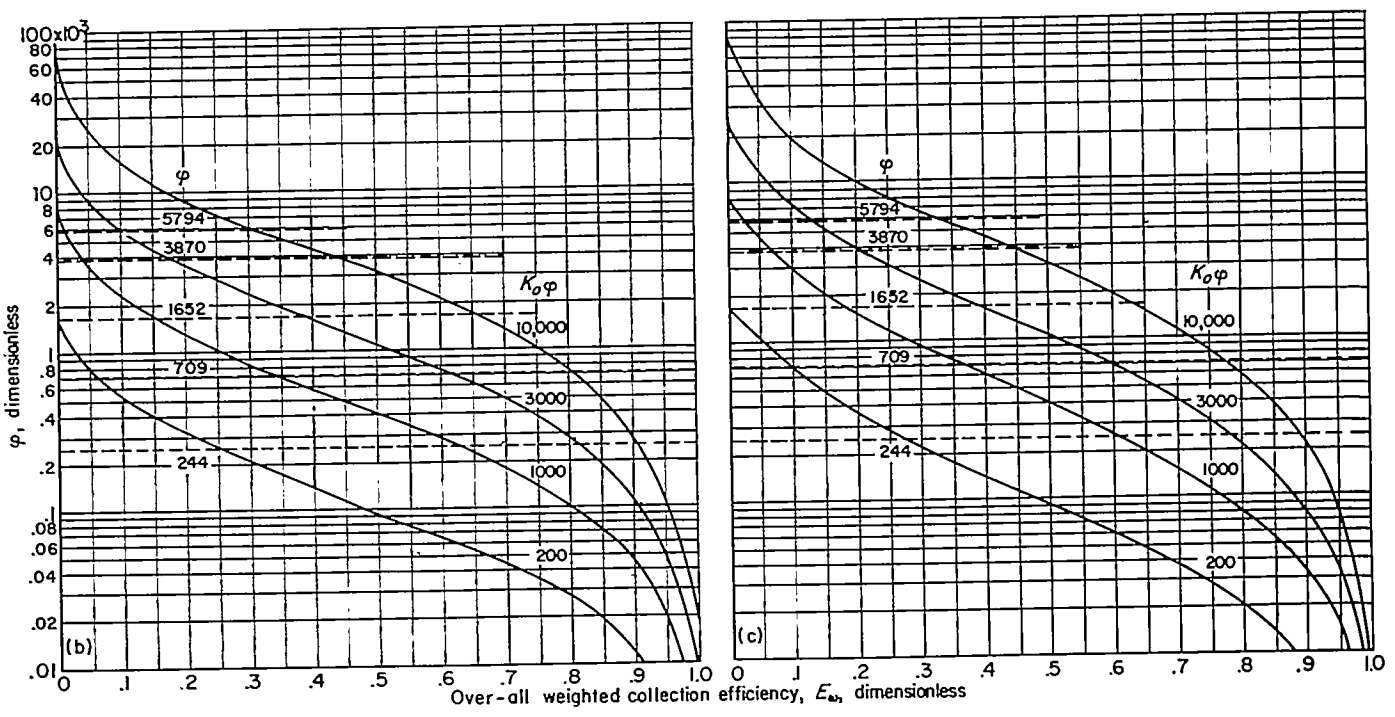

(b) Distribution C.

(c) Distribution E.

FIGURE 28.—Concluded. Over-all weighted collection efficiency as function of φ for four values of $K_0\varphi$.

same procedure is used for φ_2, and the results are plotted on the same chart as those for φ_1. Curves are faired through the two sets of points, and the point of intersection of the two curves determines the value of $K\varphi$ for which equation (E7) is satisfied. From this value of $K\varphi$ the droplet size can be calculated by use of equation (17). The intersection point also determines a value of E/I from which the liquid-water content w can be determined by equations (E5) or (E6), since U and t are known.

When three or more cylinders are employed, all the curves of $K\varphi$ against E/I should intersect in a point. If there are errors in the amounts of ice collected on individual cylinders or the cloud is not composed of droplets of uniform size, then the curves will not intersect in a point.

APPLICATION OF METHOD TO CLOUDS OF NONUNIFORM DROPLET SIZE

Theoretically, this method may be used to determine approximate droplet-size distribution patterns if working charts (fig. 28 (a)) are made for the various assumed droplet distributions presented in table II. Working charts for distribution C and E are shown in figures 28 (b) and (c), respectively. Three or more cylinders are required to determine the droplet-size distribution. The experimental data are processed for all assumed droplet-size distributions, and the one that most nearly gives a single intersection point for the curves of $K\varphi$ against E/I is the approximate droplet-size distribution. As was discussed in section III, the droplet size is the volume-median droplet size, the collection efficiency is the weighted collection efficiency E_ω, and K in $K\varphi$ is replaced by K_o for the volume-median droplet size.

UNITS FOR EQUATIONS

The preceding equations are true for any consistent system of units. For practical reasons, certain departures from consistent units are desirable for routine use. Thus, in the detailed calculation procedure described in the following section, mixed units are employed with numerical conversion factors.

STEPWISE CALCULATING PROCEDURE

Steps (a) to (d).—Steps (a) to (d) in the calculation procedure for this method are identical with those in section IV, and items (1) to (14) in work sheet II are the same as those in work sheet I. Work sheet II is presented for this alternate method with an actual observation as an example.

(e) Relative amount of ice per unit frontal area.—The mass of ice collected per unit frontal area is determined by the following equation:

$$I^*=3.467\times10^3\left(\frac{m^*}{D_{ice}l^*}\right)$$

For the cylinders shown in figure 16, the length of the cylinders l^* is 2 inches, and the equation becomes

$$I^*=1.734\times10^3\left(\frac{m^*}{D_{ice}}\right)$$

where D_{ice} is obtained from item (14). Values of I^* for each cylinder are entered as item (15).

(f) Parameter φ for average diameters of cylinders.—The parameter φ is calculated for each cylinder by use of the average diameter D_{ice} (item (14)), V (item (3)), and φ/DV (item (9)). The values of φ for the example are 244, 709, 1652, 3870, and 5794 for the five cylinders. These values are entered as item (16) in work sheet II and are indicated by dashed lines in figure 28.

(g) Tabulation of E_ω as function of $K_o\varphi$ for values of φ.—Tabulated values of E_ω (E_ω is identical to E for distribution A) as a function of $K_o\varphi$ for the values of φ computed in step (f) are obtained from figure 28 by reading the value of E_ω for the intersection points of a constant φ line with the $K_o\varphi$ curves. For example, for $\varphi=244$ (fig. 28 (a)), the values of E_ω for $K_o\varphi$ equal to 200, 1000, 3000, and 10,000 are 0.242, 0.668, 0.840, and 0.912, respectively. If the droplet-size distribution is to be determined, it is necessary to tabulate E_ω as a function of $K_o\varphi$ with φ constant for all the assumed droplet-size distributions. The values of $K_o\varphi$ and E_ω thus obtained are entered in item (17) of work sheet II for the appropriate cylinder size and droplet-size distribution.

(h) Parameter E_ω/I^*.—The values of E_ω for the various cylinders entered in item (17) are divided by the corresponding value of I^* (item (15)), and the results are entered in the columns of item (17) for E_ω/I^*.

(i) Plotting $K_o\varphi$ as function of E_ω/I^*.—For a given assumed droplet-size distribution, the values of $K_o\varphi$ in item (17) are plotted as a function of the values of E_ω/I^* (item (17)) for all cylinders on a single sheet of semilog paper. Curves are faired through the plotted points as shown in figure 29. The curves should intersect in a point, if the correct droplet-size distribution has been assumed and there are no errors in the amount of ice collected on an individual cylinder. If the curves do not intersect in a single point for any droplet-size distribution, the midpoint of the smallest polygon formed by the intersecting curves is used to determine $K_o\varphi$ and E_ω/I^*. An inspection of figure 29 reveals that, for the example, the curves for distribution E (fig. 29 (c)) most nearly intersect in a point. This droplet-size distribution is entered as item (18) of the work sheet. At the intersection point the values of $K_o\varphi$ and E_ω/I^* are read and entered as items (19) and (20). These values are 5400 and 8.46×10^{-5}, respectively.

(j) Droplet size.—The droplet size d is determined from the value of $K_o\varphi$ (item (19)) and the following equation:

$$d=\frac{\mu\sqrt{K_o\varphi}}{4.8\times10^{-6}(\rho_a V)}$$

which is derived from the definition of $K\varphi$ given as equation (17). Values of viscosity μ and air density ρ_a corresponding to the corrected air temperature T (item (7)) and the pressure altitude Z_p (item (4)), respectively, may be found in many references. Another method for finding the droplet size is to convert $K_o\varphi$ into LK_o by items (14) and (16) and use the graphical method presented in figure 22. For the example, the droplet size is 14.1 microns and is entered as item (21).

WORK SHEET II FOR ALTERNATE METHOD WITH AN OBSERVATION AS AN EXAMPLE

(1) Average indicated airspeed, mph	171
(2) Average true airspeed, Γ, mph	185
(3) Average local airspeed, V, mph	191
(4) Pressure altitude, Z_p, ft	7000
(5) Uncorrected air temperature, °C	−10.1
(6) Wet-air temperature correction, °C	−2.1
(7) Corrected temperature, T, °C	−12.2
(8) Exposure period, t, sec	216
(9) φ/DV, hr/(mile)(in.)	6.7

	Cylinder diameter, D, in.				
	⅛	½	1¼	3	4½
(10) Gross weight, g	7.44	23.56	59.68	141.83	190.47
(11) Tare weight, g	6.34	20.94	55.16	135.61	183.41
(12) Net weight of ice, g	1.10	2.62	4.52	6.22	7.06
(13) Corrected net weight, m^*, g	1.10	2.62	4.52	6.22	7.06
(14) D_{ice}, in.	.191	.554	1.291	3.024	4.518
(15) I^*, (mph)(sec)(g/cu m)	9981	8196	6068	3564	2702

(17)	Initial cylinder diameter, D, in.									
	⅛		½		1¼		3		4½	
	(16) φ for average diameters of iced cylinder, D_{ice}									
$K_o\varphi$	244		709		1652		3870		5794	
	E_ω	E_ω/I^*	E_ω	E_ω/I^*	E_ω	E_ω/I^*	E_ω	E_ω/I^*	E_ω	E_ω/I^*
Distribution A										
200	0.242	2.42×10^{-5}	0.042	0.51×10^{-5}	0	0	0	0	0	0
1,000	.668	6.69	.348	4.25	.142	2.34×10^{-5}	.025	$.70\times10^{-5}$	.004	$.15\times10^{-5}$
3,000	.840	8.42	.644	7.86	.377	6.21	.160	4.49	.087	3.22
10,000	.912	9.14	.827	10.09	.688	11.34	.432	12.12	.300	11.10
Distribution C										
200	0.257	2.57×10^{-5}	0.064	0.78×10^{-5}	0	0	0	0	0	0
1,000	.630	6.31	.334	4.08	.155	2.55×10^{-5}	.042	1.18×10^{-5}	.012	$.44\times10^{-5}$
3,000	.812	8.14	.610	7.44	.387	6.38	.177	4.97	.104	3.85
10,000	.904	9.06	.802	9.79	.653	10.76	.434	12.18	.309	11.44
Distribution E										
200	0.273	2.74×10^{-5}	0.099	1.21×10^{-5}	0	0	0	0	0	0
1,000	.604	6.05	.359	4.38	.183	3.02×10^{-5}	.068	1.91×10^{-5}	.026	$.96\times10^{-5}$
3,000	.778	7.79	.588	7.17	.388	6.39	.202	5.67	.132	4.89
10,000	.886	8.88	.768	9.37	.627	10.33	.438	12.29	.328	12.14

(18) Droplet-size distribution	E
(19) $K_o\varphi$	5400
(20) $E_\omega/I^*=1/Vtw^*$	8.46×10^{-5}
(21) Mean effective droplet diameter, d, microns	14.1
(22) Liquid-water content, w^*, g/cu m	0.30

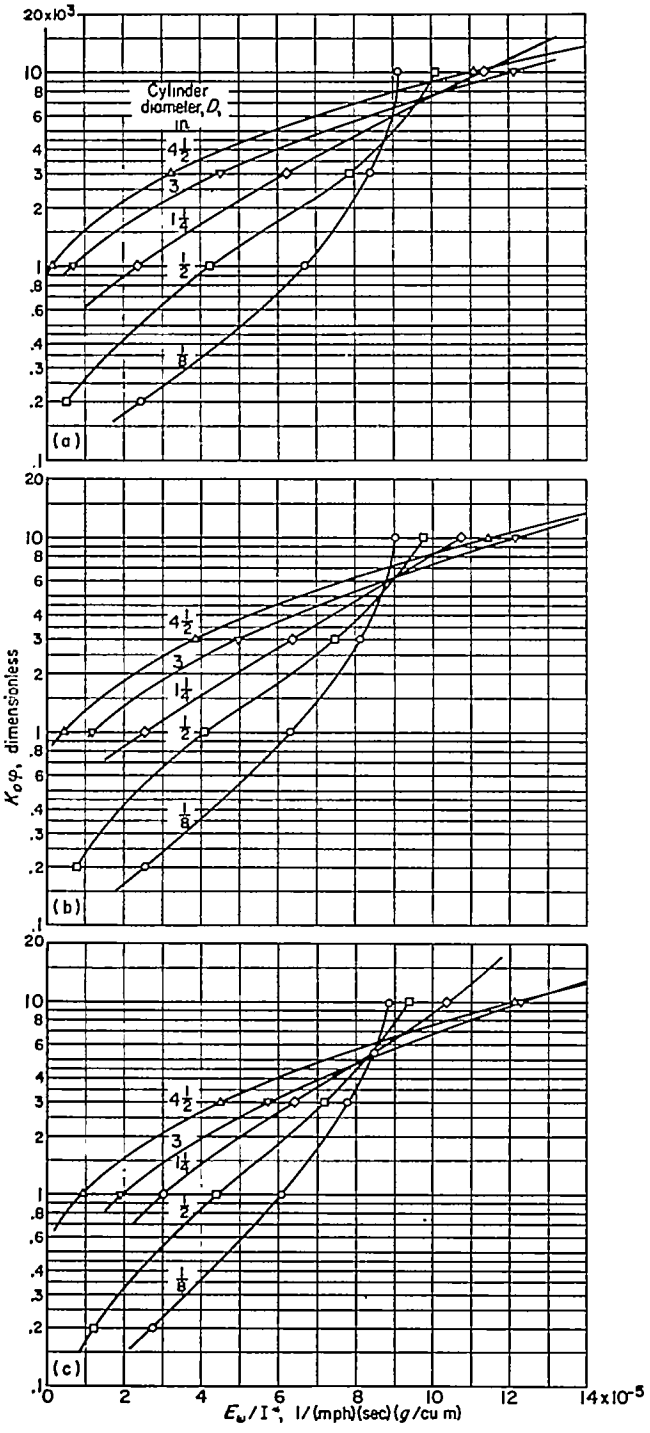

(a) Distribution A.
(b) Distribution C.
(c) Distribution E.

FIGURE 29.—Parameter $K_o\varphi$ as function of E_ω/I^* for various cylinder diameters.

(k) **Liquid-water content.**—The liquid-water content w^* is determined from the value of the quantity E_ω/I^* determined in step (i). This value of E_ω/I^*, which was determined by the intersection point of the curves of $K_o\varphi$ against E_ω/I^*, is actually equal to $1/Vtw^*$. The liquid-water content is determined by dividing the reciprocal of $1/Vtw^*$ by the product of V (item (3)) and t (item (8)). The liquid-water content for the example is 0.30 gram per cubic meter; this value is entered as item (22).

DISCUSSION

A comparison of the end results by this method (items (18), (21), and (22) in work sheet II) with those obtained by the standard method (items (20), (23), and (21) in work sheet I) shows very good agreement for the liquid-water content, droplet size, and droplet-size distribution. Droplet-size distribution E, however, may not be true for either method, because the curve of $K_o\varphi$ against E_ω/I^* for the 4½-inch cylinder did not intersect in a point with the other curves. For other sample calculations of actual flight data not presented here, the agreement was not always as good. This was especially true for droplet-size distribution. For liquid-water content and droplet size, the maximum difference was of the order of 10 percent. From these sample calculations some points of interest were observed, as follows:

(1) The curves of $K_o\varphi$ against E_ω/I^* for the ⅛-inch cylinder very often did not intersect in the same points as the other curves for any droplet-size distribution. This was especially true when the amount of ice collected by the ⅛-inch cylinder was large (diameter doubling during exposure time).

(2) The curves of $K_o\varphi$ against E_ω/I^* for the ½-, 1¼-, and 3-inch cylinders usually intersected in a small area for any droplet distribution pattern (see fig. 29).

(3) For some flight data, no more than two curves of $K_o\varphi$ against E_ω/I^* ever intersected in a point for any assumed droplet-size distribution.

The intersection of all the curves of $K_o\varphi$ against E_ω/I^* in a single point for a given droplet-size distribution by this method is the same as having all the plotted points fall along the given droplet-size distribution curve by the standard method. However, droplet-size distribution determinations are unreliable by either method, because an error in the amount of ice collected by one or more cylinders will give a nonexistent droplet-size distribution.

This method requires more calculations and plotting than the standard method. However, it eliminates the necessity of approximating the value of $K_o\varphi$ and of matching plotted points to standard curves by moving one chart with respect to the other.

APPENDIX F

ANALYSIS OF HEAT BALANCE AND MASS TRANSFER

ASSUMPTIONS

The heat balance of a system consisting of a rotating circular cylinder is described herein. The cylinder is exposed with its axis at right angles to the air stream in the region of accelerated flow about an airplane flying in a cloud composed of liquid-water droplets at a temperature below freezing. The following processes must be considered in an analysis of the heat balance:

(1) Convective heat transfer
(2) Kinetic heating
(3) Impingement of water droplets
(4) Evaporation or condensation
(5) Freezing
(6) Run-off of liquid water

Since some of the processes involved are not completely understood, the following simplifying assumptions are made to avoid undue complexity in the analysis:

(1) The surface temperature is uniform around the cylinder circumference, and average values of the heat-transfer coefficient are applicable to the cylinder as a whole.

(2) The expression $\epsilon(p_{v,S}-p_{v,0})/p_{a,0}$ represents the effective average difference in vapor concentration between the surface and the air stream.

(3) No condensation or evaporation occurs except at the cylinder surface.

(4) The water droplets strike the cylinder at the free-stream velocity and temperature.

(5) The conduction of heat into or out of the cylinder and the net loss or gain of heat by radiation are negligible compared with the other heat-transfer quantities.

(6) The liquid-water content in the air stream is not changed by the acceleration caused by the airplane fuselage.

EQUATIONS

The heat balance of the cylinder may be expressed by the following equation:

$$q_1-q_2+q_3+q_4=0 \tag{F1}$$

where

q_1 rate of heat loss by convective transfer to air stream
q_2 rate of heat gain due to change of enthalpy of water that freezes on surface
q_3 rate of heat loss due to change of enthalpy of water that evaporates from surface
q_4 rate of heat loss due to change of enthalpy of water that runs off in liquid state

The convective heat-transfer term q_1 is expressed as follows:

$$q_1=2\pi LH(T_S-T_{S,d}) \tag{F2}$$

where $T_{S,d}$ is the temperature that would be assumed by a dry cylinder in clear air. The dry-air kinetic temperature rise $(T_{S,d}-T_0)$ is regarded as occurring in two steps: (1) adiabatic cooling as the airspeed increases from U to U_l, given by

$$T_0-T_l=\frac{1}{2c_p}(U_l^2-U^2)$$

and (2) kinetic heating occurring when air characterized by T_l and U_l is brought to rest at the cylinder surface:

$$T_{S,d}-T_l=\frac{\sigma}{2c_p}U_l^2$$

where σ is the average recovery factor. Eliminating T_l and substituting in equation (F2) give

$$q_1=2\pi LH\left\{T_S-T_0-\frac{U^2}{2c_p}\left[1-\frac{U_l^2}{U^2}(1-\sigma)\right]\right\} \tag{F3}$$

The other three terms in equation (F1) represent the contributions due to the enthalpy changes of the impinging liquid water involved in the processes of freezing, evaporation, and run-off. It is convenient to express q_2, q_3, and q_4 in terms of the volume rates of freezing, evaporation, and run-off defined in equation (21). The heat-balance terms q_2, q_3, and q_4 may each be expressed as a product of a mass-flow rate and a change of specific enthalpy. If $h_{w,0}$ represents the specific enthalpy of the liquid-water droplets under free-stream conditions (T_0, U), the specific enthalpy of the droplets when brought to rest on the cylinder surface and before any heat has been transferred between the surface and the droplets is given by the expression $h_{w,0}+\frac{1}{2}U^2$, in which the second term is the free-stream specific kinetic energy. The equations for q_2, q_3, and q_4 are as follows:

Freezing:

$$q_2=2U_lLw_fE_\omega\left(h_{w,0}+\frac{1}{2}U^2-h_{ice,S}\right) \tag{F4}$$

Evaporation:

$$q_3=2U_lLw_eE_\omega\left(h_{v,S}-h_{w,0}-\frac{1}{2}U^2\right) \tag{F5}$$

Run-off:

$$q_4=2U_lLw_rE_\omega\left(h_{w,S}-h_{w,0}-\frac{1}{2}U^2\right) \tag{F6}$$

The rate of evaporation W_e is obtained from

$$W_e=2\pi L\epsilon\frac{H}{c_p}\left(\frac{p_{v,S}-p_{v,0}}{p_{a,0}}\right) \tag{F7}$$

The relation between heat and mass transfer for water vapor in air that is implied by the use of the coefficient H/c_p in equation (F7) is difficult to justify on theoretical grounds. Nevertheless, it is supported strongly by experimental evidence. In the range of low airspeeds, the equivalent assumption is that the temperature of a wet-bulb thermometer is equal to the adiabatic-saturation temperature. That this assumption is true, at least to a very satisfactory degree of approximation, has been firmly established by laboratory experiments (ref. 28) and by many years of experience with the use of wet- and dry-bulb thermometers

to measure humidity. Following Hardy (ref. 29), the same relation has been applied successfully at moderate and high airspeeds during the last ten years in the solution of anti-icing problems, including the successful prediction of the icing limit at a Mach number of 1.36 (ref. 30).

The evaporation heat loss q_3 may be expressed in terms of the convective heat-transfer coefficient by combining equations (21), (F5), and (F7) to obtain

$$q_3=\frac{2\pi LH\epsilon}{c_p}\left(\frac{p_{v,S}-p_{v,0}}{p_{a,0}}\right)\left(h_{v,S}-h_{w,0}-\frac{1}{2}U^2\right) \tag{F8}$$

When no run-off occurs, w_r and q_4 are zero; hence, the heat-balance equation becomes

$$q_2=q_1+q_3 \tag{F9}$$

Substituting from equations (F3), (F4), and (F8) in equation (F9), solving for w_fE_ω, and replacing H by $\kappa Nu/2L$ give the following:

$$w_fE_\omega=\frac{\pi\kappa Nu\left\{T_S-T_0-\frac{U^2}{2c_p}\left[1-\frac{U_l^2}{U^2}(1-\sigma)\right]+\frac{\epsilon}{c_p}\left(\frac{p_{v,S}-p_{v,0}}{p_{a,0}}\right)\left(h_{v,S}-h_{w,0}-\frac{1}{2}U^2\right)\right\}}{2LU_l\left(h_{w,0}+\frac{1}{2}U^2-h_{ice,S}\right)} \tag{F10}$$

The quantity w_fE_ω represents the volume rate of freezing expressed as slugs of ice formed per cubic foot of space swept by the cylinder. An equation for the volume rate of evaporation in the same units is obtained from equations (21) and (F7):

$$w_eE_\omega=\frac{\pi\kappa Nu\epsilon}{2LU_lc_p}\left(\frac{p_{v,S}-p_{v,0}}{p_{a,0}}\right) \tag{F11}$$

Equations (F10) and (F11) may be used to calculate the freezing and evaporation rates if the cylinder surface temperature is known. By assuming various values of surface temperature, the relation between freezing rate and evaporation rate may be established and a means provided for correcting multicylinder data for the effect of evaporation. In the critical case when the surface temperature is 0° C and $w_r=0$, equation (F10) gives the rate of freezing at the onset of run-off. Equations (F10) and (F11) are applicable whenever $w_rE_\omega=0$; that is, in both critical and subcritical conditions.

The use of equations (F10) and (F11) requires a knowledge of the Nusselt number. For smooth cylinders, the Nusselt number has been determined as a function of the Reynolds number (ref. 31). For a cylinder upon which glazed ice is forming—that is, under conditions in which the water does not freeze immediately on contact but spreads and runs on the surface as it freezes—the surface becomes rough, and the values of Nusselt number for smooth cylinders are not applicable. The following equation (ref. 32), based on a cylinder with longitudinal grooves, is used herein to determine the Nusselt number when the surface is presumed to be rough:

$$Nu=0.082Re_c^{0.747} \tag{F12}$$

This equation was established for a range of Reynolds numbers below 5000. Its use herein for cylinders operating at higher Reynolds numbers is justified by the fact that the results agree with observations, as shown subsequently.

In the subcritical condition, the impingement rate is insufficient to raise the surface temperature to 0° C, the run-off rate is zero, and the impingement rate is equal to the sum of the freezing and evaporation rates, as shown in the following equations:

$$wE_\omega<(wE_\omega)_{cr} \tag{24}$$

$$T_S<0°\text{ C} \tag{25}$$

$$wE_\omega=w_eE_\omega+w_fE_\omega \tag{26}$$

$$w_rE_\omega=0 \tag{27}$$

At the critical condition, the impingement rate is just sufficient to maintain the surface temperature at 0° C without run-off. Thus, the critical run-off rate is zero and the critical impingement rate equals the sum of the freezing rate and the evaporation rate. Hence, at the critical condition,

$$wE_\omega=(wE_\omega)_{cr}=(w_eE_\omega)_{cr}+(w_fE_\omega)_{cr} \tag{28}$$

$$T_S=0°\text{ C} \tag{29}$$

$$w_rE_\omega=(w_rE_\omega)_{cr}=0 \tag{30}$$

Supercritical conditions occur when the impingement rate exceeds the critical value. When ice is forming, the surface temperature cannot rise above 0° C; therefore, the evaporation rate w_eE_ω, the convective heat-transfer term q_1, and the evaporative cooling term q_3 remain constant at their critical values. The run-off rate w_rE_ω increases from zero with a corresponding increase in q_4, resulting in an increase in q_2, since q_1 and q_3 are constant. This increase in q_2 causes an increase in the freezing rate. The following equations apply, therefore, to the supercritical case:

$$wE_\omega>(wE_\omega)_{cr} \tag{31}$$

$$T_S=0°\text{ C} \tag{32}$$

$$w_eE_\omega=(w_eE_\omega)_{cr} \tag{33}$$

$$w_rE_\omega>0 \tag{F13}$$

$$w_fE_\omega>(w_fE_\omega)_{cr} \tag{F14}$$

An expression for w_fE_ω is obtained from equations (F1) and (F4) for the supercritical case:

$$w_fE_\omega=\frac{q_1+q_3+q_4}{2U_lL(h_{w,0}-h_{ice,S}+\frac{1}{2}U^2)}$$

In the critical case, $q_4=0$; hence,

$$(w_fE_\omega)_{cr}=\frac{q_1+q_3}{2U_lL(h_{w,0}-h_{ice,S}+\frac{1}{2}U^2)}$$

The excess of the volume freezing rate above the critical value is given by

$$w_fE_\omega-(w_fE_\omega)_{cr}=\frac{q_4}{2U_lL(h_{w,0}-h_{ice,S}+\frac{1}{2}U^2)}$$

Introducing the value of q_4 from equation (F6) gives the following expression for the excess of the actual freezing rate over the critical:

$$w_fE_\omega-(w_fE_\omega)_{cr}=\frac{w_rE_\omega(h_{w,S}-h_{w,0}-\frac{1}{2}U^2)}{(h_{w,0}-h_{ice,S}+\frac{1}{2}U^2)} \tag{F15}$$

The excess impingement rate over the critical value is

$$wE_\omega-(wE_\omega)_{cr}=w_fE_\omega-(w_fE_\omega)_{cr}+w_rE_\omega \tag{F16}$$

The fraction of the excess water that freezes, called the "freezing fraction" in reference 18, is given by

$$\lambda=\frac{w_fE_\omega-(w_fE_\omega)_{cr}}{wE_\omega-(wE_\omega)_{cr}} \tag{F17}$$

From equations (F15) to (F17) there is obtained

$$\lambda=\frac{h_{w,S}-h_{w,0}-\frac{1}{2}U^2}{h_{w,S}-h_{ice,S}} \tag{36}$$

Except at high airspeeds and temperatures close to freezing, $\frac{1}{2}U^2$ is small compared with $h_{w,S}-h_{w,0}$. Neglecting $\frac{1}{2}U^2$ and noting that

$$h_{w,S}-h_{ice,S}=\frac{80(h_{w,S}-h_{w,0})}{T_S-T_0}$$

give the approximate equation for the freezing fraction used in reference 18:

$$\lambda\cong\frac{-T_0}{80} \tag{F18}$$

The following expression for the volume freezing rate under supercritical conditions is obtained from equation (F17):

$$w_fE_\omega=(w_fE_\omega)_{cr}+\lambda[wE_\omega-(wE_\omega)_{cr}] \tag{34}$$

and an expression for the volume run-off rate is obtained from equations (F16) and (34):

$$w_rE_\omega=(1-\lambda)[wE_\omega-(wE_\omega)_{cr}] \tag{35}$$

CALCULATIONS

The values of critical volume freezing and evaporation rates presented in table IV were calculated from equations (F10) and (F11) by setting $T_S=0°$ C for the critical condition and using equation (F12) to determine the Nusselt number for the rough surface condition. Additional calculations were made using values of T_S intermediate between T_0 and the melting point for both rough and smooth surface conditions. Values of $w_e{}^*E_\omega$ were then plotted as a function of $w_f{}^*E_\omega$ for each set of flight conditions, and a straight line was determined for each case to represent approximately the relation between $w_e{}^*E_\omega$ and $w_f{}^*E_\omega$ for rough cylinders at the higher values of $w_f{}^*E_\omega$ and for smooth cylinders at the lower values. The assumption implied in this procedure is that the surface is smooth at low rates of ice formation and becomes rough as the critical condition is approached. Values of the parameters defining these lines are given in table V.

The use of equations (F10) and (F11) requires that several additional quantities be known as functions of the independent variables. These quantities were obtained as follows.

The Nusselt number was obtained from equation (F12) for a rough surface and from the curve in reference 31 for a smooth surface. The Reynolds number Re_σ was evaluated at the local airspeed U_l, the free-stream pressure $p_{a,0}$, and the average of the free-stream and surface temperature. The value 1.12 used for the ratio U_l/U was obtained from measurements made in calibrating the multicylinder exposure used on the C-46 airplane by the Ames laboratory (ref. 33). Actual calibrations are not available for other airplanes, but it would appear reasonable to assume that this value is approximately representative for cylinders exposed at a position on the upper portion of the fuselage over the trailing edge of the wing on a conventional transport-type airplane.

There is some uncertainty as to the over-all temperature-recovery factor for a cylinder in transverse flow. The value $\sigma=0.75$ was chosen as a representative average value on the basis of test results summarized in reference 34. The vapor pressure at the surface $p_{v,S}$ was taken as the saturation vapor pressure over ice at the temperature T_S, and the free-stream vapor pressure $p_{v,0}$ was taken as the saturation vapor pressure over water at the temperature T_0, based on the assumption of 100 percent relative humidity in the undisturbed cloud.

FREEZING RATES

The calculated values of critical volume freezing rates are difficult to verify from flight data, because a cylinder influenced by run-off usually experiences both subcritical and supercritical conditions during the exposure period. Under subcritical conditions, the volume freezing rate w_fE_ω is approximately directly proportional to the volume impingement rate wE_ω, and the departure of the latter below the critical value is reflected directly in the measured average value of the former. Under supercritical conditions, on the other hand, the increase in volume freezing rate above the critical value is equal to the freezing fraction λ times the increase in volume impingement rate. Since λ is usually small compared with unity, variations in volume impingement rate above the critical value have a much smaller effect on the measured average value of volume freezing rate than variations below the critical value. Furthermore, the largest excesses of volume impingement rate above the critical value tend to occur at temperatures only slightly below freezing when the freezing fraction is very small; whereas, at lower temperatures when λ assumes larger values, the critical impingement rate is larger and the excess of impingement over the critical value is smaller. It is to be expected, therefore, that the effect on the measured average volume freezing rate of periods of subcritical conditions (including gaps in the clouds) would at least offset the effect of supercritical con-

ditions so that the maximum observed rates of freezing would not be likely to exceed the critical values.

A comparison of maximum observed and calculated critical values of volume freezing rate is shown in figure 30 for four cylinder sizes. The measured values represented by the data points were computed from the original records of weight of ice, exposure duration, and flight speed. The calculated critical values were obtained by interpolation from the data of table IV and adjusted for average cylinder diameter by use of equation (23). The average cylinder diameter was based on an assumed ice density of 0.9 gram per cubic centimeter, since the amount of entrained air is a minimum in conditions of run-off. All available multicylinder data obtained in flight by the NACA were examined, and values of volume freezing rate were computed for all cases in which run-off was a possibility. Only the higher values of $w_f{}^*E_\omega$ are plotted in figure 30.

The results show that the calculated critical volume freezing rate is a good approximation to the maximum observed rate. The data points are scattered below the 45° line (representing critical conditions), with a rather sharp cut-off just below the line. A few points lie above the line,

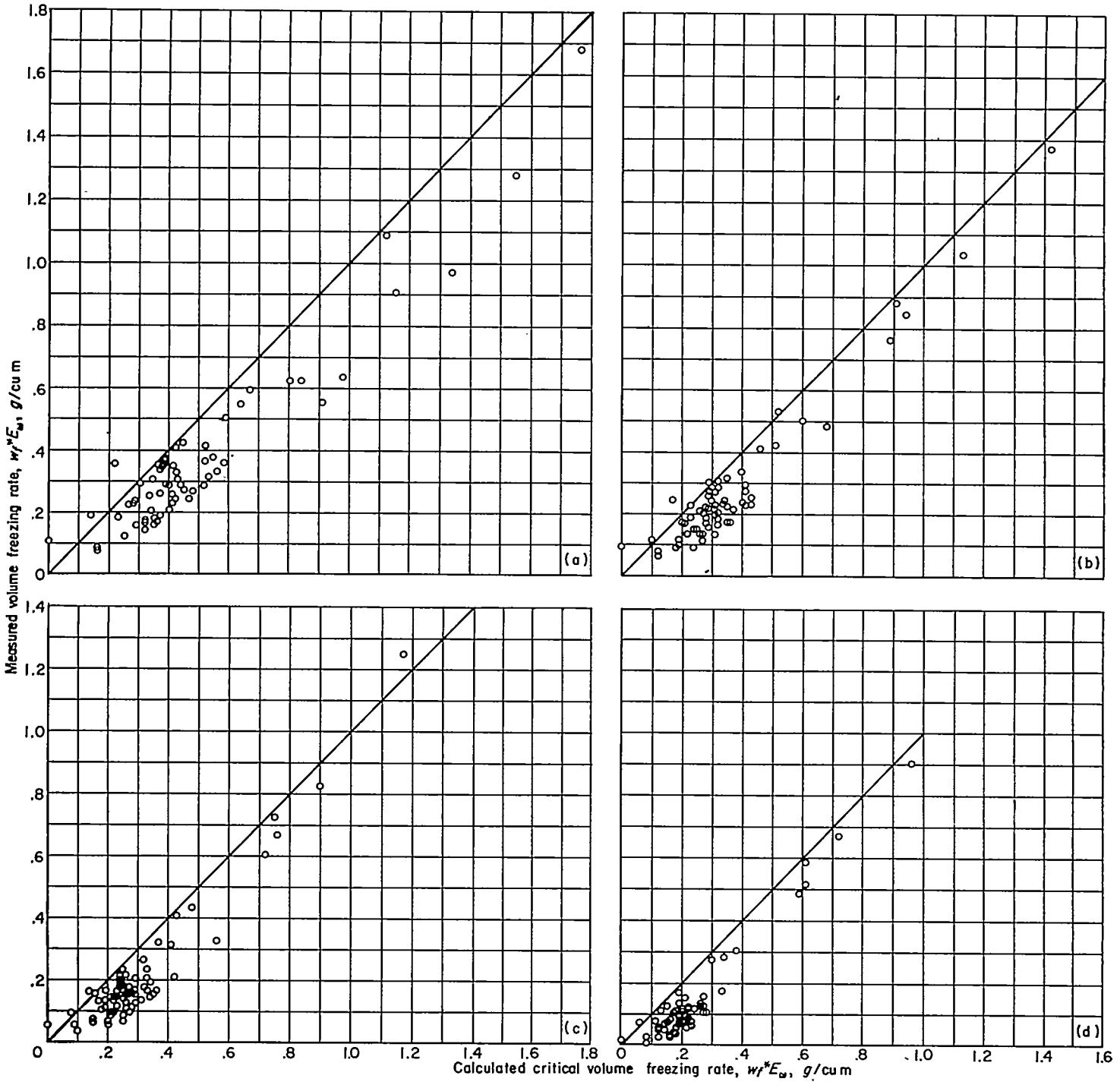

(a) Initial cylinder diameter, ⅛ inch.
(b) Initial cylinder diameter, ½ inch.
(c) Initial cylinder diameter, 1¼ inches.
(d) Initial cylinder diameter, 3 inches.

FIGURE 30.—Comparison of calculated critical volume freezing rate and maximum measured values of volume freezing rate.

presumably because of errors in measuring free-air temperature or weight of ice. The fact that the agreement is good for all values of cylinder diameters shows that the exponent used in equation (F12) is approximately correct. As the cylinder size increases, the number of points close to the critical line decreases, because the lower collection efficiency reduces the chances of encountering critical conditions.

REFERENCES

1. Glauert, Muriel: A Method of Constructing the Paths of Raindrops of Different Diameters Moving in the Neighbourhood of (1) a Circular Cylinder, (2) an Aerofoil, Placed in a Uniform Stream of Air; and a Determination of the Rate of Deposit of the Drops on the Surface and the Percentage of Drops Caught. R. & M. No. 2025, British A. R. C., 1940.
2. Ranz, W. E.: The Impaction of Aerosol Particles on Cylindrical and Spherical Collectors. Tech. Rep. No. 3, Eng. Exp. Station, Univ. Ill., Mar. 31, 1951. (Contract No. AT(30–3)–28, U. S. Atomic Energy Comm.)
3. Langmuir, Irving, and Blodgett, Katherine B.: A Mathematical Investigation of Water Droplet Trajectories. Tech. Rep. No. 5418, Air Materiel Command, AAF, Feb. 19, 1946. (Contract No. W–33–038–ac–9151 with General Electric Co.)
4. Brun, Edmond, Caron, Robert, et Vasseur, Marcel: Introduction à l'étude de la Mécanique des Suspensions. G. R. A. Rapport Tech. No. 15, Recherches Aéronautiques (Paris), 1945.
5. Kantrowitz, Arthur: Aerodynamic Heating and the Deflection of Drops by an Obstacle in an Air Stream in Relation to Aircraft Icing. NACA TN 779, 1940.
6. Dorsch, Robert G., Brun, Rinaldo J., and Gregg, John L.: Impingement of Water Droplets on an Ellipsoid with Fineness Ratio 5 in Axisymmetric Flow. NACA TN 3099, 1954.
7. Brun, Rinaldo J., and Dorsch, Robert G.: Impingement of Water Droplets on an Ellipsoid with Fineness Ratio 10 in Axisymmetric Flow. NACA TN 3147, 1954.
8. Dorsch, Robert G., and Brun, Rinaldo J.: Variation of Local Liquid-Water Concentration about an Ellipsoid of Fineness Ratio 5 Moving in a Droplet Field. NACA TN 3153, 1954.
9. Hacker, Paul T., Brun, Rinaldo J., and Boyd, Bemrose: Impingement of Droplets in 90° Elbows with Potential Flow. NACA TN 2999, 1953.
10. Bergrun, Norman R.: A Method for Numerically Calculating the Area and Distribution of Water Impingement on the Leading Edge of an Airfoil in a Cloud. NACA TN 1397, 1947.
11. Bergrun, Norman R.: An Empirically Derived Basis for Calculating the Area, Rate, and Distribution of Water-Drop Impingement on Airfoils. NACA Rep. 1107, 1952.
12. Brun, Rinaldo J., Gallagher, Helen M., and Vogt, Dorothea E.: Impingement of Water Droplets on NACA 65_1–208 and 65_1–212 Airfoils at 4° Angle of Attack. NACA TN 2952, 1953.
13. Brun, Rinaldo J., Gallagher, Helen M., and Vogt, Dorothea E.: Impingement of Water Droplets on NACA 65A004 Airfoil and Effect of Change in Airfoil Thickness from 12 to 4 percent at 4° Angle of Attack. NACA TN 3047, 1953.
14. Brun, Rinaldo J., Gallagher, Helen M., and Vogt, Dorothea E.: Impingement of Water Droplets on NACA 65A004 Airfoil at 8° Angle of Attack. NACA TN 3155, 1954.
15. Dorsch, Robert G., and Brun, Rinaldo J.: A Method for Determining Cloud-Droplet Impingement on Swept Wings. NACA TN 2931, 1953.
16. Anon.: The Multicylinder Method. The Mount Washington Monthly Res. Bull., vol. II, no. 6, June 1946.
17. Ludlam, F. H.: The Heat Economy of a Rimed Cylinder. Quarterly Jour. Roy. Meteorological Soc., vol. 77, no. 334, Oct. 1951 pp. 663–666.
18. Fraser, D., Rush, C. K., and Baxter, D.: Thermodynamic Limitations of Ice Accretion Instruments. Lab. Rep. LR–32, Nat. Aero. Establishment, Ottawa (Canada), Aug. 22, 1952.
19. Wien, W., and Harms, F., eds.: Handbuch der Experimentalphysik. Teil 4, Bd. 4, Akad. Verlagsgesellschaft M. B. H. (Leipzig), 1932.
20. Glauert, H.: The Elements of Aerofoil and Airscrew Theory. The Macmillan Co. (New York), 1944.
21. Lowell, Herman H.: Maximum Evaporation Rates of Water Droplets Approaching Obstacles in the Atmosphere under Icing Conditions. NACA TN 3024, 1953.
22. Brun, Rinaldo J., and Mergler, Harry W.: Impingement of Water Droplets on a Cylinder in an Incompressible Flow Field and Evaluation of Rotating Multicylinder Method for Measurement of Droplet-Size Distribution, Volume-Median Droplet Size, and Liquid-Water Content in Clouds. NACA TN 2904, 1953.
23. Eser, F. (M. Flint, trans.): On the Flow of Compressible Fluids Past Solid Bodies at Subsonic Velocity. Luftfahrtforschung, vol. 20, no. 7, July 20, 1943, pp. 220–230. (R. T. P. Trans. No. 2056.)
24. Neel, Carr B., Jr., Bergrun, Norman R., Jukoff, David, and Schlaff, Bernard A.: The Calculation of the Heat Required for Wing Thermal Ice Prevention in Specified Icing Conditions. NACA TN 1472, 1947.
25. Howell, Wallace E.: Comparison of Three Multicylinder Icing Meters and Critique of Multicylinder Method. NACA TN 2708, 1952.
26. Clark, Victor F.: Conditions for Run-Off and Blow-Off of Catch on Multicylinder Icing Meter. Harvard-Mt. Washington Icing Research Report 1946–47, AF Tech. Rep. 5676, United States Air Force, pp. 190–218.
27. Jahnke, Eugen, and Emde, Fritz: Tables of Functions. Fourth ed., Dover Pub., 1945.
28. Dropkin, David: The Deviation of the Actual Wet-Bulb Temperature from the Temperature of Adiabatic Saturation. Bull. No. 23, Eng. Exp. Station, Cornell Univ., July 1936.
29. Hardy, J. K.: An Analysis of the Dissipation of Heat in Conditions of Icing from a Section of the Wing of the C–46 Airplane. NACA Rep. 831, 1945. (Supersedes NACA ARR 4I11a.)
30. Callaghan, Edmund E., and Serafini, John S.: Analytical Investigation of Icing Limit for Diamond-Shaped Airfoil in Transonic and Supersonic Flow. NACA TN 2861, 1953.
31. McAdams, William H.: Heat Transmission. Second ed., McGraw-Hill Book Co., Inc., 1942.
32. Jakob, Max: Heat Transfer. Vol. I. John Wiley & Sons, Inc., 1949.
33. Lewis, William, Kline, Dwight B., and Steinmetz, Charles P.: A Further Investigation of the Meteorological Conditions Conducive to Aircraft Icing. NACA TN 1424, 1947.
34. Johnson, H. A., and Rubesin, M. W.: Aerodynamic Heating and Convective Heat Transfer—Summary of Literature Survey. Trans. A. S. M. E., vol. 71, no. 5, July 1949, pp. 447–456.
35. Kline, Dwight B., and Walker, Joseph A.: Meteorological Analysis of Icing Conditions Encountered in Low-Altitude Stratiform Clouds. NACA TN 2306, 1951.
36. Lewis, William, and Hoecker, Walter H., Jr.: Observations of Icing Conditions Encountered in Flight During 1948. NACA TN 1904, 1949.

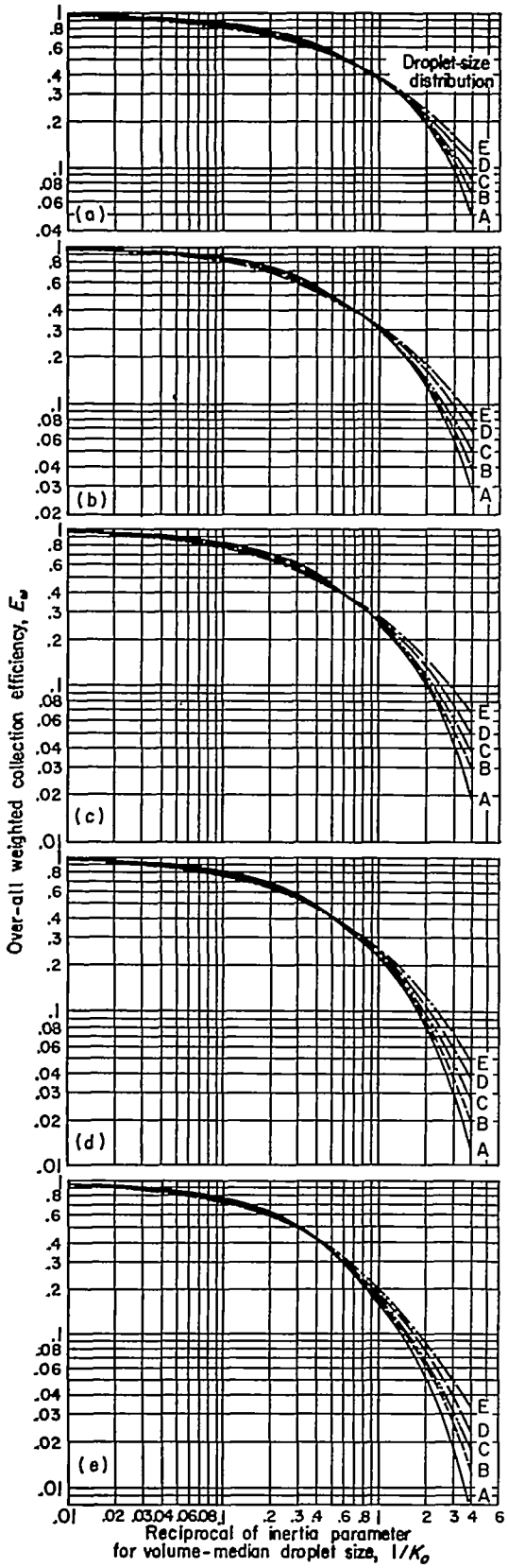

(a) $K_0\varphi$, 0.
(b) $K_0\varphi$, 200.
(c) $K_0\varphi$, 1000.
(d) $K_0\varphi$, 3000.
(e) $K_0\varphi$, 10,000.

FIGURE 12.—Over-all weighted collection efficiency as function of reciprocal of inertia parameter for volume-median droplet size for five cloud droplet-size distributions.

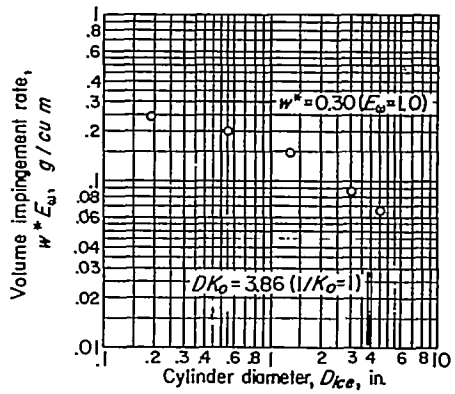

FIGURE 20.—Sample plot of volume impingement rate w^*E_ω as function of cylinder diameter.

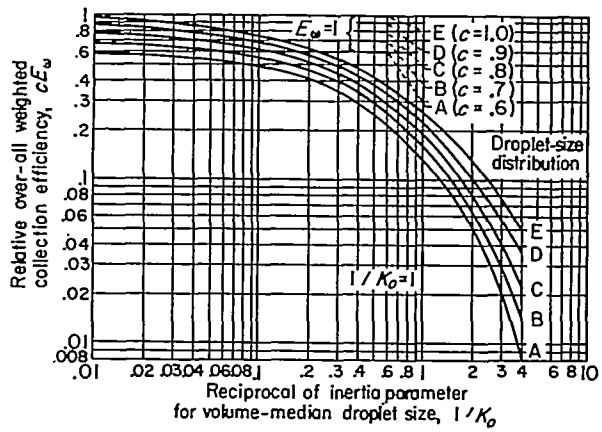

FIGURE 21.—Curves from data of table III showing relative over-all weighted collection efficiency as function of reciprocal of inertia parameter for $K_0\varphi=3000$ for droplet-size distributions defined in table II.